

INSTITUTO TECNOLÓGICO Y DE ESTUDIOS
SUPERIORES DE MONTERREY
CAMPUS MONTERREY
DIVISION DE INGENIERIA
PROGRAMA DE GRADUADOS EN INGENIERIA



PROGRESSIVE FAILURE ANALYSIS OF A COMPOSITE
THIN-WALLED BEAM FINITE ELEMENT MODEL
UNDER AEROELASTIC LOADING CONDITIONS
Modeling and Simulation

TESIS

PRESENTADA COMO REQUISITO PARCIAL
PARA OBTENER EL GRADO ACADÉMICO DE:
DOCTOR EN CIENCIAS DE INGENIERIA
CON ESPECIALIDAD EN ENERGIA EOLICA

POR
DIEGO ERNESTO CARDENAS FUENTES

MONTERREY, N. L.,

DICIEMBRE DE 2011

**INSTITUTO TECNOLÓGICO Y DE ESTUDIOS
SUPERIORES DE MONTERREY
CAMPUS MONTERREY
DIVISION DE INGENIERIA
PROGRAMA DE GRADUADOS EN INGENIERIA**



**PROGRESSIVE FAILURE ANALYSIS OF A COMPOSITE
THIN-WALLED BEAM FINITE ELEMENT MODEL
UNDER AEROELASTIC LOADING CONDITIONS:
Modeling and Simulation**

TESIS

**PRESENTADA COMO REQUISITO PARCIAL
PARA OBTENER EL GRADO ACADÉMICO DE:
DOCTOR EN CIENCIAS DE INGENIERIA
CON ESPECIALIDAD EN ENERGIA EOLICA**

**POR
DIEGO ERNESTO CARDENAS FUENTES**

MONTERREY, N. L.

DICIEMBRE DE 2011

INSTITUTO TECNOLÓGICO Y DE ESTUDIOS SUPERIORES DE MONTERREY

CAMPUS MONTERREY

DIVISIÓN DE INGENIERÍA

PROGRAMA DE GRADUADOS EN INGENIERÍA



PROGRESSIVE FAILURE ANALYSIS OF A COMPOSITE THIN-WALLED BEAM FINITE ELEMENT MODEL UNDER AEROELASTIC LOADING CONDITIONS: Modeling and Simulation

TESIS

PRESENTADA COMO REQUISITO PARCIAL PARA OBTENER EL GRADO ACADÉMICO DE:

DOCTOR EN CIENCIAS DE INGENIERÍA

CON ESPECIALIDAD EN ENERGÍA EOLICA

POR

DIEGO ERNESTO CARDENAS FUENTES

MONTERREY, N.L.

DICIEMBRE DE 2011

**INSTITUTO TECNOLÓGICO Y DE ESTUDIOS SUPERIORES DE
MONTERREY**


CAMPUS MONTERREY

DIVISIÓN DE INGENIERÍA
PROGRAMA DE GRADUADOS EN INGENIERÍA

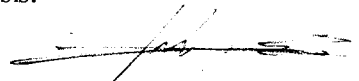
Los miembros del Comité de Tesis recomendamos que este documento de disertación presentado por Diego Ernesto Cárdenas Fuentes sea aceptado como requisito parcial para obtener el grado académico de:

**Doctor en Ciencias de Ingeniería con
Especialidad en Energía Eólica**

Comité de Tesis:



Dr. Oliver Matthias Probst Oleszewski
Asesor



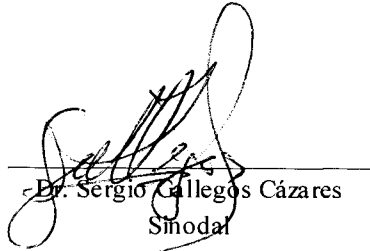
Dr. Hugo Ramón Elizalde Siller
Co-Asesor



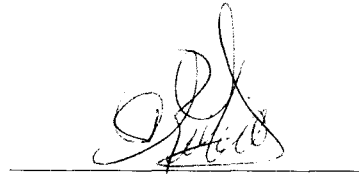
Dr. Piergiorgio Marzocca
Co-Asesor



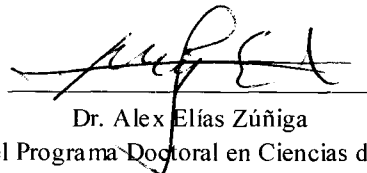
Dr. Ciro Ángel Rodríguez González
Sinodal



Dr. Sergio Callegos Cázares
Sinodal



Dr. Carlos Rubio González
Sinodal



Dr. Alex Elías Zúñiga
Director del Programa Doctoral en Ciencias de Ingeniería

Diciembre de 2011

DEDICATORIA

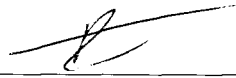
A mi Familia y Amigos

AGRADECIMIENTOS

Esta tesis es fruto de del esfuerzo y colaboración de muchas personas. En primer lugar quiero hacer patente el agradecimiento al Dr. Oliver Probst por haberme dado la oportunidad de iniciarme a su lado en el mundo de la energía eólica y por su motivación constante para dar lo mejor de mí. Al Dr. Hugo Elizalde por las innumerables horas en las que pacientemente compartió su conocimiento conmigo. Al Dr. Piergiovanni Marzocca por su siempre entusiasta participación, la cual permitió elevar la calidad de los objetivos de este trabajo. Además de mi infinito agradecimiento por su invaluable apoyo en momentos difíciles en mi salud. Quiero agradecer también a mis sinodales, al Dr. Ciro Rodríguez por su confianza y apoyo invariable desde mi etapa de estudiante de ingeniería. Al Dr. Sergio Gallegos por su amable disponibilidad a atender muchas de las dudas que surgieron lo largo de la realización de la tesis. Al Dr. Carlos Rubio por sus consejos y evaluación que hizo de este trabajo. Quiero reconocer la invaluable ayuda y muestras de fraternidad que siempre recibí de todos mis compañeros y amigos de la Cátedra de Energía Eólica: Escarpita, Juan Pablo, Roberto, Romo, Juan José, Herbe, David, Paco, Jorge y Jaime. Tampoco quiero dejar de mencionar la importancia del financiamiento económico que recibí del ITESM Campus Monterrey, de su Cátedra de Energía Eólica y del New York State Energy Research and Development Authority (NYSERDA) a través del Dr. Marzocca. Finalmente es gratamente apreciado el apoyo de AlphaStar a través de la autorización en el uso de su software y el entrenamiento otorgado.

COPYRIGHT DECLARATION

I, hereby, declare that I wrote this dissertation entirely by myself, and that it exclusively describes my own research. Every contribution from colleagues, professors, researchers, entrepreneurs, specialists, technicians, practitioners and graduate students are properly referenced.



Diego Ernesto Cárdenas Fuentes

ABSTRACT

New advanced composite blades design methodologies can significantly impact the performance and reliability of wind turbine technologies. Current approaches employed in designing composite turbine blades, resort to sophisticated multiphysics codes taking into account fluid-structure interaction. When it comes to structural health monitoring and damage progression, the practitioner needs to evaluate the integrity of the composite structure by using in-situ real-time techniques, often neglecting the effect of the degradation of structure properties, particularly when addressing complex aeroelastic simulations. This work contributes to the state-of-the-art of damage progression in composite blade under dynamic operating conditions. Due to computational inefficiencies and the high demands of computational resources, dynamic aeroelastic simulations are performed using reduced order models. Wind turbine rotor blades are efficiently modeled using a thin-walled beam (TWB) approach, a 1D FE model capable of capturing most essential characteristics of slender structures. The TWB was chosen because it enables to recover the strains and stresses for all layers at any position of the blade, therefore enabling the integration of failure models capable of predicting the propagation of damage in the structure. Due to its computational efficiency it is possible to integrate the TWB in a dynamic aeroelastic environment capable of describing the fluid-structure interaction occurring during operational conditions. The proposed architecture enables the evaluation of the blade structural integrity at every time-step. Failure criteria are checked at every time-step and when met, the mechanical properties of the damaged area are degraded and the stiffness matrix of the structure is updated. This approach fully couples the aerodynamics loads, structural and inertial loads, along with the effect of the damage caused by the applied loads. The ultimate goal is to provide the practitioner tools for the evaluation of blade integrity during operational condition, to assess their behavior during aeroelastic simulations and to provide insight into damage progression and reliability of composite turbine blades.

Table of contents

DEDICATORIA.....	i
AGRADECIMIENTOS.....	ii
COPYRIGHT DECLARATION	iii
ABSTRACT.....	iv
Table of contents.....	v
List of Figures.....	ix
List of Tables	xiii
Nomenclature.....	xiv
Chapter 1.....	1
Introduction	1
Chapter Summary	1
1.1. Background	1
1.2. Wind Turbine Damage Assessment.....	3
1.3. Scope and Approach	5
1.4. Organization of Contents	6
References	7
Chapter 2.....	1
Damage in Composite Materials.....	1
Chapter Summary	1
2.1. Failure criteria review	1
2.1.1. Parametric failure criteria	2

2.1.2.	Phenomenological failure criteria	3
2.1.3.	Micromechanics strength prediction	4
2.1.4.	Probabilistic criteria	5
2.2.	Failure criteria evaluation	5
2.2.1.	Characteristic of the theories	5
2.2.2.	Ranking of theories	6
2.3.	GENOA (Chamis model).....	8
2.3.1.	Software description.....	8
2.3.2.	WWF evaluation of Chamis theory.....	10
	References	12
Chapter 3.	1
Thin-Walled Beam Model.....	1
Chapter Summary	1
3.1. Kinematics.....	4
3.1.1. Warping theory	7
3.1.2. Strain in TWB.....	11
3.2. Constitutive equations.....	11
3.3. Finite element model	13
References	17
Chapter 4.	1
Static and dynamic TWB validation	1
Chapter Summary	1
4.1. Definition of the geometry	2
4.1.1. External geometry	3

4.1.2. Internal geometry	5
4.2. Materials Layup	6
4.3. Results	8
4.4. Conclusion.....	17
References	20
Chapter 5.	1
Progressive Failure Analysis of Thin-Walled Composites Structures	1
Chapter Summary	1
5.1. Methodology	2
5.1.1. Integrated Thin-Walled Beam Progressive Failure Analysis model	2
5.1.2. Implementation of the integrated TWB-PFA model.....	5
5.1.3. Description of case study.....	7
5.2. Results and discussion	9
5.3. Summary and conclusions.....	21
References	24
Chapter 6.	1
Dynamic Aeroelastic Progressive Failure Analysis of Thin-Walled Composite Structures.....	1
Chapter Summary	1
6.1. Description of the model.....	3
6.1.1. Thin-wall beam (TWB) model with Progressive Failure Analysis (PFA) ..	3
6.1.2. Aerodynamic loads.....	7
6.1.3. Gravitational and centrifugal loads	9
6.1.4. Wind speed time series generation.....	10
6.2. Program structure	10

6.2.1. Static aeroelastic module	12
6.2.2. Dynamic aeroelastic module.....	14
6.2.3. Damage module	15
6.3. Description of the case study.....	16
6.3.1. Case 1: Parked rotor facing a class 5 hurricane	16
6.3.2. Case 2: Wind speed ramp at constant rotor shaft frequency.....	17
6.3.3. Case 3: Constant wind speed and loss of load	17
6.3.4. Blade description	17
6.4. Results and discussion	19
6.4.1. Case 1: Parked rotor facing class 5 hurricane	19
6.4.2. Case2: Wind speed ramp at constant rotor shaft frequency.....	22
6.4.3. Case 3: Constant Wind Speed.....	25
6.5. Conclusion.....	27
References	29
Chapter 7.....	1
Conclusions and further work.....	1
7.1. Conclusions and summary of contributions	1
7.2. Future Outlook	2
Appendix A.....	1
Appendix B.....	3
Appendix C.....	5
Appendix D.....	7

List of Figures

Figure 1.1: Global annual installed wind capacity 1996-2010 [3].....	2
Figure 1.2: Rotor size evolution of wind turbines [6]	2
Figure 2.1: Most used failure criteria among engineers [8].....	2
Figure 2.2: CODSTRAN simulation cycle [21].....	8
Figure 3.1: Decomposition of a 3D blade problem into a 1D Beam [9]	2
Figure 3.2: Geometry layout and mesh of a cross sectional area [9].	3
Figure 3.3: A) generic beam element of a wind turbine blade. B) Mid-surface and Coordinate Systems (CS)	5
Figure 3.4: Angular displacements of TWB.....	7
Figure 3.5: Warping shear stresses in some open cross-sections [19].....	8
Figure 3.6: Warping Normal Stresses in some open cross-sections [19].	8
Figure 3.7: Warping displacement behaviour [28].....	9
Figure 3.8: Generic 2-node TWB element with 14 DOF	16
Figure 4.1: External chord (C) variation along blade's length [8]. See Appendix B for detailed information of cross-sections belonging to the transitional region.	3
Figure 4.2: Airfoil S821 divided in segments I through V. Divisions occur at 0%, 5%, 30%, 40%, 60% and 100% of the chord's length.	4
Figure 4.3: Twist angle (β) distribution along blade's length [8].	4
Figure 4.4: Airfoil alignment over the reference line.....	5

Figure 4.5: Cut view of the blade at a radius position of $R=3.2\text{m}$, showing the airfoil's cross-section and internal shear web. Colours identify the Layup Code.....	6
Figure 4.6: The blade section numbering and positions. Colours represent the <i>Layup Code</i> , fully detailed in Appendix C. <i>Layup Code 16</i> , not included in this Figure, represents the internal shear-web's layup.....	7
Figure 4.7: Model 1 built in ANSYS®	9
Figure 4.8.....	11
Figure 4.9: Displacement curves for Load Cases 1 and 2	14
Figure 4.10: Angular displacement curves for Load Case 3.....	15
Figure 4.11: Flapwise displacement curves for Load Case 4	15
Figure 4.12: Point-FRF for flapwise tip DOF.....	16
Figure 4.13: FRF for edgewise tip DOF (excitation at flapwise tip DOF).....	16
Figure 5.1 : PFA simulation cycle	6
Figure 5.2: Cross sectional area of the blade.....	8
Figure 5.3: Out-of-plane blade tip displacement versus applied load.....	10
Figure 5.4: Evolution of the blade cross-section at 450 mm from the root end as a function of the applied load.....	11
Figure 5.5: Percentage of damage volume vs. load for the three blade models.....	12
Figure 5.6: Damage Progression of Layer 4 (90°). (a) Plot showing location of damaged cells in layer 4 for different values of the external load as predicted by the GENOA model. (b) Corresponding plot built from the results obtained with the TWB-PFA model. Note that different scales have been used for visualization the deflection of the beam in the GENOA model (a) and the TWB-PFA model (b).....	14

Figure 5.7: Top view of the Damage Progression of Layer 4 (90° fibre orientation). (a) Damage map calculated from GENOA for different values of the tip load. (b) Corresponding damage map obtained with the TWB-PFA model.....	15
Figure 5.8: Cumulative damage volume as a function of the spanwise coordinate for Layer 4 (90° fibre orientation) and four load cases. Continuous curves: Predictions of the shell model. Dashed curves: Predictions of the unadjusted TWB-PFA model. Fine-dashed curve: Predictions of the TWB-PFA model with adjusted strength values	18
Figure 5.9: Damage Progression of Layer 7 (0°) as shown as damage maps for the two load cases where damage was observed. Left: Predictions of the shell model. Right: Predictions of the TWB-PFA model	19
Figure 5.10: Top view of the Damage Progression of Layer 7 (0° fibre orientation). Upper graph: Predictions of the shell model. Lower graph: Predictions of the TWB-PFA model.	20
Figure 5.11: Cumulative damage volume as a function of the spanwise coordinate for Layer 7 (0°). Continuous curve: Predictions of the shell model. Dashed curve: Predictions of the TWB-PFA model.	21
Figure 6.1: Global and mid-surface coordinate system.....	4
Figure 6.2: A generic 2-node TWB element with 7 DOFs per node.....	5
Figure 6.3: Blade element Forces and Velocities [11]	8
Figure 6.4: Aeroelastic code with damage progression capabilities (flowchart)	11
Figure 6.5: Static Aeroelastic Module diagram	13
Figure 6.6: Aeroelastic Module flowchart.....	14
Figure 6.7: Damage Module Diagram.....	16
Figure 6.8: Blade geometry and materials layup	18
Figure 6.9: Wind speed time series and damage volume	19
Figure 6.10: Flapwise displacement.....	20

Figure 6.11: Progressive Failure Analysis of layer 6 (Balsa)	21
Figure 6.12: Wind speed time series and damage volume	22
Figure 6.13: Flapwise displacement and azimuth position of the blade.....	23
Figure 6.14: Progressive Failure Analysis of layer 6 (Balsa)	24
Figure 6.15: Wind speed time series and damage volume	25
Figure 6.16: Flapwise and Spanwise displacement of the blade.....	26
Figure 6.17: Progressive Failure Analysis of layer 6 (Balsa)	27

List of Tables

Table 2. 1 Summary of the grades obtained by each theory evaluated in the WWF exercise.....	7
Table 4.1: <i>Material Code</i> and in-plane elastic properties [8]	7
Table 4.2: <i>Layup Code</i> mapping (detailed in Appendix C). <i>Layup Code 16</i> , not included in this table, represents the internal shear-web’s layup.	7
Table 4.3: Results for Modal and Linear Static analyses. Error measures relate Models 1 and 2 only.	12
Table 5.1: Material elastic and strength properties	8
Table 5.2: Material layup for the airfoil profile, listed from the outmost to the innermost layer.....	9
Table 6.1: Material elastic and strength properties	18

Nomenclature

x, y, z	Beam's main coordinate system.	$\sigma_{zz}, \sigma_{sz}, \sigma_{nz}$	Axial and shear stresses of the shell.
U, V, W	Beam's pole displacements with respect to the x, y, z system, respectively.	σ_{ij}	Stress: Longitudinal (11), Transverse (22), Thickness (33), Shear (12, 23, 13)
φ	Beam's cross-section rigid body rotation with respect to the z axis.	$\varepsilon_z^0, \kappa_x, \kappa_y,$ $\kappa_\omega, \kappa_{sz}$	Axial strain, biaxial curvatures in the x and y directions, warping and twisting curvature of the beam.
n, s, z	Beam's secondary coordinate system, located at the shell's mid-surface.	$N_z, M_y, M_x,$ M_ω, M_t, T V_x, V_y	Internal axial, bending, bimoment, torsional and shear loads with respect to the pole.
$\bar{u}, \bar{v}, \bar{w}$	Shell's mid-surface displacements with respect to the x, y, z system	E_{11}, E_{22}	Longitudinal and transverse in-plane Young modulus.
u, v, w	Shell displacements with respect to the x, y, z system.	G_{12}, ν_{12}	In-plane shear modulus and poisson number.
θ	Angle relating the x, y and n, s coordinate systems	S_{ij}^k	Strength. $k = c$: compression, t : tension, s : shear. $ij = 11$: Longitudinal, 22 : Transverse, 33 : Thickness, 12 : Shear
p	Pole, origin of the x, y system for each cross section.	\bar{Q}_{ij}^*	Material stiffness in the global (x, y, z) system.
r, q	Vectors relating the x, y and n, s coordinate systems (parallel to n, s axes respectively).	$[E_{ij}]$	Cross-section stiffness matrix.
w_ω	Warping Displacement	$[M], [K],$ $[C]$	Finite element mass, stiffness and damping matrix.
$F(n, s)$	Complete Warping function.	$\{f\}$	Finite element load vector.
ω_1, ω_2	Primary and Secondary warping functions.	$f_{edge-wise},$ $f_{flap-wise},$ $f_{torsional},$ $f_{axial},$ M_x, M_y, M_ω	External loads applied on the blade.
ω_{2a}, ω_{2b}	First and Second terms of secondary warping for closed sections.	$\{u\}$	Finite element nodal displacement vector.
t	Shell thickness.	α	Attack angle
G_{sz}	Tangential shear stiffness.	β	Blade's twist angle
$\gamma_{xz}, \gamma_{yz},$ γ_ω	Transverse and warping shear strains.	$\varepsilon_{zz}, \gamma_{sz}, \gamma_{nz}$	Axial and shear strains of the shell.
$\psi_x, \psi_y, \psi_\omega$	Rotations of the cross-section with respect to x, y, ω_1 respectively.		

Chapter 1.

Introduction

Chapter Summary

Wind energy is the fastest growing energy source in the world. This chapter introduces the increasing importance of improving the design of wind turbine rotor, particularly in multiphysical scenarios which requires sophisticated computational tools. After some introductory remarks the blades damage assessment is explained and research opportunities are discussed. Finally, the objectives of the thesis are defined along with the current accomplishments.

1.1. Background

Concerns are rising as the price of fossil fuel is escalating and emissions from non-renewable energy sources are significantly polluting the environment. There is evidence suggesting that grave anthropomorphic climate changes could take place, a motivating factor as our society is starting to replace traditional energy production processes with others capable of reducing greenhouse gas (GHG) emissions, responsible of the global warming. Moreover, the scarcity of fossil fuels [1,2] and their unstable price is negatively impacting society, leading to destabilize national economies.

This situation has stimulated the growth of the use of renewable energy resources to replace and complement non-renewable sources, and wind energy is a fast growing alternative for a sustainable future. In 2010, installed wind power capacity reached 197 gigawatts, satisfying about 2.5% of the world's energy demand [3], and expected to rise to 9.1% by 2020 [4]. Figure 1.1 illustrates the exponential growth trend of recent years.

GLOBAL ANNUAL INSTALLED WIND CAPACITY 1996-2010

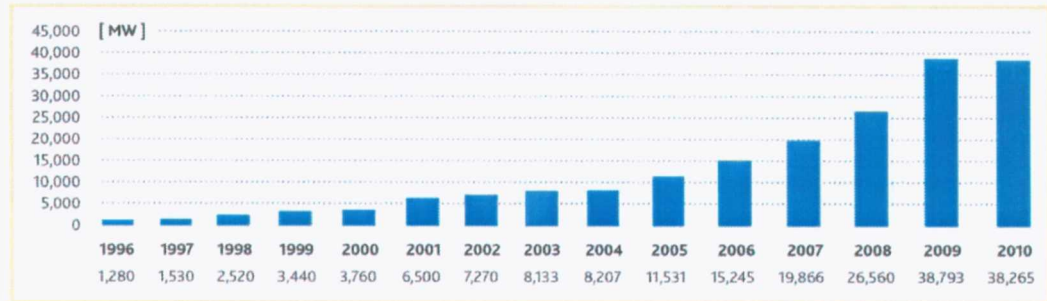


Figure 1.1: Global annual installed wind capacity 1996-2010 [3]

This fast growth is achieved by both expansion in space occupied by wind turbines (including offshore wind farms), and, as technology gradually improves, an increase in rotor size, which allows higher energy capture for a given generator size and reduces overall energy production cost [5]. Figure 1.2 summarizes the growth of commercial wind turbine size and speculates about trends for the near future.

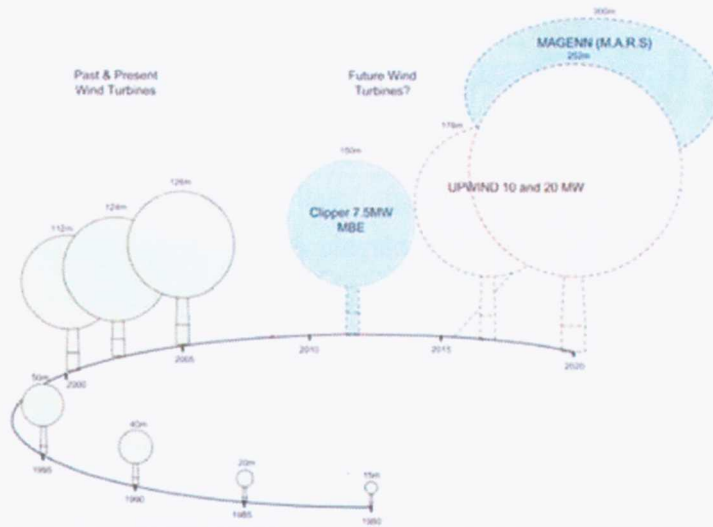


Figure 1.2: Rotor size evolution of wind turbines [6]

1.2. Wind Turbine Damage Assessment

Among others, offshore installations location and larger blade size impose severe operational conditions to wind turbine rotors due to high static and dynamic wind loads. The design of large, flexible and slender blades require abandoning traditional tools (static analysis, uniform inflow, etc.) in favour of advanced dynamic simulations coupling unsteady aerodynamic loads with structural elements to predict realistic wind turbine response [7]. Recent investigations [7-15] describe the current state-of-the-art in aeroelastic analyses in some detail, the success of which highly depends on the structural model's ability of reproducing static and dynamic behaviour under complex aerodynamic flow conditions. To this end, finite element (FE) and modal models are two main approaches. Due to the very extensive computational resources required in aeroelastic simulations, finite element representations are limited in practice to 1D classical beam models, which have the potential to reduce the size of the analyzed system down to a few dozens of degrees-of-freedom (DOF) albeit at the expense of accuracy and loss of detail due to the simplification of geometry and material layup [16]. On the other hand, modal approaches rely on linear mode superposition for representing overall structural behaviour, and their accuracy depends on generating sufficiently refined mode shapes for different rotor speeds [17].

It is important to couple the structural dynamic model of the blade with reliable damage models to determine when and how the material degrades and fails. In addition to improved design, for structural health monitoring purpose the availability of advanced computational models that accounts for damage progression would allow going from scheduled based maintenance to conditional based maintenance, clearly reducing the significant inspection costs [18,25,26]. Currently, the structural integrity of the blade is assessed based on results provided by aeroelastic simulations in tandem with experimentally-obtained or theoretically-derived damage/failure models [8,19-22]. However, computational demands of the interaction between damage progression and aeroelastic response easily exceeds available computing power in design labs.

Current approaches for modelling composite blade's dynamic behaviour in aeroelastic codes (via classical 1D FE-beam and modal models) use condensed mechanical and

geometrical properties, therefore it is very difficult if not impossible to track damage progression on a layer-by-layer basis. A further difficulty is that the blade's rigidity must be updated at individual layers whenever a damage event takes place, which in turn affects wind aerodynamic loads. Thus, detailed 2D or 3D FE models, easily involving several thousands of DOFs [23-24], are impractical in real-life's aeroelastic Progressive Failure Analysis (PFA). For this reason, practical 1D FE models must have the ability of recovering shell's strain and stress three-dimensional fields in order to evaluate damage progression in the whole structure. Thin-walled beam (TWB) models provide an effective one-dimensional representation of the dynamics of a composite structure, while allowing recovering the layer-resolved strain and stress fields to evaluate structural damage progression.

There is little work documented in literature on the combination of beam FE models, recovery of shell strains/stresses and damage tracking. Li [8] in her doctoral thesis uses the VABS methodology [16] in combination with a damage model to optimize the structural properties of a helicopter rotor blade. She first calculates the strain/stress distributions in the blade for a typical helicopter maneuver and then performs an offline fatigue damage analysis for the complete aeroelastic time series generated from a multi-body dynamic software package. In case non-acceptable damage occurs the design is revised and newly subjected to a failure analysis; otherwise the design is deemed to be appropriate. While this approach allows for blade optimization in complex aeroelastic situations it does not provide a platform for integrated damage progression analysis, where the structural properties of the blade are continuously updated while damage progresses.

Pawar and Ganguli [25] described an integrated damage model obtained by combining a matrix-cracking damage model developed by Gudmundson et al [27-28], ply de-bonding/de-lamination and fibre-breakage models developed by Shahid and Chang [29], and a TWB model developed by Chandra and Chopra [30]. In their work the authors obtained relationships between the blade response and damage densities. A static load is applied to the rotor blade and the structural response of the blade as a function of the damage level is calculated. In a follow-up paper [26] Pawar and Ganguli studied the effect of the damage level on the natural frequencies of a rotating thin-walled beam. In both papers the stated objective of the authors lies with structural health monitoring, requiring a

relationship between the global damage level and the static and dynamic response of a blade. The authors do not provide, however, a model capable of predicting damage progression as a function of applied load or spatial distributions of the damage in response to a given load. Although these results could be valuable for ground-based health monitoring equipment, applicability for design purposes and life assessment is rather limited.

1.3. Scope and Approach

Based on the aforementioned exposition, the purpose of this work is to implement a Progressive Failure Analysis (PFA) into a computationally-attractive composite Thin-Wall Beam (TWB) Finite Element (FE) model subject to operational (gravitational, centrifugal and aerodynamic) loads during an aeroelastic simulation. The aerodynamic loads are obtained via Blade Element Momentum (BEM) theory [31].

The selected TWB model was originally developed by Librescu and co-workers [32-35], subsequently discretized via FE by Vo and Lee [36-38], and later specialized for the case of a generic turbine blade by Cárdenas et al.[39]. This TWB model allows inclusion of material anisotropy, arbitrary laminate lay-ups, and shear deformability, thus being able to represent fundamental structural behaviour of complex 3D shell or solid FE models with reasonable accuracy [39]. Stress/strain fields for individual layers can be recovered based solely on nodal FE displacement solutions, thus allowing PFA at any layer and position of the structure.

A further advantage is the availability of analytical expressions for arbitrary cross-section's stiffness, making damage tracking a more straightforward task during a displacement-based FE analyses.

To perform the PFA the failure criteria implemented are the one by GENOA, commercial software specialized in composite failure analysis [40], which main features are described in Chapter 2.

1.4. Organization of Contents

- Chapter 2 presents a literature review of the models used to predict and progress damage in composite material. Special attention is paid in describing Genoa, the computational platform using shell finite elements that used to compare the proposed TWB based progressive damage predictions.
- Chapter 3 describes the theory of the TWB and explains the model shells capabilities.
- Chapter 4 presents a numerical validation of a thin-wall beam (TWB) finite element (FE) model of a realistic wind turbine rotor blade. Static and dynamic results predicted by the TWB are compared against a model created using an higher order shell model.
- Chapter 5 describes the implementation of the progressive failure analysis into the TWB modeling framework. The damage predicted by the TWB model due to static loads are compared those calculated using a higher order shell element model.
- Chapter 6 illustrates the platform created for the modeling of dynamic damage propagation in complex composite structures and provides selected exemplary cases simulating the rotor in parked and rotating conditions.
- Chapter 7 provides concluding remarks and recommendations and a future outlook.

References

- 1 Fingar T. Global Trends 2025:A Transformed World. National Intelligence Council Report. USA. 2008
- 2 Hoel M, Kverndokk S. Depletion of fossil fuels and the impacts of global warming. Resource and Energy Economics. Volume 18, Issue 2, June 1996, Pages 115-136
- 3 <http://cleantechnica.com/world-wind-power/2/> (accessed 20-nov-2011)
- 4 <http://www.europeanenergyreview.eu/site/pagina.php?id=2434> (accessed 20-nov-2011)
- 5 Chia Chen Ciang, Jung-Ryul Lee and Hyung-Joon Bang. Structural health monitoring for a wind turbine system: a review of damage detection methods. Meas. Sci. Technol. 19 (2008) 122001 (20pp)
- 6 Philip Wong Too, Peter Jamieson, Ollie Manins, William Thorp. Trends in wind turbine technology. Garrad Hassan. April 2009
- 7 M.O.L. Hansen, J.N. Sorensen, S. Voutsinas, N. Sorensen, H.A. Madsen. State of the art in wind turbine aerodynamics and aeroelasticity. Progress in Aerospace Sciences 42 (2006) 285–330
- 8 Li L. Structural design of composite rotor blades with consideration of manufacturability, durability and manufacturing uncertainties. Doctoral Thesis in School of Aerospace Engineering. Georgia Institute of Technology. August 2008
- 9 H. Shahverdi, A.S.Nobari, M.Behbahani-Nejad, H.Haddadpour. Aeroelastic analysis of helicopter rotor blade in hover using an efficient reduced-order aerodynamic model. Journal of Fluids and Structures 25 (2009) 1243–1257
- 10 P. Friedmann, B. Glaz, R. Palacios, A moderate deflection composite helicopter rotor blade model with an improved cross-sectional analysis. International Journal of Solids and Structures 46 (2009) 2186–2200
- 11 S. Murugan, R. Chowdhury, S. Adhikari, M.I. Friswell. Helicopter aeroelastic analysis with spatially uncertain rotor blade properties. Aerospace Science and Technology (2011)
- 12 J.M. Jonkman and P.D. Sclavounos. Development of Fully Coupled Aeroelastic and Hydrodynamic Models for Offshore Wind Turbines. ASME Wind Energy Symposium Reno, Nevada January 10–12, 2006

- 13 Ahlstrom A. Aeroelastic simulation of wind turbine dynamics. Doctoral thesis in Structural Mechanics, KTH, Sweden, 2005.
- 14 M.L. Buhl, A. Manjock. A Comparison of Wind Turbine Aeroelastic Codes Used for Certification. 44th AIAA Aerospace Sciences Meeting and Exhibit, Reno, Nevada, January 9–12, 2006
- 15 P. Passon, M. Kühn, S. Butterfield, J. Jonkman, T. Camp, T.J. Larsen. Benchmark Exercise of Aero-Elastic Offshore Wind Turbine Codes. EAWE Conference, Lyngby, Denmark, August 28–31, 2007
- 16 Volovoi V, Hodges D.H, Cesnik C.E.S, Popescu B. Assessment of beam modelling methods for rotor blade applications. *Mathematical and Computer Modelling* 2001; 33: 1099-1112
- 17 Jason M. Jonkman, Marshall L. Buhl Jr. FAST User's Guide. Technical Report NREL/EL-500-38230, August 2005.
- 18 Chia Chen Ciang, Jung-Ryul Lee, Hyung-Joon Bang. Structural health monitoring for a wind turbine system: a review of damage detection methods. *Meas. Sci. Technol.* 19 (2008) 122001 (20pp)
- 19 D. White. New Method for Dual-Axis Fatigue Testing of Large Wind Turbine Blades Using Resonance Excitation and Spectral Loading Technical Report NREL/TP-500-35268, April 2004
- 20 Mahmood M. Shokrieh, Roham Rafiee. Simulation of fatigue failure in a full composite wind turbine blade. *Composite Structures* 74 (2006) 332–342
- 21 R.P.L. Nijssen. Fatigue Life Prediction and Strength Degradation of Wind Turbine Rotor Blade Composites. Doctoral Thesis in Design and Production of Composite Structures. Delft University of Technology 2006
- 22 J.C. Marin, A. Barroso, F. Paris, J. Canas. Study of fatigue damage in wind turbine blades. *Engineering Failure Analysis* 16 (2009) 656–668
- 23 Laird D, Montoya F. Finite Element Modeling of Wind Turbine Blades Sandia National Laboratories, Albuquerque 2005
- 24 Bonnet P, Dutton G. Parametric Modeling Of Large Wind Turbine Blades. Abaqus UK Regional User Meeting. Didcot, Oxon. Energy Research Unit – STFC Rutherford Appleton Laboratory

- 25 P. M. Pawar, R. Ganguli. Modeling progressive damage accumulation in thin walled composite beams for rotor blade applications. *Composites Science and Technology* 66 (2006) 2337–2349
- 26 P. M. Pawar, R. Ganguli. On the effect of progressive damage on composite helicopter rotor system behavior. *Composite Structures* 78 (2007) 410–423
- 27 Adolfsson E, Gudmundson P. Matrix crack induced stiffness reduction in $[(\theta_m/90)_n / + \theta_p / - \theta_q]_s$ composite laminates. *Compos Eng* 1995;5:107–23.
- 28 Gudmundson P, Zang W. An analytic model for thermoelastic properties of composite laminates containing transverse matrix cracks. *Int J Solids Struct* 1993;30(23):3211–31.
- 29 Roberts SJ, Evans JT, Gibson AG, Frost SR. The effect of matrix microcracks on the stress–strain relationship in fiber composite tubes. *J Composite Mater* 2003;37(17):1509–22.
- 30 Chandra R, Chopra I. Structural response of composite beams and blades with elastic couplings. *Compos Eng* 1992;2(5–6):347–74.
- 31 H. Madsen, R. Mikkelsen, S. Øye, C. Bak, J. Johansen. A Detailed investigation of the Blade Element Momentum (BEM) model based on analytical and numerical results and proposal for modifications of the BEM model *Journal of Physics: Conference Series* 75 (2007) 012016
- 32 Song O, Librescu L, Jeong NH. Static response of thin-walled composite I-beams loaded at their free-end cross-section: analytical solution. *Composite Structures* 2001; 52: 55-65.
- 33 Librescu L, Na S. Active vibration control of doubly tapered thin-walled beams using piezoelectric actuation. *Thin-Walled Structures* 39 (2001) 65–82
- 34 Qin Z, Librescu L. On a shear-deformable theory of anisotropic thin-walled beams: further contribution and validations. *Composite Structures* 56 (2002) 345–358
- 35 Librescu L, Song O. *Thin-walled Composite Beams: Theory and Application*. Springer, 2006
- 36 Vo T., Lee J. Flexural torsional behavior of thin walled closed-section composite box beams. *Engineering Structures* 2007; 29: 1774-1782
- 37 Lee J. Vo T., Flexural–torsional behavior of thin walled composite box beams using shear-deformable beam theory. *Engineering Structures* 30 (2008) 1958–1968
- 38 Vo T., Lee J. Free vibration of thin-walled composite box beams. *Composite Structures* 84 (2008) 11-20

39 D. Cárdenas, H. Elizalde, P. Marzocca, O. Probst. Numerical validation of a finite element thin-walled beam model of a composite wind turbine blade Article first published online: 18 MAR 2011 DOI: 10.1002/we.462 Wind Energy 2011

40 <http://www.ascgenoa.com/main/> (accessed 20-nov-2011)

Chapter 2.

Damage in Composite Materials

Chapter Summary

A literature review of the type of models used to predict damage in composite is presented in this chapter. The ranking of their ability to describe the response and failure behavior of various laminates under a broad of loading conditions is based on the Worldwide Failure Exercise. Finally, an pertinent details related to Genoa and its failure criteria are provided.

2.1. Failure criteria review

Typically, wind turbine blades are constructed from fibre reinforced polymers, due to their high stiffness-to-density and strength-to-density ratios and good fracture toughness [1]. Continuous glass-fibre composites are preferred due to lower cost, although designers are moving towards stiffer carbon fibres as they are slowly becoming affordable for the wind industry [2]. As the materials used are significantly cheaper than aerospace materials, their defects which might lead to structural damage are a critical concern. There is a strong need for composite failure criteria and degradation models which are simple enough for application in common engineering problems while still being in good agreement with physical evidence. In contrast with isotropic metallic materials, failure criteria for composites must account for inherent anisotropy and many other particularities in order to achieve an accurate prediction. Most of available failure criteria create a geometric envelope within a tensor space (stress, strain), where the region inside the envelope represents a damage-free zone

In his PhD thesis [3], Arellano-Escarpita presents a literature review of failure criteria for composite materials based on [4-5]. They are classified them as: parametric, phenomenological, micromechanics, and probabilistic. Figure 2.1 shows the rate of use among the design engineers for different failure models. The phenomenological and parametric failure models are the most popular due its simplicity and relative good accuracy.

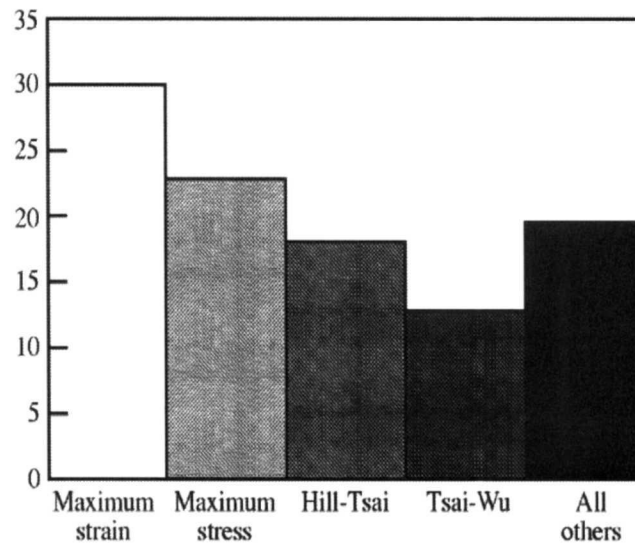


Figure 2.1: Rate of use among composite designer for different failure criteria [4]

2.1.1. Parametric failure criteria

Parametric criteria are based on empirical data and they are described in [3] as a mathematical expression to fit a failure envelope generated by experiment results. Tsai-Hill and Tsai-Wu are the most known criteria in this category and its popularity is due to their success predicting certain failure conditions and relative simplicity of implementation (see Figure 2.1). The shortcoming of the parametric criteria, which limit their extrapolation, is the fact that they do not distinguish among failure modes and they do not offer a physical explanation for damage's nucleation and progression [3]. The failure envelope given by Tsai-Wu [4-5] for plane-stress orthotropic materials is:

$$K_1\sigma_{11} + K_2\sigma_{22} + K_{11}\sigma_{11}^2 + K_{22}\sigma_{22}^2 + K_{66}\tau_{12}^2 + 2K_{12}\sigma_{11}\sigma_{22} = 1 \quad \text{Eq. 2.1}$$

where:

$$K_1 = \frac{1}{S_{11}^t} - \frac{1}{S_{11}^c}; \quad K_2 = \frac{1}{S_{22}^t} - \frac{1}{S_{22}^c}; \quad K_{11} = \frac{1}{S_{11}^t S_{11}^c}; \quad K_{22} = \frac{1}{S_{22}^t S_{22}^c}$$

$$K_{66} = \frac{1}{(S_{12}^s)^2}; \quad K_{12} = \frac{F_{12}^*}{\sqrt{S_{11}^t S_{11}^c S_{22}^t S_{22}^c}} \quad \text{Eq. 2.2}$$

S represent the material's strength limit while the upper indices *t*, *c*, *s* indicate tension, compression, and shear, respectively; sub-indexes 11, 22 and 12 correspond to directions parallel, transversal and in-plane to the fibre. The bilinear interaction parameter (F_{12}^*) ranges between 1 and -1, the specific value being determined by the properties of each laminate; usually a value of -0.5 is used in absences of data reported by literature [3].

A modification of the Tsai-Wu criterion is the Tsai-Hill [4-5] and the difference is the definition of a piece-wise failure envelope for each quadrant:

$$K_1 = 0; \quad K_2 = 0; \quad K_{11} = \frac{1}{S_{11}^j}; \quad K_{22} = \frac{1}{S_{22}^j}$$

$$K_{66} = \frac{1}{(S_{12}^s)^2}; \quad K_{12} = -\frac{1}{2(S_{11}^j)^2} \quad \text{where } j = \begin{cases} c; \text{compression} \\ t; \text{tension} \end{cases} \quad \text{Eq. 2.3}$$

Tsai-Hill defines a specific set of parameters which depends on the nature of the load (tensile or compressive).

2.1.2. Phenomenological failure criteria

Phenomenological criteria are based on the understanding of the material's failure modes at the macroscopic level and they address each mode separately. Examples of this category are [3]:

a. Maximum Stress and Maximum Strain Criteria [3]. They can be considered the most used criteria due their simplicity (see Figure 2.1). Those criteria predict failure when some of the stress or strain components in a given direction reach a threshold value determined by uni-axial experiments. The following equations defines when the failure occurs:

$$f_{max. stress} = \max \left\{ \left| \frac{\sigma_{11}}{S_{11}^t} \right|, \left| \frac{\sigma_{11}}{S_{11}^c} \right|, \left| \frac{\sigma_{22}}{S_{22}^t} \right|, \left| \frac{\sigma_{22}}{S_{22}^c} \right|, \left| \frac{\sigma_{12}}{S_{12}^s} \right| \right\} \geq 1 \quad Eq. 2.4$$

$$f_{max. strain} = \max \left\{ \left| \frac{\varepsilon_{11}}{\varepsilon_{11}^t} \right|, \left| \frac{\varepsilon_{11}}{\varepsilon_{11}^c} \right|, \left| \frac{\varepsilon_{22}}{\varepsilon_{22}^t} \right|, \left| \frac{\varepsilon_{22}}{\varepsilon_{22}^c} \right|, \left| \frac{\gamma_{12}}{\gamma_{12}^s} \right| \right\} \geq 1 \quad Eq. 2.5$$

The composite material fails when $f \geq 1$. The main shortcoming of this kind of criteria is the non interaction among multi-axial stresses.

b. *Hashin-Rotem criterion* [3]. This criterion can distinguish among failure modes associated to matrix or fibres separately and the failure occurs according with the following equation:

$$f = \begin{cases} \frac{\sigma_{11}}{S_{11}^j} \geq 1 \\ \left(\frac{\sigma_{22}}{S_{22}^j} \right)^2 + \left(\frac{\sigma_{12}}{S_{12}^s} \right)^2 \geq 1 \end{cases} \quad \text{where } j = \begin{cases} c; \text{compression} \\ t; \text{tension} \end{cases} \quad Eq. 2.6$$

c. *LaRC04*. In [3] this approach is considered one of the best criteria due to its capability for predicting relatively accurate failure envelopes for a wide array of load conditions, specifically compression and shear. LaRC04 criteria consist on a set of six independent equations, each corresponding to a specific failure mode. The full sets of equations and their description, which conforms LaRC04 can be found in [6]:

2.1.3. Micromechanics strength prediction

According to [3], the micromechanical approaches model separately the fibres and matrix of the composite to predict overall mechanical properties (elastic modulus and strength) as well as failure onset. The simplest models consider isotropic, linear elastic and perfect aligned fibres in the matrix with no discontinuities at interfaces. However, they have some limitations calculating transverse modulus due to the stress concentration around the fibres. A More advanced model [7] solves this limitation and it is based on analytical solutions of stress/strain fields coupling the deformation of an ellipsoid (fibre) surrounded

by a matrix. In the case of textile composite, [3] recommends the use of a 3D FEM approach due to their entangled geometry [8-10]. One of the most successful methods based on micromechanical-FE approach is the Multi-Continuum Theory (MCT), capable of describing the multiple phases which co-exist in a single material point [9-10].

2.1.4. Probabilistic criteria

The last failure criteria category described in [3] are probabilistic type. This approach generates failure envelopes using statistical methods based on experimental tests. The criteria generated by this method don't consider any interaction among individual constituents. However, it is possible to generate a complex failure envelope to fit precisely experimental data. The disadvantage of this approach, similarly to the parametric method, is the inability to extrapolate to different load cases. The failure criteria of Kriging [4] are an example of a statistical approach.

2.2. Failure criteria evaluation

A comprehensive comparison of laminate failure models was established to assess the state-of-the-art in laminate modeling technologies (known as the Worldwide Failure Exercise) [11]. In mentioned study, Hinton, Kaddour and Soden compare 19 models to predict laminate response and failure behavior of various laminates under a broad range of loading conditions.

2.2.1. Characteristic of the theories

The authors [11] describe the principal key features of the evaluated theories as:

- *Method of analysis:* Theories are divided between those which use FE together with Classical Laminate Theory as the main approach and the rest which use only (CLT).
- *Type of analysis:* This feature refers to whether the author of the theory considers linear or nonlinear material properties.

- *Modes of failure:* In this category, the authors grouped to the level of ability of the theories to identify specific modes of failure during the loading event. At least almost all theories are able to identify between two or more mode of failure: a) fibre failure (tension, compression or shear), b) matrix failure (transverse tension, transverse compression, shear or a combination of them). The modes of failure are predicted using the lamina properties with exception of Mayes, Huang and Chamis which use the constituent fibre and matrix properties.
- *Micromechanics:* This feature describes whether the theory is based on a micromechanical approach. About half of the theories employ micro mechanics in their formulation
- *Post-initial failure degradation models:* Some of the theories specify a degradation model to account for post initial failure behavior. Once the first ply failure or initial failure has occurred, the multidirectional laminates are still capable to carry load. Modelling the post failure behavior of a laminates requires certain assumptions to degrade the properties of the failed lamina. For further details of the post failure models it is necessary referring to [11]. Hinton and colleagues classified into the three main groups the post failure methods:
 - a) Models employing no post failure analysis.
 - b) Models employing sudden reduction in the properties of the failed lamina.
 - c) Models employing a gradual drop in the properties of the failed lamina.

2.2.2. Ranking of theories

In order to assess the predictive capabilities of the theories, Hinton and colleagues complete a systematic comparison of the predicted results against experimental evidences. The authors selected 125 cases which covered five ranking categories [11]:

1. Biaxial strength of unidirectional lamina.
2. 'Initial' biaxial strengths of multi-directional laminates.
3. 'Final' strengths of multi-directional laminates.
4. Deformation (stress-strain curves) of multi-directional laminates.
5. Ability to predict the general trends observed in the test data.

and described the scoring system rules applied to these cases, as follows:

- Grade A (i.e. the prediction lies within $\pm 10\%$ of the experimental value).
- Grade B (i.e. the prediction lies between $\pm 10\%$ and $\pm 50\%$ of the experimental value).
- Grade C (i.e. the prediction lies below 50% or above 150% of the experimental value).
- Grade NA (i.e. no solution offered).

Table 2.1 Summary of the grades obtained by each theory evaluated in the WWF exercise.

Theory	Grade type				
	A	B	C	NA	A+B
Zinoviev	53	43	29	0	96
Bogetti	51	44	30	0	95
Puck	64	30	31	0	94
Cuntze	62	32	31	0	94
Tsai	50	35	40	0	85
Sun(L)	52	31	42	0	83
Edge	50	32	43	0	82
Huang	42	38	45	0	80
Mayes	52	27	46	0	79
Wolfe	39	31	55	0	70
Hart-Smith3	39	30	41	15	69
Chamis	44	24	53	4	68
Rotem	37	30	58	0	67
Hart-Smith1	41	16	23	45	57
Hart-Smith2	36	19	25	45	55
Sun(NL)	21	17	21	66	38
Eckold	20	14	48	43	34
McCartney	10	4	4	107	14
Cuntze-B	59	38	28	0	97
Tsai-B	57	36	32	0	93
Mayes-B	58	33	34	0	91
Wolfe-B	53	32	40	0	85
Edge-B	51	34	40	0	85
Huang-B	43	37	45	0	80
McCartney-B	26	13	19	67	39

In Table 2.1 are summarized the grades scored by the theories evaluated in the WWF exercise. The maximum grade to score is 125. The authors claim that the result of this comparison highly depends on the accuracy of the experimental predictions. Additionally they accept that even when they applied relatively strict rules to rank the theories, it is possible that some of the strengths and weaknesses of each of the theories could be not noticed unintentionally.

2.3. GENOA (Chamis model)

2.3.1. Software description

Among all damage theories found in literature, only that of Chamis and Mayes (MCT) are already incorporated into commercial FE codes to predict the failure behaviour of complex composite structures [11]. Chamis and Minnetyan implemented this model in CODSTRAN [12], which later evolved into GENOA [13], which is Progressive Failure Analysis (PFA) software by AlphaStar Corporation. For this reason, same criteria were chosen for the progressive failure analysis based on the TWB model developed in this thesis. This enabled a side-by-side comparison with a 3D Shell FE GENOA model, at least for the static loading cases.

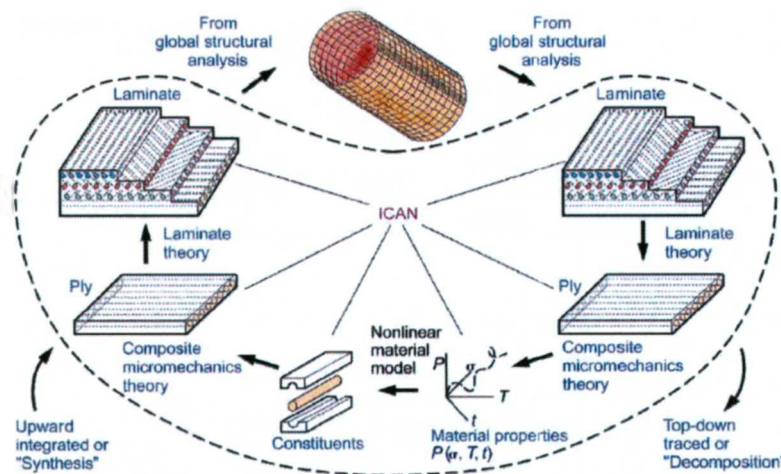


Figure 2.2: CODSTRAN simulation cycle [12]

Composite Durability Structural Analysis (CODSTRAN), which is the previous version of GENOA, is a computer code consisting of three modules: composite mechanics, FE analysis, and damage progression modelling. Figure 2.2 shows a schematic of the computational simulation cycle in CODSTRAN. The Integrated composites analyzer (ICAN) module [14] is recalled before and after each FE analysis. First, the ICAN module computes the composite properties from the fibre and matrix constituent characteristics and the composite layup. Then, the FE module accepts the composite properties at each node and performs the analysis at each load increment, computing nodal forces and deformations of the FEM model. This information is supplied to the ICAN module which evaluates the amount and nature of local damage, if any, in all plies of the composite laminate. Individual ply failure modes are assessed by ICAN using failure criteria associated with the negative and positive limits of the six ply-stress components in the material directions, as follows:

$$\begin{aligned} S_{11}^c < \sigma_{11} < S_{11}^t \\ S_{22}^c < \sigma_{22} < S_{22}^t \\ S_{33}^c < \sigma_{33} < S_{33}^t \\ S_{12(-)}^s < \sigma_{12} < S_{12(+)}^s \\ S_{23(-)}^s < \sigma_{23} < S_{23(+)}^s \\ S_{13(-)}^s < \sigma_{13} < S_{13(+)}^s \end{aligned} \quad \text{Eq. 2.7}$$

S_{11}^t represents the ply longitudinal tensile strength failure mechanism, which is dominated by fibre's strength, S_{11}^c represents the corresponding compression value, where matrix is more involved. S_{22}^t and S_{33}^t represent the failure mechanism for transverse tension dominated by matrix tensile strength. This is also known as matrix splitting, micro-cracking or interfacial bond failure. S_{22}^c and S_{33}^c represent the failure mechanism for transverse compression dominated by matrix compressive strength. S_{12}^s , S_{23}^s and S_{13}^s represent shear ply failure mechanisms dominated by matrix shear strength and interfacial conditions.

Strengths can be calculated by ICAN based on constituent fibre and matrix strengths and micromechanics equations [14]. In addition to failure criteria based on the above stress limits, the Modified Distortion Energy (MDE) failure criterion is also considered, which takes into account combined stresses [15]. The MDE failure criterion is expressed as:

$$f = 1 - \left[\left(\frac{\sigma_{L11\alpha}}{S_{L11\alpha}} \right)^2 + \left(\frac{\sigma_{L22\beta}}{S_{L22\beta}} \right)^2 - K_{L12\alpha\beta} \frac{\sigma_{L11\alpha}}{S_{L11\alpha}} \frac{\sigma_{L22\beta}}{S_{L22\beta}} + \left(\frac{\sigma_{L12S}}{S_{L12S}} \right)^2 \right] \quad \text{Eq. 2.8}$$

where α and β indicate the tensile or compressive stress, and

$$K_{L12\alpha\beta} = \frac{(1 + 4\nu_{L12} - \nu_{L13})E_{L22} + (1 - \nu_{L23})E_{L11}}{[E_{L11}E_{L22}(2 + \nu_{L12} + \nu_{L13})(2 + \nu_{L12} + \nu_{L23})]^{1/2}} \quad \text{Eq. 2.9}$$

Within this approach failure takes place when $f \leq 0$ and failure modes can be either fibre- or matrix-related, depending on dominance of the magnitudes of the squared terms in Eq. 2.8. Given a fibre-driven failure event, both fibre (E_{1f}) and matrix (E_m) longitudinal moduli are replaced by negligible (instead of zero, to avoid numerical errors) values so that the ply effectively stops carrying load. For a matrix failure, its modulus is replaced with a negligible value ($E_m \approx 0$). Micromechanics relations [14] are used to compute revised properties (longitudinal modulus E_{1l} , transverse modulus E_{22} , shear modulus G_{12} , and Poisson's ratios ν_{L12} , ν_{L13} and ν_{L23}) of the failed lamina. The revised properties are then used to carry out Progressive Failure Analysis. The procedure is repeated until all plies have failed and the laminate cannot carry any more load (see Figure 2.2).

2.3.2. WWF evaluation of Chamis theory

In [11] it is possible to assess the performance of the Chamis theory from the WWF exercise. The comments provided by Hinton and colleagues reflect the result obtained in Table 2.1:

- Chamis theory gives a good description of measured unidirectional lamina failure envelopes.
- The maximum shear stresses observed in experimented combined direct and shear loading are not well predicted for unidirectional lamina.

- The predicted initial failure stresses for multi-directional laminates were lower than the data from experiments and lower compared with the predictions of many other theories.
- The main weakness of the theory is the prediction of laminate behavior where the initial failure occurred at a low stress level but final failure occurred at much larger stress.
- This theory cannot predict non-linear stress-strain curves.
- The overall performance was not quite as good as some other theories.

Although this evaluation provides a good to fair to Chamis theory, with several advantages and drawbacks, the author has implemented this model in the work presented in the following chapters as it provides a mean of comparison with a state-of-the-art finite element code based on this theory.

References

- 1 R.P.L. Nijssen. Fatigue Life Prediction and Strength Degradation of Wind Turbine Rotor Blade Composites. Doctoral Thesis in Design and Production of Composite Structures. Delft University of Technology 2006
- 2 Brøndsted, P., Lilholt, H., Lystrup, A., 'Composite Materials for Wind Power Turbine Blades', *Annu. Rev. Mater. Res.*, Vol. 35, 2005, pp. 505-538
- 3 Escarpita, D. Experimental investigation of textile composites strength subject to biaxial tensile loads. Doctoral Thesis. ITESM, MTY. May 2011
- 4 F. Paris. A Study of Failure Criteria of Fibrous Composite Materials, NASA/CR- 2001-210661, March 2001.
- 5 Echaabi J, Trochu F, Gauvin R. Review of Failure Criteria of Fibrous Composite Materials. *Polymer Composites* 1996; 17(6): 786-798
- 6 Pinho ST, Dávila CG, Camanho PP, Iannucci L, Robinson P. Failure Models and Criteria for FRP Under In-Plane or Three-Dimensional Stress States Including Shear Non-Linearity, NASA/TM-2005-213530, February 2005.
- 7 Hull D, Clyne TW. An introduction to composite materials. 2nd edition. Cambridge University Press, 1996.
- 8 Karkkainen RL, Sankar BV, Tzeng JT. Strength prediction of multi-layer plain weave textile composites using the direct micromechanics method. *Composites: Part B* 2007; 38(7-8): 924-932.
- 9 Key CT, Schumacher SC, Hansen AC. Progressive failure modelling of woven fabric composite materials using multicontinuum theory. *Composites: Part B* 2007; 38(2):247-257.
- 10 Mayes JS, Hansen AC. Multicontinuum Failure Analysis of Composite Structural Laminates. *Mechanics of Composite Materials and Structures* 2001; 8(4): 249-262.
- 11 M.J. Hinton, A.S. Kaddour, P.D. Soden. Failure Criteria in Fibre Reinforced Polymer Composites: The World-Wide Failure Exercise. 2004 Elsevier .ISBN: 0-08-044475-X
- 12 C. Chamis, L. Minnetyan. Defect/damage tolerance of pressurized fibre composite shells. *Journal of Composite Structures* 51 (2001) 159-168
- 13 <http://www.ascgenoa.com/main> (accessed on 20 Nov-2011)

14 P. Murthy, C. Chamis. ICAN: integrated composite analyzer user's and programmer's manual. NASA TP-2515, National Aeronautics and Space Administration, Washington, DC, 1985.

15 K. Gotsis, C. Chamis, L. Minnetyan. Prediction of composite laminate fracture: micromechanics and progressive fracture Composites Science and Technology 58 (1998) 1137-1149

Chapter 3.

Thin-Walled Beam Model

Chapter Summary

The TWB theory is introduced in this Chapter. The basic assumptions of the model are described and the equations needed to recover strains and stresses of any laminate ply at any blade position are presented. The shell capabilities of the TWB model allow a further implementation of failure criteria in order to perform a progressive failure analysis.

Rotor blades, such as the one used on rotorcrafts and wind turbines, are among the most critical structural components of rotor systems, thus advanced tools must be employed at the design and performance analysis stages [1]. The optimization of such components using recursive fluid-structure dynamic simulations of detailed 2D or 3D finite element (FE) models, can easily involve several thousands of degrees-of-freedom (DOF) [2-3]. As it was indicated in earlier chapters, to perform advanced composite blades complex numerical simulations, such as the one involving flow-structure interaction, it is practical to use 1D Beam FE models. Models with the ability of recovering the shell's three-dimensional strain and stress fields are needed to evaluate damage progression in the whole structure during the aeroelastic vibrations. One of the most advanced analysis tools, which is suitable for rotor blade applications, is the Variational Asymptotic Beam Section Analysis (VABS) reported in [4-6]. VABS mathematical basis is the variational-asymptotic method developed in [7] which transforms a general 3D nonlinear elasticity problem of a beam-like structure into a 2D linear cross-sectional analysis and then into a 1D nonlinear beam problem (see Figure 3.1). VABS is capable of capturing the trapeze and Vlasov effects and calculate the 1D sectional properties including transverse shear

refinement. Validations against 3D FE models resulted in a reduced computational effort of three orders of magnitude, with very good agreement for stress/strain results [8].

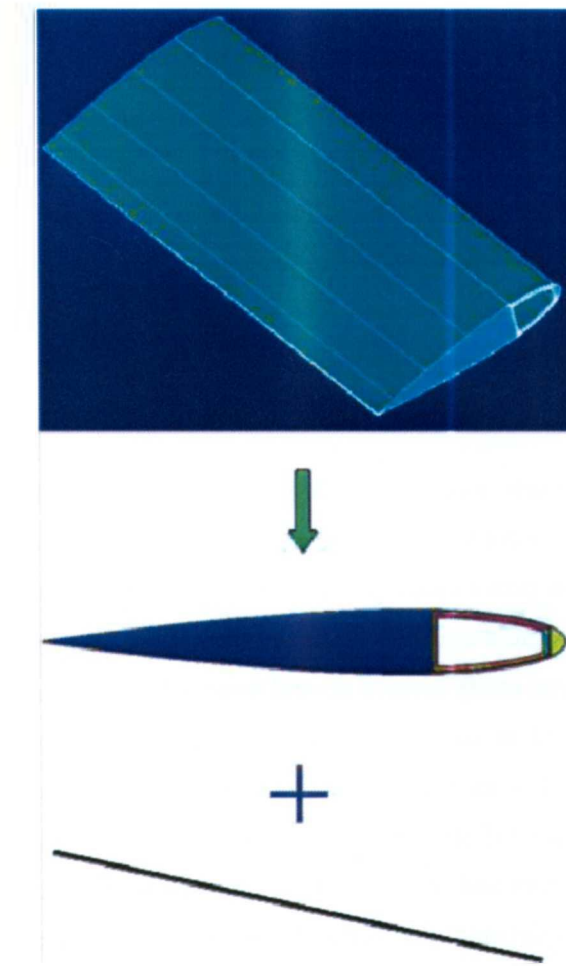


Figure 3.1: Decomposition of a 3D blade problem into a 1D Beam [9]

Despite its advantages, VABS methodology cannot be integrated into an aeroelastic damage progression platform in a straightforward way. VABS required a 2D mesh (see Figure 3.2) of the different cross sectional areas of the structure in order to perform a FE analysis and obtain the sectional stiffness [9]. Once the stiffness parameters of the

transverse areas have been obtained it is possible to reduce the problem to an equivalent 1D beam. Executing a FE analysis whenever a layer is damaged to update the stiffness properties of a transversal area would represent a high recursive computational effort.

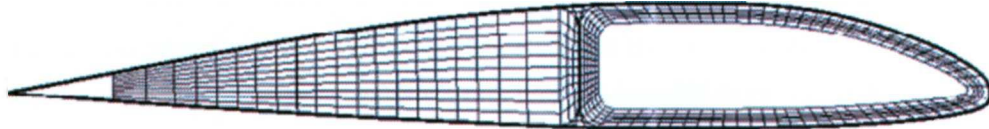


Figure 3.2: Geometry layout and mesh of a cross sectional area used in the VABS approach [9].

In the present work, an alternative approach is pursued, based on the TWB theory developed by Librescu and co-workers [10-12] and subsequently discretized via FE by Vo and Lee [13-16]. This choice is motivated by the fact that Librescu's formulation provides analytical expressions for the stiffness matrixes of the transverse sections which are useful for damage progression analyses during an aeroelastic simulation, although possibly at the expense of a lesser accuracy compared to other formulations, including VABS [4].

The Librescu's theory allows constructing an accurate yet computationally efficient 1D FE beam model capable of retaining most essential features found in generic rotor blades: thin-walled hollow section with variable thickness along the section's contour, inner reinforcements, anisotropic laminates with arbitrary material layup and fiber orientation, transversal shear, etc. Other features, such as tapered section and geometric/material nonlinearities can be incorporated in a straightforward fashion [10-17]. The latter would require only slight modifications to the proposed displacement field, avoiding the small-angle assumption by retaining the full trigonometric expressions, thus yielding a few non-zero Lagrange-type strain terms generate a non-linear stiffness matrix, which must be solved iteratively. Having said this, the present application is, for the time being, restricted to linearity.

The cross-section stiffness is calculated by a double integration of main properties through the thickness and along the shell's contour, so the formulation is able to distinguish properties arising from different regions of the shell (region with damage included). This allows, in principle, full deformation and stress fields to be recovered for post-processing analyses such as advanced composite failure criteria. Moreover, since the cross-section's stiffness is calculated "off-line" once for each, the geometrical and material complexities of the cross-section do not exert influence on element size, as it does on FE models based on shell and solid elements, one of the limitation of the use of VABS approach like to this problem. This is a main feature which impacts directly on computational economy, and make obvious the advantage of using the proposed approach for the problem at hand. Therefore the TWB model was chosen mainly for simplicity, reasonably good accuracy, and its availability in analytical form, which makes this approach physical based.

3.1. Kinematics

Figure 3.3 shows a generic element of a typical wind turbine blade, illustrating main features required for the analysis [10-14]. Each section can be reinforced by one or more shear webs, where the area enclosed by a given closed contour defines a cell. The origin of the main coordinate system (CS) x,y,z is placed at the pole p , defined at the intersection of the beam's cross-section with an arbitrary line running along the radial direction of the beam (parallel to z axis). Displacement of the pole p along the x,y,z coordinates are denoted by U, V, W respectively. ψ_x, ψ_y, ϕ and ψ_ω represents the angular displacement of the cross-section with respect to the x, y, z and warping directions, respectively. A secondary CS s,n,z measures tangential (\bar{u}), normal (\bar{v}) and axial (\bar{w}) displacements of an arbitrary point located on the shell's mid-surface, defined equidistant from the upper and bottom surfaces of the beam's shell (see Figure 3.3). Both CS are related via angle θ and vectors r and q , which are parallel to the n and s axes, respectively. The wall thickness can have an arbitrary circumferential variation (along the contour), as long as it remains thin; this variation is assumed uniform throughout the element's length. It is recommended in [10] the use of the TWB model to structures where the total length is at least 10 times larger than any characteristic dimension of the cross-sectional area.

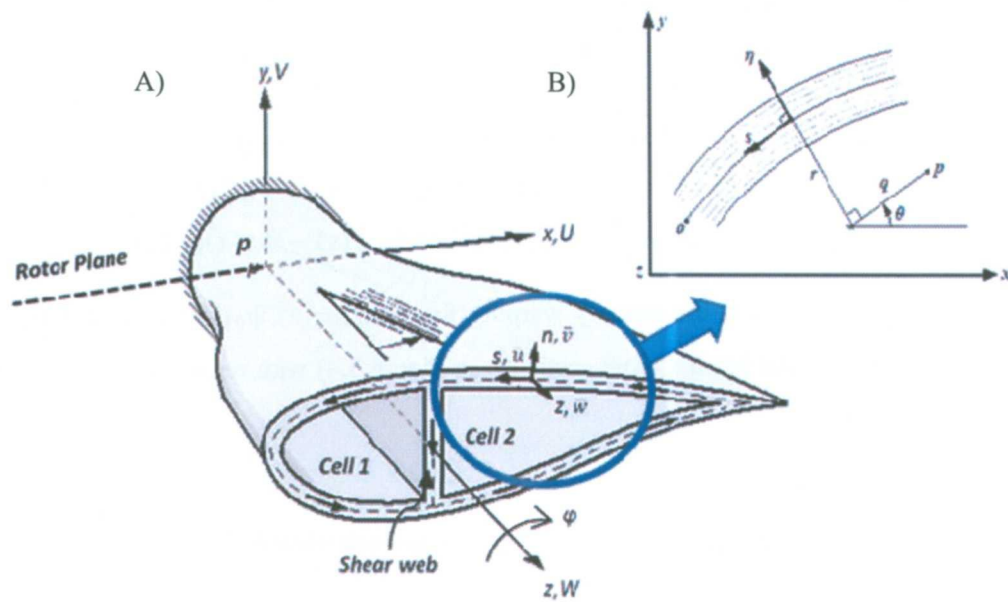


Figure 3.3: A) generic beam element of a wind turbine blade. B) Mid-surface and Coordinate Systems (CS) [29]

The TWB model is based on the following assumptions [14]:

- 1) Small strains.
- 2) The beam's cross-sections do not deform in their own plane.
- 3) Uniformity of the transverse shear strains γ_{xz} , γ_{yz} and warping shear γ_{ω} over the cross-section is assumed. According to [30] the shear effect depends on the boundary conditions and aspect ratio (length of the blade divided by the cross-sectional dimension). The effects become important for aspect ratios smaller than 5.
- 4) The Kirchhoff–Love assumption in classical plate theory remains valid for laminated composites (mid-surface plane is used to represent a 3D plate).

The Based on these assumptions mentioned above, the mid-surface displacement field can be expressed as:

$$\begin{aligned}
 \bar{u}(s, z) &= U(z) \sin \theta(s) - V(z) \cos \theta(s) - \varphi(z)q(s) \\
 \bar{v}(s, z) &= U(z) \cos \theta(s) + V(z) \sin \theta(s) + \varphi(z)r(s) \\
 \bar{w}(s, z) &= W(z) - \psi_y(z)x(s) - \psi_x(z)y(s) - \psi_\omega(z)\omega_1(s)
 \end{aligned}
 \tag{Eq. 3.1}$$

where $\omega_1(s)$ is the primary warping function, $\psi_x(z)$, $\psi_y(z)$ and $\psi_\omega(z)$ represent the rotations of the beam's cross section (see Figure 3.4) with respect to the x , y and z axis given by:

$$\begin{aligned}
 \psi_x &= \gamma'_{yz} - V' \\
 \psi_y &= \gamma'_{xz} - U' \\
 \psi_\omega &= \gamma'_{\omega} - \varphi'
 \end{aligned}
 \tag{Eq. 3.2}$$

The prime (') indicates differentiation with respect to the axial coordinate z . An Euler-Bernoulli beam model (non-shear deformation) is obtained ignoring the transverse shear effect. Eq. 3.2 is then reduced to:

$$\begin{aligned}
 \psi_x &= -V' \\
 \psi_y &= -U' \\
 \psi_\omega &= -\varphi'
 \end{aligned}
 \tag{Eq. 3.3}$$

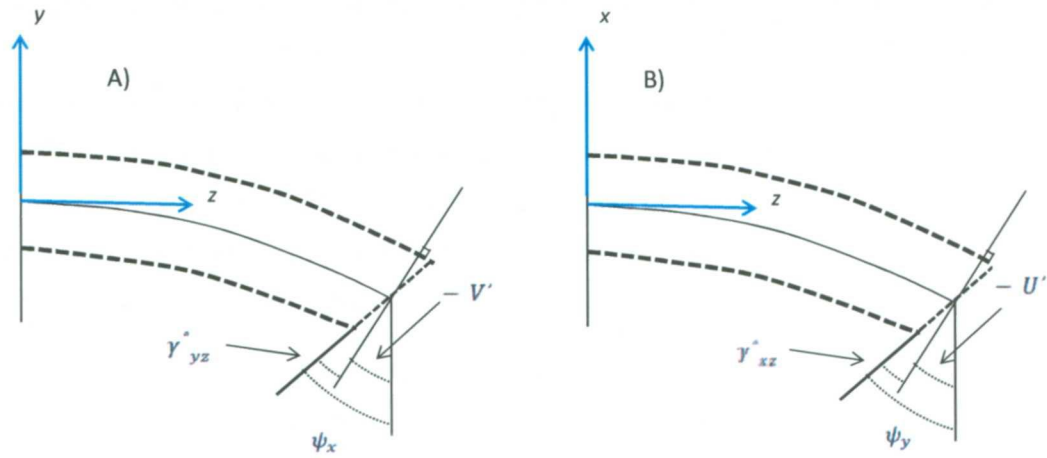


Figure 3.4: Angular displacements of TWB in the yz plane (A) and xz plane (B)

The full displacement field of an arbitrary point of the beam's shell (u, v, w) is related to the mid-surface's $(\bar{u}, \bar{v}, \bar{w})$ by:

$$\begin{aligned}
 u(s, z, n) &= U(z) \sin \theta(s) - V(z) \cos \theta(s) - \varphi(z)q(s) \\
 v(s, z, n) &= U(z) \cos \theta(s) + V(z) \sin \theta(s) + \varphi(z)r(s) + n\varphi(z) \\
 w(s, z, n) &= W(z) + \psi_y(z)[x(s) + n \sin \theta(s)] + \psi_x(z)[y(s) - n \cos \theta(s)] \\
 &\quad + \psi_\omega(z)F(n, s)
 \end{aligned}
 \tag{Eq. 3.4}$$

The term $F(n, s)$ is the complete warping function which is defined in the following section.

3.1.1. Warping theory

An description of warping theory is offered in the master thesis of Aguirre [31], where warping is referred to the out of plane displacement of a cross-section undergoing torsion, which is precluded for certain geometries such as circular cross sections [10]. When the

warping displacements are constrained appears a warping torsional moment which is divided in two [31]:

1. Warping shear stresses (Figure 3.5), acting tangential to the cross-section, constant across the thickness and varying along the contour.
2. Warping normal stresses (Figure 3.6). They arise as a result of constraining compression/tension axial displacements due to torsion of the element. They vary along the contour of the cross-section.

These types of stresses have to be added to the bending and shear stresses already present in the cross-section. The warping stresses are neglected for closed section. However they can be significant in open cross-sections [31].

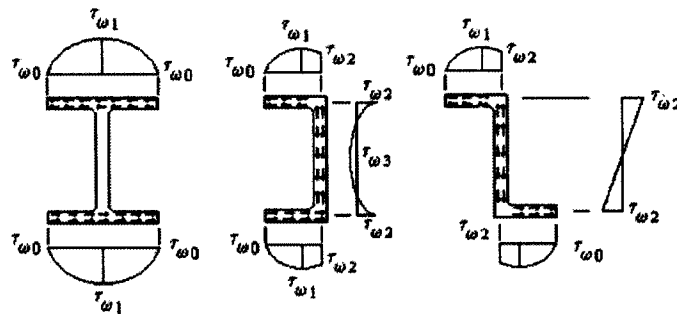


Figure 3.5: Warping shear stresses in some open cross-sections [19].

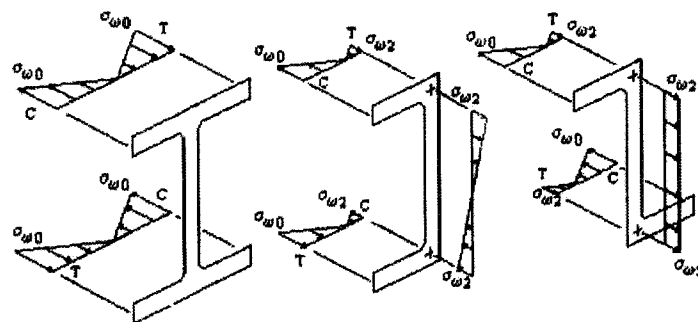


Figure 3.6: Warping Normal Stresses in some open cross-sections [19].

Warping displacements can be split into primary and secondary warping (see Figure 3.7). The former is associated with the (average) mid-surface's motion, while the latter represents the contribution of points off the mid-surface [10,18-21].

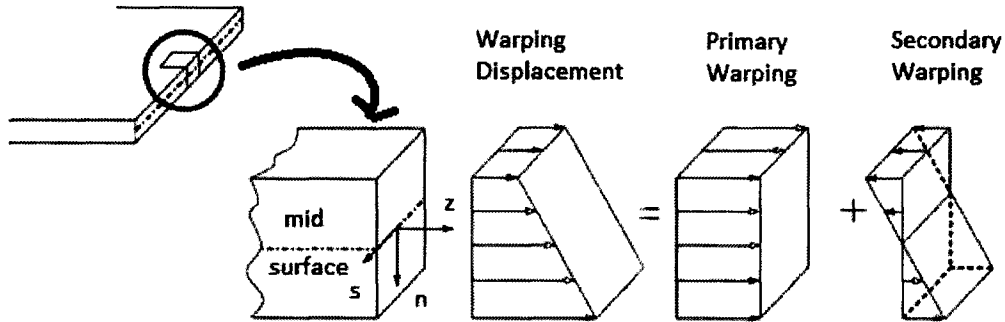


Figure 3.7: Warping displacement behaviour [28].

Librescu formulation for composite thin-walled beams [10], assumes the warping displacement in pure torsion as:

$$w(n, s, z)_\omega = F(n, s)\varphi'(z) \quad \text{Eq. 3.5}$$

where $F(n, s)$ is a total warping function specifically derived for open and closed cross-sections, and $\varphi'(z)$ is the rate of twist of the beam element with respect to the axial beam coordinate. The warping function can be divided into primary ($\omega_1(s)$) and secondary ($\omega_2(n, s)$):

$$F(n, s) = \omega_1(s) + \omega_2(n, s) = \omega_1(s) + [\omega_{2A}(n, s) + \omega_{2B}(n, s)] \quad \text{Eq. 3.6}$$

where $\omega_2(n, s)$ is subsequent divided into $\omega_{2A}(n, s)$ and $\omega_{2B}(n, s)$. The primary warping depends only on the geometrical and material properties of the contour while the secondary warping is also function of the variable n (position in the wall thickness). Finally the complete warping function is expressed for open and closed cross-sections as follows [31]:

$$F(n, s) = \underbrace{\int_0^s r ds}_{\omega_1} - \underbrace{nq}_{\omega_{2A}} \quad \text{Eq. 3.7}$$

$$F(n, s) = \int_0^s \underbrace{\left(r - \frac{\oint r ds}{\mathcal{L} t G_{sz}} \right)}_{\omega_1} ds - \underbrace{nq}_{\omega_{2A}} - 2n \int_0^s \underbrace{\left[\frac{\oint ds}{t G_{sz} \mathcal{L}} - 1 \right]}_{\omega_{2B}} ds \quad Eq. 3.8$$

where $t(s)$ is the thickness and $G_{sz}(s)$ is the tangential shear stiffness which depends of the contour position s . \mathcal{L} is defined as:

$$\mathcal{L} = \oint \frac{ds}{t(s) G_{sz}(s)} \quad Eq. 3.9$$

For a multilayer composite laminate the tangential shear stiffness $G_{sz}(s)$ is taken as:

$$G_{sz}(s) = \frac{A_{66}(s)}{t(s)} \quad Eq. 3.10$$

where $A_{66}(s)$ is obtained once the ABD matrix is calculated [22-23] and represents the composite shear stiffness:

$$A_{66}(s) = \int \bar{Q}_{66}(s) dn \quad Eq. 3.11$$

and $\bar{Q}_{66}(s)$ is the plane-stress shear stiffness of a composite ply, in the global beam coordinate system [22-23]. Aguirre mention that for closed sections usually only $\omega_1(s)$ and $\omega_{2A}(n, s)$ are considered, as $\omega_{2B}(n, s)$ vanishes when both, the thickness and the tangential shear stiffness are constant along the contour. It is convenient to choose a contour origin and pole position which allow satisfying the condition:

$$\oint F(n, s) ds = 0 \quad Eq. 3.12$$

Eq. 3.12 implies that the warping displacement $w(n, s, z)_\omega$ is continuous along the cross section perimeter. To complete the warping function a constant C must be subtracted and it is defined as:

$$C = \frac{\oint F(n, s) ds}{\oint ds} \quad Eq. 3.13$$

3.1.2. Strain in TWB

Based on assumption 1, the full strain field is defined by:

$$\begin{aligned}\varepsilon_{zz} &= \frac{\partial w(s,z,n)}{\partial z} \\ \gamma_{sz} &= 2\varepsilon_{sz} = \frac{\partial w(s,z,n)}{\partial s} + \frac{\partial v(s,z,n)}{\partial z} \\ \gamma_{nz} &= 2\varepsilon_{nz} = \frac{\partial w(s,z,n)}{\partial n} + \frac{\partial u(s,z,n)}{\partial z}\end{aligned}\tag{Eq. 3.14}$$

Using Eq. 3.14 the full shell strain field is:

$$\begin{aligned}\varepsilon_{zz} &= W' + \psi_y'(x + n \sin \theta) + \psi_x'(y - n \cos \theta) + \psi_\omega'[F(n, s)] \\ \gamma_{sz} &= \gamma_{xz} \cos \theta + \gamma_{yz} \sin \theta + \gamma_\omega[r - n - F_t(s)] + \varphi'[F_t(s) + 2n] \\ \gamma_{nz} &= \gamma_{xz} \sin \theta - \gamma_{yz} \cos \theta - \gamma_\omega[q + F_2(s)]\end{aligned}\tag{Eq. 3.15}$$

The term $F(n, s)$ is the complete warping function as defined in the previous section Eq. 3.8. For convenience, the following terms are defined as they appear naturally on the mathematical formulation [31]:

$$\begin{aligned}F_t(s) &= \frac{\oint r_n(s) ds}{t(s)G_{sz}(s)\mathcal{L}} \\ F_2(s) &= 2 \int_0^s \left[\frac{\oint ds}{t(s)G_{sz}(s)\mathcal{L}} - 1 \right] ds\end{aligned}\tag{Eq. 3.16}$$

3.2. Constitutive equations

Wind turbine blades are typically manufactured using multi-layer laminated composites, each lamina having arbitrary thickness, material properties and fibre-orientation. The overall behaviour of a composite thin shell can be approximated by a plane-stress orthogonal constitutive law. Incorporating assumption 2 (non-deformability of the cross-

section) the constitutive law for the k -th lamina, expressed in the curvilinear CS (n,s,z) , can be expressed as in [16]:

$$\begin{Bmatrix} \sigma_{zz} \\ \sigma_{sz} \\ \sigma_{nz} \end{Bmatrix}^k = \begin{bmatrix} \bar{Q}_{11}^* & \bar{Q}_{16}^* & 0 \\ \bar{Q}_{16}^* & \bar{Q}_{66}^* & 0 \\ 0 & 0 & \bar{Q}_{55} \end{bmatrix}^k \begin{Bmatrix} \epsilon_{zz} \\ \gamma_{sz} \\ \gamma_{nz} \end{Bmatrix} \quad \text{Eq. 3.17}$$

It should be noticed that, due to a fully populated constitutive matrix, the material will exhibit some degree of extensional-bending-torsional coupling, and this behaviour is often induced for alleviating stresses due to excessive bending loads [24-26]. Thus, the developed model can also be used for optimizing the laminates' layup. The internal forces and moments acting on the blade are obtained by integrating these stresses over the contour of the airfoil's shell, as follows:

$$\begin{aligned} N_z &= \int_A \sigma_z dsdn \\ M_y &= \int_A \sigma_z (x + n \sin \theta) dsdn \\ M_x &= \int_A \sigma_z (y - n \cos \theta) dsdn \\ M_\omega &= \int_A \sigma_z [\omega_1(s) - nq - F_2(s)] dsdn \\ V_x &= \int_A (\sigma_{sz} \cos \theta + \sigma_{nz} \sin \theta) dsdn \\ V_y &= \int_A (\sigma_{sz} \sin \theta - \sigma_{nz} \cos \theta) dsdn \\ T &= \int_A \left[\sigma_{sz} \left(r - \frac{F_t(s)}{2} \right) - \sigma_{nz} \left[q + \frac{F_2(s)}{2} \right] \right] dsdn \\ M_t &= \int_A \left[\sigma_{sz} \left(n + \frac{F_t(s)}{2} \right) + \sigma_{nz} \frac{F_2(s)}{2} \right] dsdn \end{aligned} \quad \text{Eq. 3.18}$$

representing internal axial (N_z), bending (M_y , M_x), warping moment in the axial direction (M_ω , see Figure 3.6), shear (V_x , V_y), St Venant torsion (M_t) measured with respect to the pole axis and warping torsion acting tangential to the cross-section (T : see Figure 3.5). These loads are related to beam strains via (Eq. 3.15, Eq. 3.18) as follows:

$$\begin{pmatrix} N_z \\ M_y \\ M_x \\ M_\omega \\ M_T \\ V_x \\ V_y \\ T \end{pmatrix} = \begin{pmatrix} E_{11} & \cdot & \cdot & \cdot & \cdot & \cdot & \cdot & E_{18} \\ \cdot & \cdot & \cdot & \cdot & \cdot & \cdot & \cdot & \cdot \\ \cdot & \cdot & \cdot & \cdot & \cdot & \cdot & \cdot & \cdot \\ \cdot & \cdot & \cdot & \cdot & \cdot & \cdot & \cdot & \cdot \\ \cdot & \cdot & \cdot & \cdot & \cdot & \cdot & \cdot & \cdot \\ \cdot & \cdot & \cdot & \cdot & \cdot & \cdot & \cdot & \cdot \\ \cdot & \cdot & \cdot & \cdot & \cdot & \cdot & \cdot & \cdot \\ \cdot & \cdot & \cdot & \cdot & \cdot & \cdot & \cdot & E_{88} \end{pmatrix} \begin{pmatrix} \epsilon_z^0 \\ \kappa_y \\ \kappa_x \\ \kappa_\omega \\ \kappa_{sz} \\ \gamma_{xz}^0 \\ \gamma_{yz}^0 \\ \gamma_\omega^0 \end{pmatrix} \quad \text{Eq. 3.19}$$

where:

$$\epsilon_z^0 = W'; \kappa_y = \psi_x'; \kappa_x = \psi_y' \text{ and } \kappa_{sz} = \varphi' - \psi_\omega \quad \text{Eq. 3.20}$$

The matrix $[E_{ij}]$ represents the stiffness of a given cross-section. This matrix is the TWB counterpart of the well-known ABD matrix [22-23] representing the extensional (A), flexural (B) and coupled extensional-flexural (D) stiffness of a material cross-section. For more detailed description on $[E_{ij}]$ determination refer to Appendix A. Since coefficients $[E_{ij}]$ contain detailed information of the stiffness of any material point in the shell (including angular and thickness location), full deformation and stress fields could be recovered for post-processing, as required by advanced failure criteria for composites.

3.3. Finite element model

The strain energy in the beam is equal to:

$$u = \frac{1}{2} \int_v \sigma_{zz} \epsilon_{zz} + \sigma_{sz} \gamma_{sz} + \sigma_{nz} \gamma_{nz} \quad \text{Eq. 3.21}$$

Substituting Eq. 3.15 into Eq. 3.21 the strain energy yield:

$$\begin{aligned}
u = \frac{1}{2} \int_V \sigma_{zz} [W' + \psi_y'(x + n \sin \theta) + \psi_x'(y - n \cos \theta) + \psi_\omega'(F(n, s))] \\
+ \sigma_{sz} [\gamma_{xz} \cos \theta + \gamma_{yz} \sin \theta + \gamma_\omega [r - n - F_t(s)] + \varphi' [F_t(s) + 2n]] \\
+ \sigma_{nz} [\gamma_{xz} \sin \theta - \gamma_{yz} \cos \theta - \gamma_\omega (q + F_2(s))]
\end{aligned} \quad \text{Eq. 3.22}$$

The loads defined in Eq. 3.18 appear in Eq. 3.22 and can be reduced to:

$$u = \frac{1}{2} \int_0^l N_z W' + M_x \psi_y' + M_y \psi_x' + M_\omega \psi_\omega' + V_x \gamma_{xz} + V_y \gamma_{yz} + T \gamma_\omega + M_t \kappa_{sz} \quad \text{Eq. 3.23}$$

Substituting the loads from Eq. 3.19 in Eq. 3.23, the strain energy is now expressed as a function of the displacements and matrix $[E]$. Using the principle that the variation of the potential energy is zero (the sum of the strain energy and the work done by an external loads) in [15,14,27] the weak form of the equations are obtained and are solved assuming one dimensional displacement-based finite element method formulation. The generalized displacements are expressed as a linear combination of the 1D Lagrange interpolation function Y_j associated with nodal j and the nodal values:

$$\begin{aligned}
W &= \sum_{j=1}^2 W_j Y_j & V &= \sum_{j=1}^2 V_j Y_j & \psi_y &= \sum_{j=1}^2 \psi_{y_j} Y_j \\
U &= \sum_{j=1}^2 U_j Y_j & \varphi &= \sum_{j=1}^2 \varphi_j Y_j & \psi_x &= \sum_{j=1}^2 \psi_{x_j} Y_j \\
& & & & \psi_\omega &= \sum_{j=1}^2 \psi_{\omega_j} Y_j
\end{aligned} \quad \text{Eq. 3.24}$$

and:

$$\begin{aligned}
Y_1 &= 1 - \frac{z_e}{l_e} \\
Y_2 &= \frac{z_e}{l_e}
\end{aligned} \quad \text{Eq. 3.25}$$

Where z_e is equal to 0 in node number 1 and equal to l_e (element length) in node number 2. The discrete equations of motion for a generic beam element can be expressed as follows:

$$[M]\{\ddot{u}\} + [C]\{\dot{u}\} + [K]\{u\} = \{f\} \quad \text{Eq. 3.26}$$

where $[M]$, $[K]$ and $[C]$ are the element's mass and linear stiffness matrices as defined in [15,14,27], $[C]$ is a hysteretic damping matrix, $\{f\}$ is a vector of nodal forces, and $\{u\}, \{\dot{u}\}, \{\ddot{u}\}$ are nodal displacement, velocities and accelerations, respectively. These matrices and vectors have the following structure:

$$[K] = \begin{bmatrix} K_{1,1} & \cdots & K_{1,14} \\ \vdots & \ddots & \vdots \\ \text{sym} & \cdots & K_{14,14} \end{bmatrix}_{14 \times 14} \quad [M] = \begin{bmatrix} M_{11} & \cdots & M_{1,14} \\ \vdots & \ddots & \vdots \\ \text{sym} & \cdots & M_{14,14} \end{bmatrix}_{14 \times 14}$$

$$\{u\} = \begin{Bmatrix} W_j \\ U_j \\ V_j \\ \varphi_j \\ \psi_{yj} \\ \psi_{xj} \\ \psi_{\omega j} \end{Bmatrix}_{14 \times 1} \quad \{f\} = \begin{Bmatrix} f_{axial} \\ f_{flap-wise} \\ f_{edge-wise} \\ f_{torsional} \\ M_y \\ M_x \\ M_\omega \end{Bmatrix}_{14 \times 1} \quad \text{Eq. 3.27}$$

$[C]$ is the damping matrix, usually determined experimentally for a given damping model. In this work, Rayleigh proportional damping was applied in the form of $[C] = \alpha[K]$, where $\alpha=0.008$ is a hysteretic damping factor recommended for glass fibre [28]. The vector $\{f\}$ comprises all external loads applied on the blade: $f_{edge-wise}$ and $f_{flap-wise}$ are caused by the aerodynamic forces on the blade, f_{axial} is due to gravity and centrifugal forces, and $f_{torsional}$, M_y , M_x and M_ω arise from the pressure distribution on the blade.

Figure 3.8 shows a generic TWB element, illustrating the 7 degrees of freedom (DOF) per node ($W, U, V, \varphi, \psi_y, \psi_x, \psi_\omega$); since each element is composed of two nodes, the element matrices will have a size of 14×14 . The 7th DOF and its definition in the boundary conditions denote two models of twist deformation: free warping ($M_\omega = 0$) and warping restrained ($\psi_\omega = 0$).

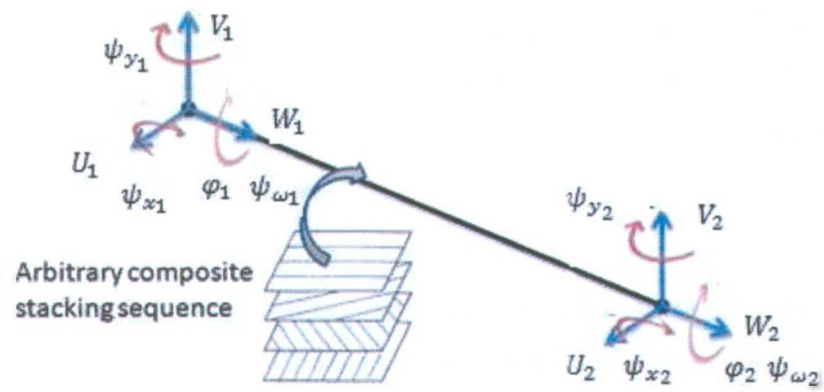


Figure 3.8: Generic 2-node TWB element with 14 DOF

References

- 1 Hau, E. Wind Turbines: Fundamentals, Technologies, Application, Economics, 2nd Ed., Springer-Verlag, Berlin. 2006
- 2 Laird D, Montoya F, Malcolm D. Finite Element Modeling of Wind Turbine Blades, ASME/AIAA Wind Energy Symposium. Reno, NV, 2005, pp. 9-17.
- 3 Bonnet P, Dutton G. Parametric Modeling Of Large Wind Turbine Blades. Abaqus UK Regional User Meeting. Didcot, Oxon. Energy Research Unit – STFC Rutherford Appleton Laboratory
- 4 Hodges DH. Nonlinear Composite Beam Theory. AIAA: Reston, VA, 2006.
- 5 Hodges D.H, Yu W. A rigorous, engineer-friendly approach for modeling realistic, composite rotor blades. Wind Energy 2006; 10: 179-193
- 6 Volovoi V, Hodges D.H, Cesnik C.E.S, Popescu B. Assesment of beam modelling methods for rotor blade applications. Mathematical and Computer Modelling 2001; 33: 1099-1112
- 7 Berdichevsky, V. L., Variational-asymptotic method of constructing a theory of shells, Journal of Applied Mathematics and Mechanics (English translation of Prikladnaya Matematika i Mekhanika), vol. 43, no. 4, pp. 664–687, 1979.
- 8 Yu W, Volovoi V, Hodges D.H, Hong, X. Validation of the Variational Asymptotic Beam Sectional Analysis. AIAA Journal 2002; 40 (10)
- 9 Li L. Structural design of composite rotor blades with consideration of manufacturability, durability and manufacturing uncertainties. Doctoral Thesis in School of Aerospace Engineering. Georgia Institute of Technology. August 2008
- 10 Librescu L, Song O. Thin-walled Composite Beams: Theory and Application. Springer, 2006
- 11 Qin Z, Librescu L. On a shear-deformable theory of anisotropic thin-walled beams: further contribution and validations. Composite Structures 56 (2002) 345–358
- 12 Oh S, Song O, Librescu L. Effects of pretwist and presetting on coupled bending vibrations of rotating thin-walled composite beams. International Journal of Solids and Structures 40 (2003) 1203–1224
- 13 Vo P, Lee J. Geometrically nonlinear analysis of thin-walled composite box beams. Computers and Structures 87 (2009) 236–245

- 14 Phuong T, Lee J. Flexural–torsional behavior of thin walled composite box beams using shear-deformable beam theory. *Engineering Structures* 30 (2008) 1958–1968
- 15 Phuong T, Lee J. Free vibration of thin-walled composite box beams. *Composite Structures* 84 (2008) 11-20
- 16 Vo TH, Lee J. Flexural torsional behavior of thin walled closed-section composite box beams. *Engineering Structures* 2007; 29: 1774-1782
- 17 Piovani M, Cortinez V. Mechanics of shear deformable thin-walled beams made of composite materials. *Thin-Walled Structures* 45 (2007) 37–62
- 18 Cook RD. *Advanced mechanics of materials*. New York. Macmillan Publishing Company. 1998
- 19 Oden, J. T. and Ripperger, E. A. (1981) *Mechanics of Elastic Structures*, Second Edition, Hemisphere Publication Corp., Washington.
- 20 Ketter, RL. *Structural analysis and design*. New York: McGraw-Hill, 1979.
- 21 N. Silvestre, D. Camotim. On the mechanics of distortion in thin-walled open sections. *Thin-Walled Structures* 48 (2010) 469–481.
- 22 Jones RM. *Mechanics of composite materials*. New York: Hemisphere Publishing Corp. 1975.
- 23 Tuttle M. (2004). *Structural Analysis of Polymeric Composite Materials*. New York: Marcel Dekker.
- 24 Mason, K. Anisotropic Wind Blade Design Expected to Reduce Wind Energy Costs. *High Performance Composites*. November 2004.
- 25 Chandra R, Chopra I. Structural response of composite beams and blades with elastic couplings. *Composites Engineering* 2 (1992) 347-374.
- 26 De Goeij W.C, van Tooren M.J.L, Beukers A. Implementation of bending-torsion coupling in the design of a wind-turbine rotor-blade. *Applied Energy* 63 (1999) 191-207.
- 27 Vo P, Lee J, Ahn N. On sixfold coupled vibrations of thin-walled composite box beams. *Composite Structures* 89 (2009) 524–535
- 28 Burton T, Sharpe D, Jenkins N, Bossanyi E. *Wind Energy Handbook*. Wiley 2001

29 D. Cárdenas, H. Elizalde, P. Marzocca, O. Probst. Numerical validation of a finite element thin-walled beam model of a composite wind turbine blade Article first published online: 18 MAR 2011 DOI: 10.1002/we.462 Wind Energy 2011

30 FP Costa. On Timoshenko's Beams Coefficient of Sensibility to Shear Effect. Tend. Mat. Apl. Comput., 9, No. 3 (2008): 447-457.

31 JJ Aguirre. Numerical validation of a finite element thin-walled beam model of a composite wind turbine blade incorporating transverse shear and full secondary warping. Master Thesis of ITESM Campus Monterrey. December 2010.

Chapter 4.

Static and dynamic TWB validation

Chapter Summary

This chapter presents an extensive and realistic numerical simulation of the TWB model described previously using a generic wind turbine rotor blade. A 9.2m rotor blade, previously reported in specialized literature, was chosen to validate the static and dynamic behaviour predicted by a TWB model against an industry-standard 3D shell model. It is concluded that, despite its simplicity, a TWB FE model is sufficiently accurate to serve as a design tool for the recursive analyses required during design and optimization stages of wind turbines using only readily available computational tools.

This chapter presents a numerical validation of a thin-wall beam (TWB) finite element (FE) model of a realistic wind turbine rotor blade. While the Librescu's theory has been successfully applied to a host of problems [1-7], to our knowledge it has not yet been used in a complex application like twist-tapered composite wind turbine blade. A representative 9.2m rotor blade by TPI Composites Inc., typically used in wind turbines rated at about 100kW, was chosen for the purpose of numerical validation. It was designed around a number of airfoils of variable chord, with a material layup conformed of glass fibre composites, balsa wood and gel coating. The thin shell is reinforced with an inner central web and a pre-twist function is applied along the blade's span. Although this blade was discussed comprehensively in [8], there was some missing information regarding geometrical and material data of the blade's root-end (playing a significant role in the blade's overall stiffness), which were here assumed for the purpose of constructing dedicated FE models. For this reason, numerical results obtained in this research were not

directly compared to those reported in [8], but rather between the models generated during the course of this investigation using the TWB and FE.

Two FE models of the sample rotor blade were built: the first was based on ANSYS® 3D-shell99 elements conformed by 55,356 DOF. Because of its large size, this model was able to reproduce the blade's geometry and laminate layup very accurately. The second model was a MATLAB® implementation of the TWB element here presented, conformed by 217 DOF. Both models shared the same input database for geometry, airfoil type, material properties and layup, etc., with some assumptions respect to the data provided in [8]. In order to compare their dynamic behaviour, those were numerically solved (in their respective software tool) for the first few natural frequencies and mode shapes, tip deflections for four linear static load cases and frequency response functions (FRFs) for the tip flap-wise and edge-wise DOF. Some results were also compared with those published in [8] for the same blade, which were obtained via an ANSYS® model similar to the one generated here. In addition, in the following a brief discussion is provided regarding the gain in accuracy yielded by the choice of warping-restrained (WR) or free-warping (FW) boundary conditions applied to the TWB FE model.

4.1. Definition of the geometry

The wind turbine blade used here for numerical validation is based on the prototype NPS-100 from Sandia National Laboratories (SNL), as published in [8]. According to this report, the NPS-100 is a derivative of the ERS-100, a 9.2 meter all-fibreglass blade originally developed by Sandia National Laboratory (SNL) and TPI Composites Inc., intended for the 100 kW retrofit market in California. Although the SNL report is comprehensive in describing most features of the NPS-100, there is some missing information regarding geometry and material layup (mostly pertaining to the blade's root) which had to be assumed to construct numerical models. Given that the blade's root-end has a significant impact on its overall stiffness, clearly these uncertainties will have some effect on the static and dynamic response of the blade. For this reason, error measures were not calculated here with respect to published results in [8], but rather between the numerical models generated during the course of this research.

4.1.1. External geometry

For geometric modeling purposes, the external geometry of the blade was divided in spanwise direction into three clearly defined regions, as shown in Figure 4.1:

1) the root, a cylindrical-shaped portion located between $x=0\text{m}$ (the root end) and $x=0.6\text{m}$ with a constant external diameter (or chord) given by $C_{\text{Root}}=0.325\text{m}$

2) the transitional region, starting with a cylinder at $x=0.6\text{m}$ and morphing via a non-linear chord variation (given by polynomial C_{Trans} , see also Appendix B) up to airfoil S821 (Figure 4.2) at $x=1.8\text{m}$, and

3) the main body, which uses the same airfoil S821 and linear chord variation (polynomial C_{Body}) through the span. The external chord (C) and twist (β) distributions along the blade are defined in Figure 4.1 and Figure 4.3, respectively. In order to define different laminates over the blade's top and bottom surfaces, each airfoil was divided chordwise into five segments, numbered I to V in Figure 4.2, which divisions were placed at chord positions of 0%, 5%, 30%, 40%, 60% and 100%. An important remark is that this and other divisions of the blade's geometry (regions, sections, segments, etc.) are meant only for organizing geometric and material information purpose, and are unrelated to finite elements' size.

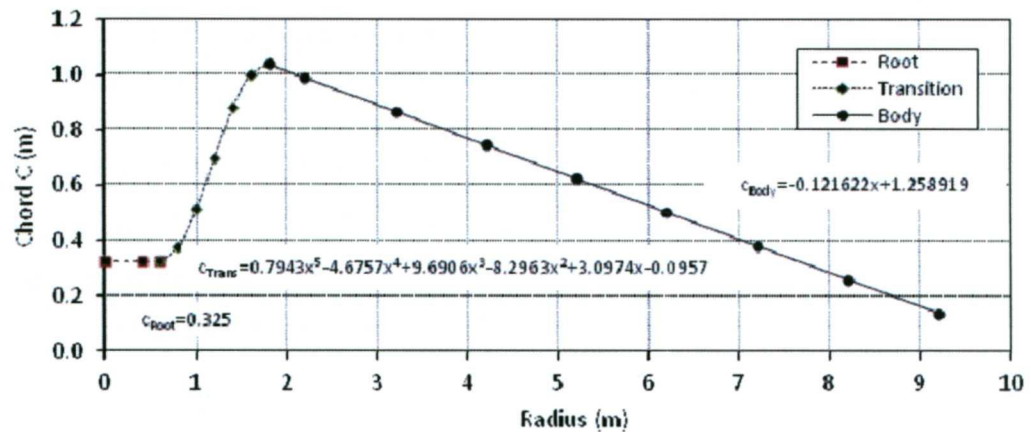


Figure 4.1: External chord (C) variation along blade's length [8]. See Appendix B for detailed information of cross-sections belonging to the transitional region.

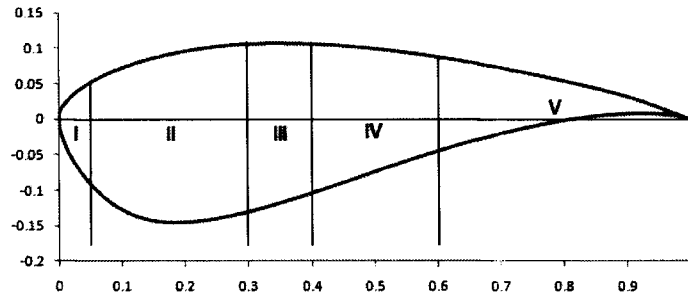


Figure 4.2: Airfoil S821 divided in segments I through V. Divisions occur at 0%, 5%, 30%, 40%, 60% and 100% of the chord's length.

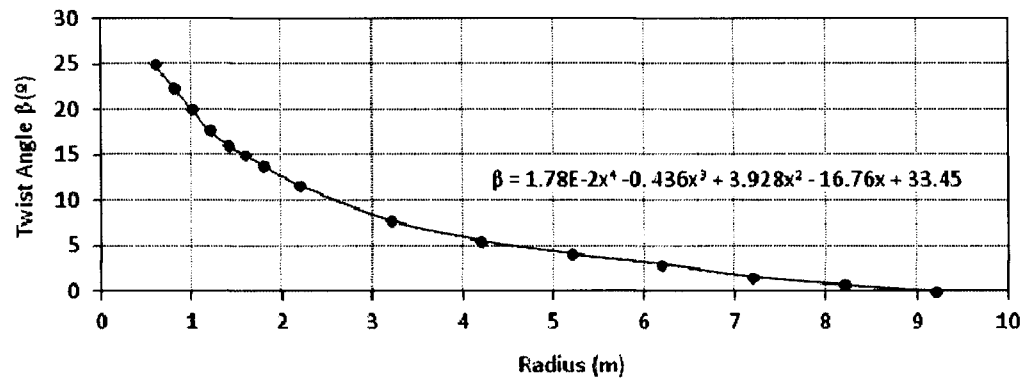


Figure 4.3: Twist angle (β) distribution along blade's length [8].

The blade cross-sections were arranged via a reference line intersecting them, as shown in Figure 4.4: the circular sections corresponding to region 1 (the root) are intersected at their centers, while the airfoils of region 3 (the main body) are intersected at 35% of their correspondent chords. The transitional airfoils of region 2, which individual geometries are detailed in Appendix B, are intersected at a chord position corresponding to the midpoint of segment III (as defined in Figure 4.2). Finally, the twist distribution is imposed by rotating the airfoils around the reference line according to Figure 4.3.

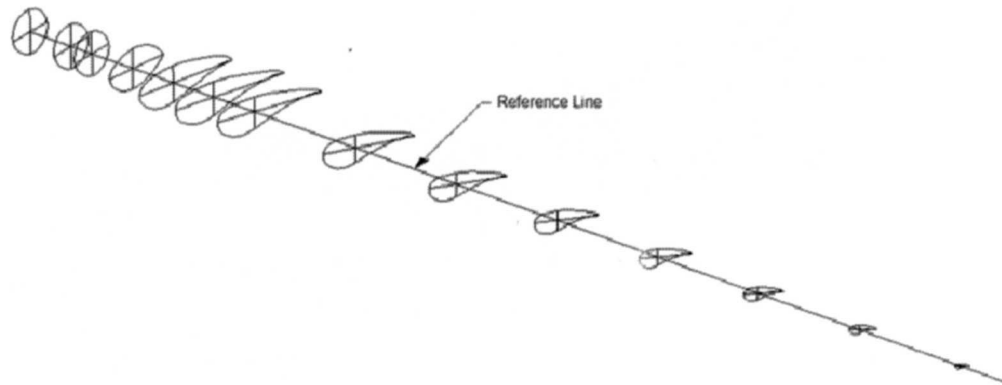


Figure 4.4: Airfoil alignment over the reference line.

4.1.2. Internal geometry

Internal to the blade, a shear web (also called “main spar”) runs along most of the blade’s length, joined to the internal surfaces of the top and bottom shells via adhesive, and whose main purpose is to provide bending stiffness. As illustrated in Figure 4.1, the shear web starts at a radius position of $R=1\text{m}$, running along the reference line shown in Figure 4.4 up to $R=8.2\text{m}$. Its evolving cross-section can be defined via planes given by the airfoils themselves, for which a local Cartesian CS is defined with origin at its intersection with the reference line, that is, at the mid-point of segment III of each airfoil. The horizontal axis of this CS is given by the chord, while the vertical axis is perpendicular to it. For each airfoil, a shear web’s cross-section is defined as a rectangle centred at the origin, with height bounded by the internal surfaces of the top and bottom shells and width of 10.64mm , the latter as specified by Layup Code 16 in Appendix C. Figure 4.5 shows a cut view of the blade at a radius position of $R=3.2\text{m}$, illustrating the airfoil’s cross-section and the internal shear web. Colours identify different material layups (here called Layup Code), to be described in the next section.

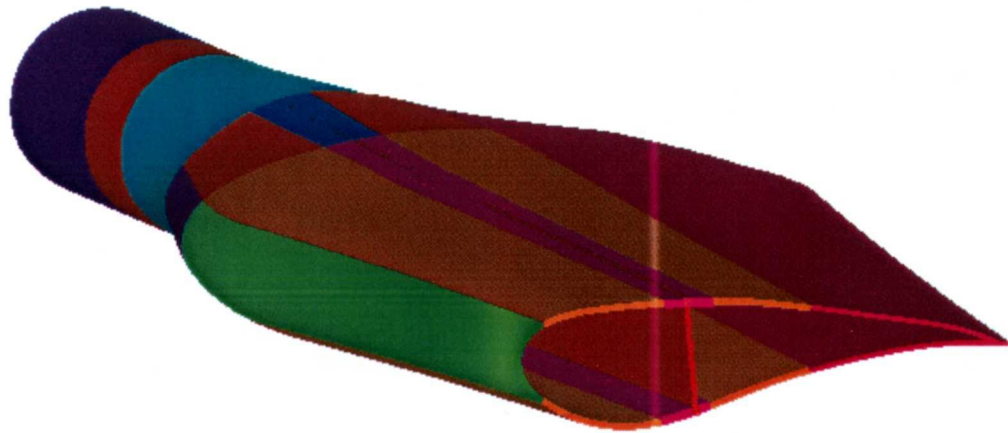


Figure 4.5: Cut view of the blade at a radius position of $R=3.2\text{m}$, showing the airfoil's cross-section and internal shear web. Colours identify the Layup Code.

4.2. Materials Layup

The TWB formulation here presented allows material layup to be specified quite arbitrarily along the blade's radius as well as top/bottom skins (balanced/unbalanced and symmetric/anti-symmetric laminates), only requiring splitting the cross-section's contour in pre-defined segments of uniform layup (as shown in Figure 4.2), which are assumed to remain uniform throughout a beam element. Therefore, the so-called circumferentially asymmetric stiffness (CAS or symmetric) and circumferentially uniform stiffness (CUS or anti-symmetric) [9-10] configurations can be incorporated in the model, allowing a full range of coupled extensional, bending and/or shear structural behaviour.

The materials employed for manufacturing the blade under study are listed in Table 4.1 and classified according to a *Material Code* (labeled "A" to "E"), also showing main elastic properties of each. For material modeling purposes, the blade geometry was divided spanwise into 13 sections, each of variable length (as represented in Figure 4.6); chordwise, as mentioned above, each airfoil was divided into 5 segments (I to V, illustrated in Figure 4.2). Based on these divisions, Table 4.2 assigns a numerical *Layup Code* to different sections and segments of the blade, while the same information is projected, via colours, onto the blade's geometry in Figure 4.6. The *Layup Code*, fully

described in Appendix C, represents a specific laminated composite which contains, for each individual lamina, a *Material Code*, fiber direction and thickness.

Table 4.1: *Material Code* and in-plane elastic properties [8]

Material Code	Material Name	Density Kg/m3	E ₁₁ GPa	E ₂₂ GPa	v ₁₂	G ₁₂ GPa
A	C520 (textile glass fibre)	1874	48.2	11.7	0.30	6.48
B	C260 (textile glass fibre)	1874	43	8.9	0.27	4.5
C	¾ mat (random glass fibre)	1670	7.58	7.58	0.30	6.48
D	Gel coat	1230	3.44	3.44	0.30	1.32
E	Balsa wood	144	2.07	-	0.22	-

Table 4.2: *Layup Code* mapping (detailed in Appendix C). *Layup Code 16*, not included in this table, represents the internal shear-web's layup.

		Section												
		1	2	3	4	5	6	7	8	9	10	11	12	13
Chord Segment	I	1	2	3	4	8	8	8	8	8	8	8	8	8
	II	1	2	3	5	9	9	9	11	11	11	11	13	15
	III	1	2	3	6	10	10	10	12	12	12	12	14	15
	IV	1	2	3	5	9	9	9	11	11	11	11	13	15
	V	1	2	3	7	7	7	7	7	7	7	7	7	7

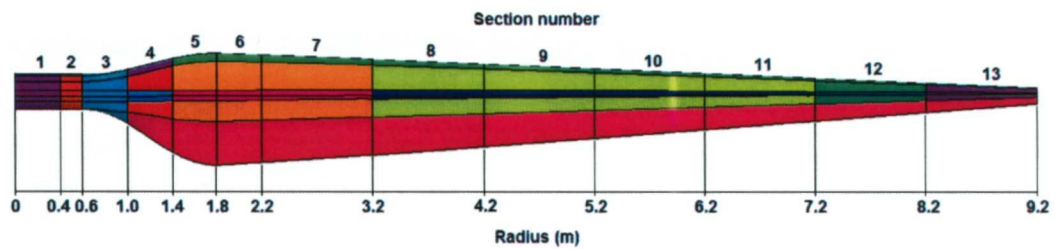


Figure 4.6: The blade section numbering and positions. Colours represent the *Layup Code*, fully detailed in Appendix C. *Layup Code 16*, not included in this Figure, represents the internal shear-web's layup.

The material layup for the blade's internal shear web is different from those represented in Table 4.2 and Figure 4.6. The shear web is mainly constructed from Balsa Wood (Material Code "E" in Table 4.1), and glass fiber (Material Codes "B" and "C") joined to the internal surfaces of the top and bottom shells via adhesive. The specific layup corresponding to the width of the shear web is specified by the *Layup Code 16*, which is fully described in Appendix C.

4.3. Results

The aforementioned geometric and material database was used to construct two separate FE models with the purpose of evaluating the static and dynamic performance of the introduced TWB formulation against proved methodologies.

Model 1 was based on ANSYS® 3D-Shell99 quadratic 8-node elements, widely used in the industry for design purposes [11-12] thus taken here as benchmark. This type of element allows defining an arbitrary number of layers in a single unit, each layer having specific material properties, fibre orientation, and thickness. Such properties are defined in a local (i.e. element based) coordinate system, therefore great care must be exercised to ensure that all elements belonging to the same laminate (i.e. Layup Code) share the same orientation, making the modeling process a time-consuming and error-prone task. A further difficulty is that complex geometric features or/and laminate composition often dictate a relatively small element size, since compatibility conditions require that an element must have a unique material composition, and this issue makes a convergence analysis a very cumbersome task. Model 1, shown in

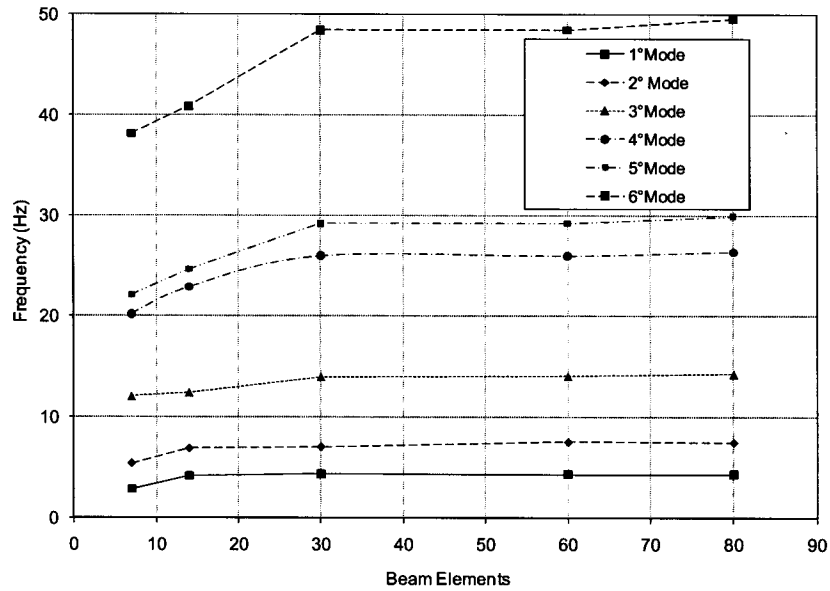
Figure 4.7, was discretized in 3352 elements and 9,926 nodes, equivalent to 55,356 DOF, with all translational and rotational DOF at the root-end completely fixed. The pre-processing tasks for setting-up this model (CAD, meshing, input data, analysis set-up, etc.) took about 80 man-hours, carried out by skilled personnel, and then solved in ANSYS®.



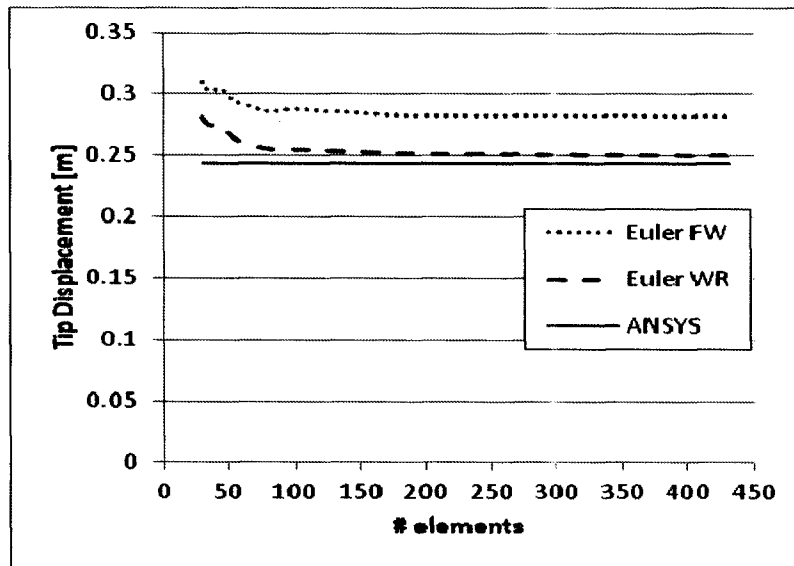
Figure 4.7: Model 1 built in ANSYS®

Model 2 was based on a MATLAB® implementation of the TWB theory presented above. A significant advantage of this formulation is that, as opposed to Model 1, geometric and material complexities of a given cross-section do not exert influence on element size, which impacts directly on computational economy. This happens because those features are tackled “off-line” during the computation of matrix $[E]$ (see Appendix A), which is calculated once for each cross-section of the structure and then stored for future analyses of smaller/larger models. A convergence analysis was performed to obtain the minimum number of TWB elements for an accurate representation of the low-frequency behaviour of the blade. Figure 4.8 a shows the variation of the first six natural frequencies of Model 2 (with its root-end node fully fixed) for increasing number of elements, observing an asymptotic behaviour at about 30 elements, equivalent to 31 nodes and 217 DOF. These 30 elements were distributed along the blade’s radius as follows: 3 for the Root region, 6 for the Transitional region and 21 for the Body region (see Figure 4.1). Due to material anisotropy and complex layup, significant extensional-bending-torsional coupling was expected even for simple load cases, thus some higher-modes (mainly torsional) could impact low frequency behaviour. To this end, a further convergence analysis for Load Case 1, later described in detail, was conducted on Model 2 (see Figure 4.8b), exhibiting the need of up to 150 elements to achieve an error lower than 2%. Also, it is observed that the choice of FW (Free Warping) or WR (Warping Restrained) has some influence on the accuracy, also discussed later. The pre-processing tasks for setting up Model 2 took about 10 man-hours, carried out by the same personnel who built Model 1, and then solved by standard MATLAB routines.

For the sake of completeness, some results were also compared with those reported in literature [8] for an FE model of the same blade, labelled here as “Model 3”. This model shares close similarities with Model 1 in terms of size (3,770 elements), DOF (66,936) and element topology (ANSYS® 3D-Shell99). In fact, the major differences between Models 1 and 3 are due to some omissions in [8] regarding the geometry and material layup of the blade’s root-end, which had to be assumed for constructing Models 1 and 2.



(a) Convergence analysis of Model 2 (TWB) for the first six modes



(b) Convergence analysis of Model 2 (TWB) for Load Case 1

Figure 4.8

Table 4.3 summarizes the both the static and the dynamic results of all three models, where error measures are given for comparisons between Models 1 and 2 only, and results not available for comparison are marked as "--". The first 6 natural frequencies of Models 1 and 2 exhibit minimum and maximum deviations of 0.73% and 20.05% for the third and sixth mode, respectively, while the departure in the fundamental frequency is 1.98%. Due to the extensional-bending-torsional coupling, none of the correspondent mode shapes are fully flap-, edge- or twist-wise, rather exhibiting a mixed behaviour. This effect is quantified for each mode, where maximum displacements are normalized to unity. For example, Model 2's first mode (4.81Hz) is seen to be flap-wise dominant (1), with significant edge-wise coupling (0.205) and negligible coupling in twist (≈ 0). As seen in Table 3, the coupling exhibited by Model 1 is reasonably reproduced by Model 2 for all modes. Although this coupling is not reported for Model 3, it can be verified that the first five frequencies of the latter are comparable to those of Models 1 and 2.

An interesting observation during the analyses was that edgewise-dominant mode shapes (i.e. Modes 2 and 4) exhibited consistently higher frequencies in Model 2 as compared to Model 1. This is possibly due to the Euler-Bernoulli assumption in Model 2,

which neglects shear energy and therefore behaves rather rigidly for relatively thick beams. As seen in Figure 4.1, the blade has a maximum edgewise thickness of about 1m at the end of its transitional region, which in view of its 9.2m total length, slightly violates the minimum length/width ratio recommended for an Euler-Bernoulli model, typically taken as 10 [1]. This can be easily corrected by implementing a C^0 (i.e. Timoshenko) formulation in the TWB element, thus allowing shear energy to occur.

Table 4.3: Results for Modal and Linear Static analyses. Error measures relate Models 1 and 2 only.

	Model 1				Model 2				Model 3 [29]				
	(ANSYS® Shell99)				(TWB)								
# elements	3352				150				3770				
# nodes	9926				151				11156				
# DOF	55356				1057				66936				
	Mode Shape				Mode Shape								
Mode	Flap	Edge	Twist	Freq.	Flap	Edge	Twist	Freq.	Freq.	Error			
				(Hz)				(Hz)			(Hz)		
1	1	0.254	0.001	4.716	1	0.205	≈0	4.81	4.52	1.98			
2	0.33	1	0.002	6.667	0.41	1	≈0	7.42	7.13	11.30			
3	1	0.157	0.002	14.109	1	0.18	≈0	14.21	12.27	0.73			
4	0.46	1	0.002	24.801	0.47	1	≈0	26.39	22.43	6.42			
5	1	0.38	0.005	28.008	1	0.31	0.000	30.62	24.58	9.32			
6	1	0.119	0.026	42.62	1	0.13	0.004	51.16	--	20.05			
	Linear Static Load Cases				Linear Static Load Cases								
Load Case 1	243	26	2.4		252.63	26.24	0.24			3.96			
	mm	mm	°		mm	mm	°						
Load Case 2	26	95	1.73		36.91	86.34	0.33				mm	mm	°
	mm	mm	°		mm	mm	°						
Load Case 3	9	1	15.51	1.92	-0.11	11.29	mm	mm	°	27.21			
	mm	mm	°	mm	mm	°							
Load Case 4	130			128.78	16.12	0.01	mm	mm	°	187			
	mm	--	--	mm	mm	°	mm			0.94			

Based on load cases suggested in [8], three linear static load cases were analysed for Models 1 and 2, using the following load conditions: 1) 2,230N flapwise tip load, 2)

2,230N edgewise tip load, and 3) 1,000Nm torque applied at the tip. As expected, each of these loads produced coupled displacements in the three directions, with a dominant response according to the direction of the applied load. Tip displacements for these load cases are also summarized in Table 4.3, where the error is measured by the deviation between dominant displacements for each load case, and comparative displacement curves are plotted in Figure 4.9 and Figure 4.10. A fourth load case, analysed comprehensively in [8] for Model 3, was also performed in Models 1 and 2, corresponding to four point loads of 0.25 kpi, each applied flapwise at 3, 4.5, 6.5 and 8 meters along the blade's radius. Flapwise tip displacements for this load case are included in Table 4.3 (labeled "Load Case 4"), while Figure 4.11 plots comparative displacement curves.

The good match exhibited by load cases 1, 2 and 4 (3.96%, 9.12% and 0.94% error, respectively) is encouraging, since they are representative of main wind load on turbine blades. This can be confirmed with a glance to Figure 4.9 and Figure 4.11, where it can be seen that results are accurate not only for tip displacements, but for the whole blade's length. The higher deviation observed for Model 3 in Figure 4.11 was expected, in view of the modeling uncertainties already mentioned. On the other hand, the large error reported for load case 3 (27.21%) should be of no concern, since it refers to the angular displacement of the tip element, which has a negligible contribution to the total aerodynamic load. In fact, Figure 4.10 shows that Model 2, when subject to the warping restrained (WR) boundary condition, yields a deflection curve which is very close to that of Model 1 all along the blade's body, yielding a least-squares error of 6.35%.

Finally, frequency response functions (FRF) of Models 1 and 2 were obtained for a frequency range around the first 5 modes and using a hysteretic damping of 0.008 [13]. Figure 4.12 and Figure 4.13 show FRFs' magnitudes corresponding to the flapwise and edgewise tip-DOF, respectively, both for a flapwise tip-DOF excitation. Consistent with observations made for modal data and static load cases, it is seen that the first mode is predicted with a somewhat higher accuracy under the WR boundary condition, while a better prediction is obtained for the higher modes using free warping (FW). Aside from some differences regarding the exact locations of the resonance frequencies, a striking feature in both plots is the very good agreement of the damping behaviour for all visible modes, as noticed by the similar width of correspondent resonances and anti-resonances.

Regarding peak magnitudes, modes 2 and 3 are really in good agreement, as the apparent large discrepancies in the edgewise FRF are due to the logarithmic scale used, and the true differences in peak magnitudes are only 0.0029 and 0.004dB, respectively.

When assessing the aforementioned results, especially error measures, it must be kept in mind that a huge difference exists in the number of equations solved for Model 1 (55,356) and Model 2 (217). Given that each model was solved in its native software (ANSYS® and MATLAB®, respectively), comparisons of computation time have to be done with care. However, for practical purposes, the computational economy represented by Model 2 is substantial. Additional benefits in computational economy arise for the TWB model if geometric/material nonlinearities are included, which can be done straightforwardly in this model.

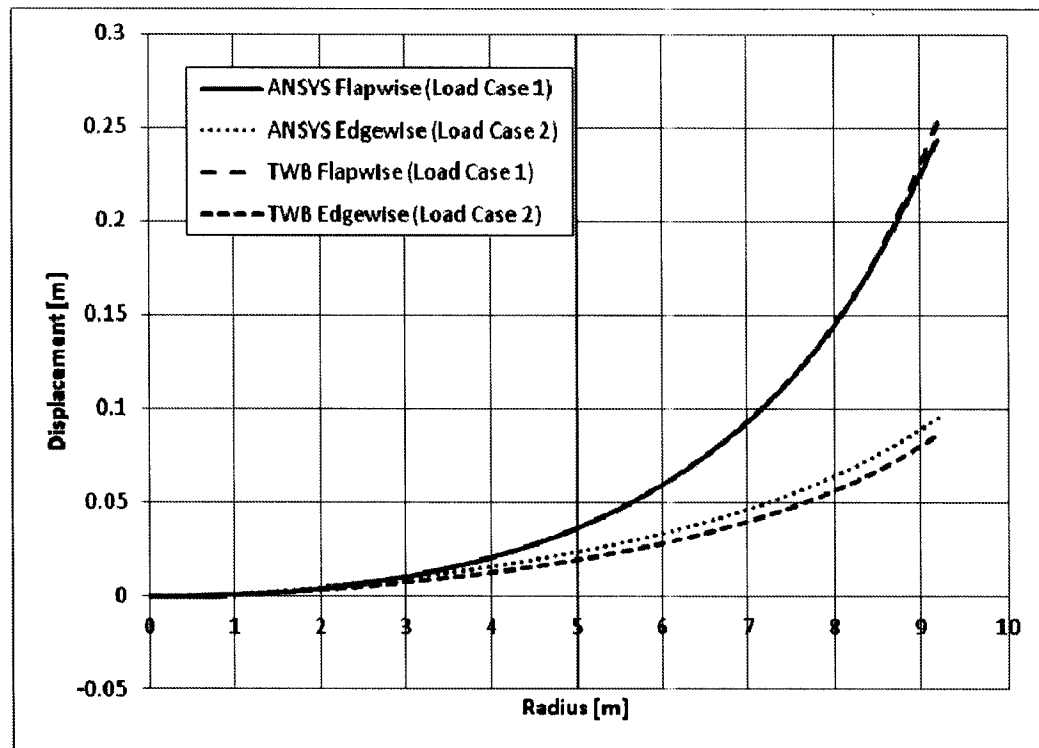


Figure 4.9: Displacement curves for Load Cases 1 and 2

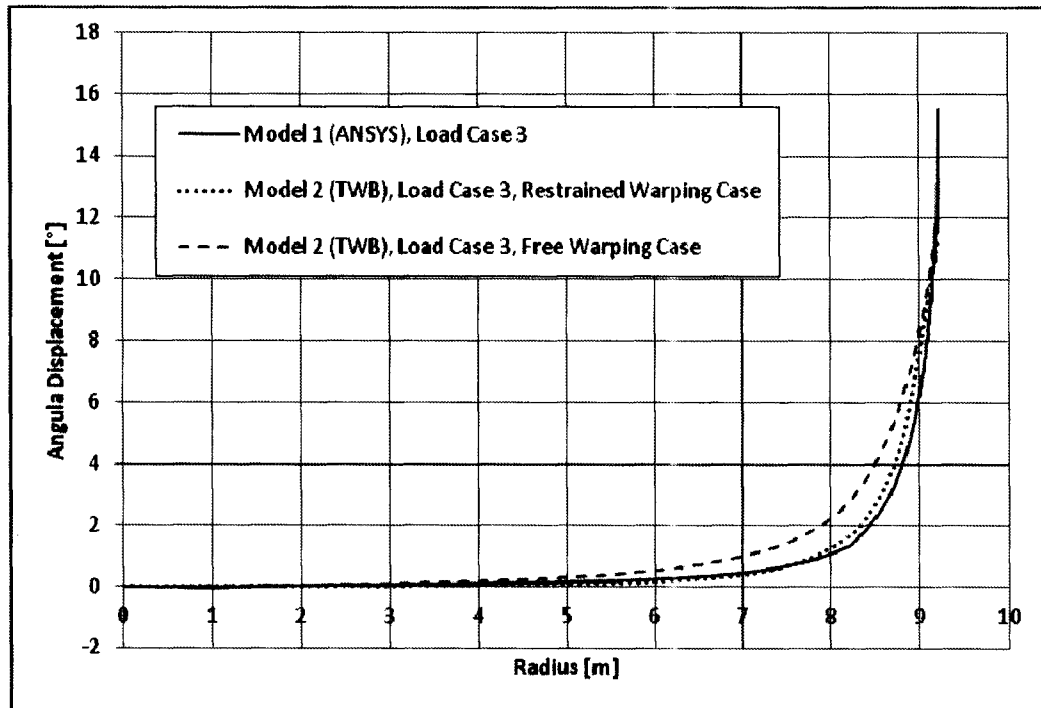


Figure 4.10: Angular displacement curves for Load Case 3

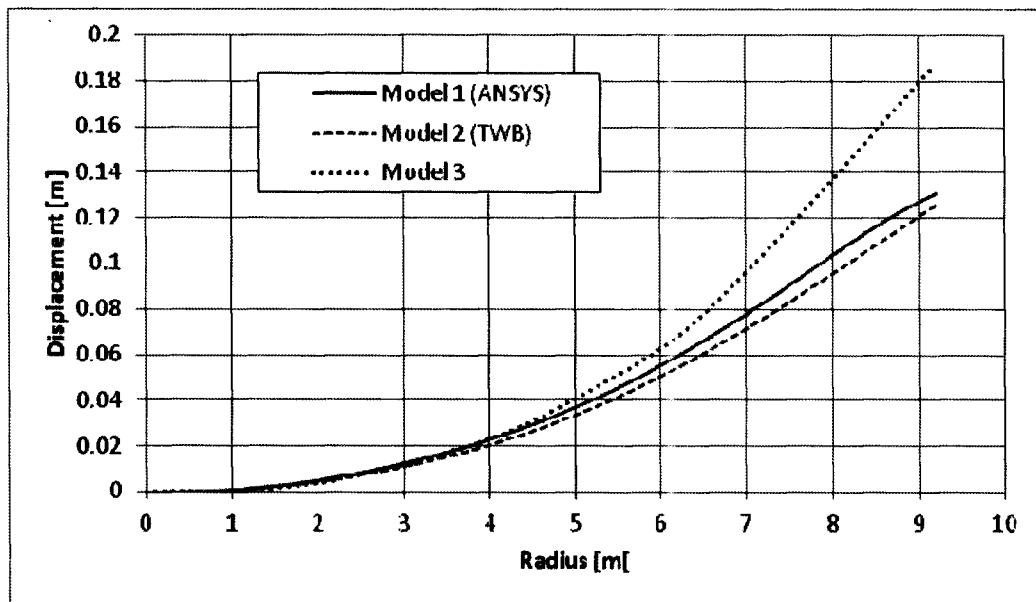


Figure 4.11: Flapwise displacement curves for Load Case 4

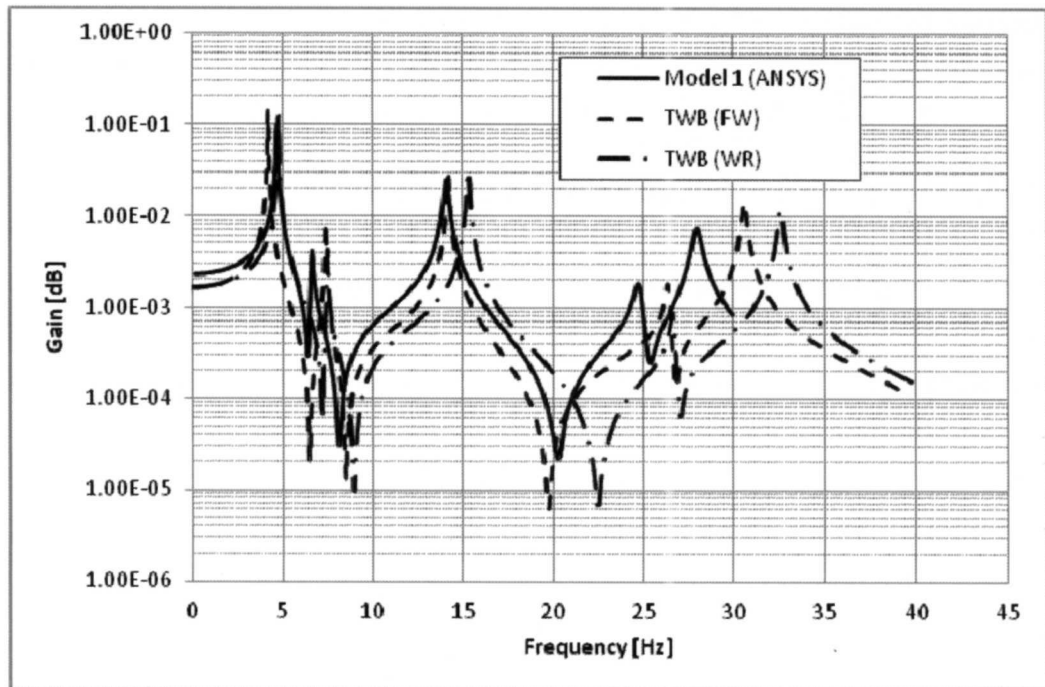


Figure 4.12: Point-FRF for flapwise tip DOF

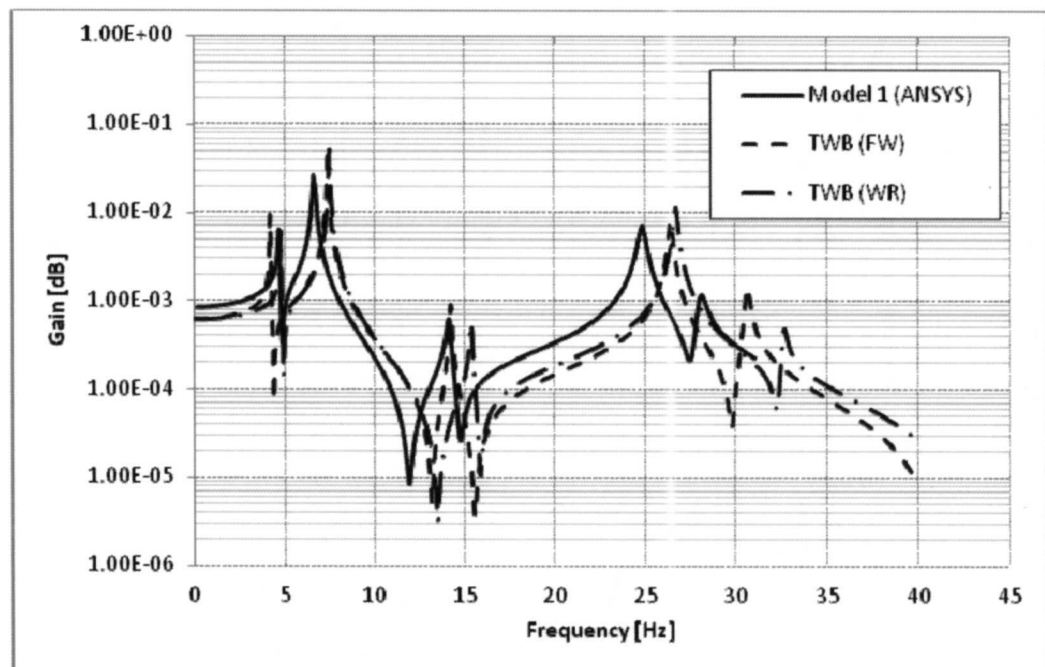


Figure 4.13: FRF for edgewise tip DOF (excitation at flapwise tip DOF)

4.4. Conclusion

In this chapter a numerical validation has been conducted of a TWB (Thin-Wall Beam) 1D finite element (FE) model of a realistic wind turbine blade against an industry-standard FE 3D-shell model built in commercial software (the benchmark, here referred to as Model 1). Based on the theory developed by Librescu and others [1-7], a MATLAB[®] implementation of a TWB model (here called Model 2) was customized to represent the complex geometry and material layup of a 9.2m composite blade previously reported in literature [8]. This report used a 3D shell FE model built in ANSYS[®] (here labeled Model 3) to simulate the blade's static and dynamic behaviour, via the study of several load cases. However, due to some missing data regarding geometry and material layup of the blade's root-end, which plays a significant role in the blade's overall stiffness, it was decided to generate a similar ANSYS[®] model (Model 1) assuming such data. The resulting DOF-size of Models 1, 2 and 3 was, respectively, 55,356, 217 and 66,936.

Model 1 and 2 were solved each in its native software, computing the first six natural frequencies, displacements for four linear static load cases, and flapwise and edgewise frequency response functions (FRF). Overall, it was demonstrated that, in spite of large differences in models' features and sizes, a fair prediction of static and dynamic behaviour was achieved by the TWB model (Model 2). Some specific findings are:

- The first five natural frequencies of Models 1 and 2 exhibited a good match, with deviations ranging from 0.73% (mode 3) to 11.30% (mode 2). The mode shapes, as quantified by their extensional-bending-torsional couplings, exhibited a very good agreement for all cases. As expected for FE solutions, higher modes showed increasing disagreement, with a deviation of 20.05% for the natural frequency of mode 6. Regarding Model 3, and in spite of the aforementioned uncertainties, the reported natural frequencies were comparable to those of Models 1 and 2. Thus, it can be concluded that information yielded by the first five modes of the TWB model (Model 2) can be trusted for applications dealing with system identification, damage propagation and alike.
- Results for the linear static load cases 1 to 4 demonstrate that this TWB model is suitable for general aerodynamic analyses. This can be seen in Figure 4.9 to Figure 4.11, where Models 1 and 2 can be seen to exhibit very close deflection

curves along most of the blade's radius. The reported large error in Table 4.3 for load case 3 (27.21% at the tip) is not critical, as the tip element has a negligible contribution to the total aerodynamic load.

- With respect to the plots of the Frequency Response Functions (FRF) for flap- and edgewise excitation, it was found that both peak amplitudes for all modes, as well as the width of all resonances and anti-resonances (indicating a similar damping behaviour), are reproduced very well by the TWB model. The warping boundary condition was found to have some impact on the accuracy of the location of the natural frequencies, with Free Warping (FW) showing a somewhat better accuracy than Warping Restrained (WR) for all modes but the lowest. Given the complexity of the blade structure and the realistic details included in the modeling process the overall accuracy is considered to be good. It should be pointed out that all conclusions are for this particular (realistic) test case, and that no claim is made that the model used will be performing equally well for arbitrary geometries, materials layups, and load conditions.

Based on the experiences of the test case studied it can be concluded that the computationally inexpensive TWB model studied here is suitable for a quick and efficient recursive analysis at the blade design stage. It should be recalled that the TWB formulation cannot, due to inherent limitations, capture the whole dynamics of either a real blade or a comprehensive numerical counterpart. However, it was found that such a model is indeed capable of approximating the quasi-static and low-frequency behavior with a reasonable overall accuracy. It is worth noting that aeroelastic codes, such as FAST developed at the National Renewable Energy Laboratory (NREL), uses only two mode shape in flapwise direction and just one in edgewise in order to reproduce the complete dynamic response of the blade. TWB formulation allows advanced features, such as transversal shear, geometric nonlinearities and tapered section, to be incorporated in a straightforward fashion (although the present application was, for the time being, restricted to linearity). Based on these results, it is suggested that the developed model could be used for more advanced dynamic simulations involving realistic wind loads and damage progression. In particular, future work will tackle the development of Progressive

Failure Analysis (PFA) based on the introduced blade model running in aeroelastic simulation.

References

- 1 Librescu L, Song O. *Thin-walled Composite Beams: Theory and Application*. Springer, 2006
- 2 Phuong T, Lee J. Free vibration of thin-walled composite box beams. *Composite Structures* 84 (2008) 11-20
- 3 Librescu L, Na S. Active vibration control of doubly tapered thin-walled beams using piezoelectric actuation. *Thin-Walled Structures* 39 (2001) 65–82
- 4 Qin Z, Librescu L. On a shear-deformable theory of anisotropic thin-walled beams: further contribution and validations. *Composite Structures* 56 (2002) 345–358
- 5 Oh S, Song O, Librescu L. Effects of pretwist and presetting on coupled bending vibrations of rotating thin-walled composite beams. *International Journal of Solids and Structures* 40 (2003) 1203–1224
- 6 Piovan M, Cortinez V. Mechanics of shear deformable thin-walled beams made of composite materials. *Thin-Walled Structures* 45 (2007) 37–62
- 7 Vo P, Lee J. Geometrically nonlinear analysis of thin-walled composite box beams. *Computers and Structures* 87 (2009) 236–245
- 8 Locke J, Valencia U. *Design Studies for Twist-Coupled Wind Turbine Blades*. SAND2004-0522. Wichita, KS: National Institute for Aviation Research 2004
- 9 Dancila DS, Armanios EA. The influence of coupling on the free vibration of anisotropic thin-walled closed-section beams. *Int. J. Solids Structures*. 1998; 35: 3105-3119.
- 10 Song O, Librescu L, Jeong NH. Static response of thin-walled composite I-beams loaded at their free-end cross-section: analytical solution. *Composite Structures* 2001; 52: 55-65.
- 11 Deeks, A, Hao H. *Developments in Mechanics of Structures and Materials*. Volume 2. Taylor and Francis Group, London 2004
- 12 ANSYS Structural Analysis Guide Release 8.1 (2004), Swanson Analysis Systems Inc.
- 13 Burton T, Sharpe D, Jenkins N, Bossanvi E. *Wind Energy Handbook*. Wiley 2001

Chapter 5.

Progressive Failure Analysis of Thin-Walled Composites Structures

Chapter Summary

A reduced-order finite-element model suitable for Progressive Failure Analysis (PFA) of composite structures under dynamic aeroelastic conditions based on a Thin-Walled Beam (TWB) formulation is presented in this chapter. Validation of the PFA-TWB against an integrated PFA model based on a shell formulation and implemented in the commercial software tool GENOA is conducted for static load conditions.

In the present chapter a Progressive Failure Analysis (PFA) Thin-Wall Beam (TWB) Finite Element (FE) model designed to predict the progression of damage in slender complex structures like rotor blades is described. As opposed to the work reviewed previously, this model is capable of continuously updating the structural properties of the blade as damage progresses, thereby providing an integrated description of failure propagation. The selected TWB model was originally developed by Librescu and co-workers [1-4] and subsequently discretized via FE by Vo and Lee [5-7]; an application of the Librescu-Vo-Lee model to a realistic turbine blade was described in [8]. The TWB model allows including material anisotropy, arbitrary laminate layups and shear deformability and has shown to reproduce the fundamental structural behaviour of 3D shell models with reasonable accuracy [8]. Stress/strain fields for individual layers can be recovered based solely on the knowledge of the nodal displacements obtained from the effective 1D finite-element model, thereby allowing for Progressive Failure Analysis (PFA) at any layer and position of the structure. A further advantage is the availability of

analytical expressions for the stiffness of arbitrary cross-sections, making damage tracking a more straightforward task during a displacement-based FE analysis. For purposes of validation of the PFA-TWB model described here, the failure criteria proposed by Chamis and Minnetyan [9] were used, since these criteria are implemented in the GENOA package, a commercial software tool designed for composite failure analysis in complex structures [10]. As a case study the methodology presented was applied to the helicopter blade described by Pawar and Ganguli [11,12] for the case of static loads. Application of the model to damage progression under dynamic aeroelastic conditions will be reported in the next chapter.

5.1. Methodology

The integrated TWB-PFA model described in the preceding paragraph was developed and implemented for the purposes of real-time dynamic failure analysis under realistic load conditions; however, the objective of the present paper is to present a validation of the model against a static model implemented in the GENOA package.

5.1.1. Integrated Thin-Walled Beam Progressive Failure Analysis model

The Thin-Walled Beam (TWB) model used in the present work is based on the formulations given in references [1-7]; an application of the TWB formulation to a realistic wind turbine blade has been described in [8]. The main aspects of the TWB model will be briefly reviewed below.

The TWB model is an effective one-dimensional representation of beam-type structures such as helicopter or wind turbine blades, capable of recovering full 3D strain and stress information based on the knowledge of the nodal displacements of the 1D model alone. Evidently, a certain set of conditions has to be obeyed in order to allow such a reconstruction of information. These conditions are the following [6]: (1) The structure is restricted to small strain values, (2) the beam cross sections remain undeformed in their own plane for all load conditions applied, (3) both the transverse shear strains γ_{xz}^0 , γ_{yz}^0

and warping shear γ_{ω}^0 are uniform over the cross section, (4) the Kirchhoff–Love assumption in classical plate theory remains valid for laminated composites.

Based on these assumptions, a double integration of geometric and materials properties of the cross-section (through the wall and along the contour) can be conducted, yielding semi-analytical expressions for the stiffness tensor (E_{ij}) of arbitrary cross-sections. Since the coefficients E_{ij} contain detailed information about the stiffness of any material point in the shell (as specified by its angular and thickness location), the full deformation and stress fields can be recovered for post-processing purposes, such as for the application of failure criteria for composites. If a failure criterion is met at a given location in the structure, the corresponding elastic moduli at this location may be degraded according to the failure model chosen. The stiffness tensor can then be updated and a new set of nodal displacements may be calculated.

The traditional approach is to conduct the elastic calculations and the failure analysis separately; then a progressive failure analysis often becomes a tedious process, even in the case of static loads. PFA for dynamic loads, on the other hand, is practically impossible with this approach. The use of reduced-order model such as TWB, on the other hand, allows implementing a coupled procedure potentially capable of analyzing the progression of damage under dynamic load conditions in real-time.

Reduced-order models necessarily come at the expense of accuracy, so it is important to evaluate the validity of the assumption of the model (1-4) under the load conditions studied and identify a range of applicability of the model. One of the key assumptions which may be violated under severe load conditions is the hypothesis that the contours of the beam sections remain constant (assumption 2 of the TWB); this validity of this assumption will be further examined in the results section.

A Timoshenko formulation is used with seven independent variables given by the node translations $U(z)$, $V(z)$, $W(z)$ where z is longitudinal or beam axis, the angular displacement $\varphi(z)$ of the cross sections around the z axis, and the angular displacements $\psi_x(z)$, $\psi_y(z)$, $\psi_{\omega}(z)$ around the x , y , and warping directions, respectively.

Once the FE displacement field (axial direction and shear) has been calculated, the deformation field is recovered as follows:

$$\begin{aligned}\varepsilon_{zz} &= W_0' + \psi_y'(x + n \sin \theta) + \psi_x'(y - n \cos \theta) + \psi_\omega'[F(n, s)] \\ \gamma_{sz} &= \gamma_{xz} \cos \theta + \gamma_{yz} \sin \theta + \gamma_\omega[r - n - F_t(s)] + \varphi'[F_t(s) + 2n]\end{aligned}\quad \text{Eq. 5.1}$$

The stress field can be calculated for arbitrary materials layups, where each lamina k with the composite material obeys a constitutive law given by:

$$\begin{Bmatrix} \sigma_{zz} \\ \sigma_{sz} \end{Bmatrix}_k = \begin{bmatrix} \bar{Q}_{11}^* & \bar{Q}_{16}^* \\ \bar{Q}_{16}^* & \bar{Q}_{66}^* \end{bmatrix}^k \begin{Bmatrix} \varepsilon_{zz} \\ \gamma_{sz} \end{Bmatrix}_k \quad \text{Eq. 5.2}$$

where the coefficients \bar{Q}_{ij}^* are obtained from the lamina's stiffness coefficients, as defined in a local reference frame given by the materials principal axes, in the following manner: First the 3D orthotropic law is reduced to plane stress/strain conditions [13], and subsequently a transformation from the local to the global coordinates is performed. Once the finite-element stress field has been calculated, it must be transformed back to the local (material) coordinates in order to evaluate the chosen failure criteria at each layer:

$$\begin{bmatrix} \sigma_{11} & \sigma_{12} \\ \sigma_{21} & \sigma_{22} \end{bmatrix}^K = [T] \begin{bmatrix} \sigma_z \\ \sigma_{sz} \end{bmatrix}^K [T]^T \quad \text{Eq. 5.3}$$

where the subscripts 1 and 2 identify the directions along and transverse to the fibre, respectively, and $[T]$ collects the director cosines between the global and local coordinate systems. The local stress values calculated in this manner can then be compared with the selected failure criteria. In the present case, the failure criteria proposed by Chamis and Minnetyan [9] have been chosen. No failure occurs while the local stresses at each lamina remain within the limits shown below:

$$\begin{aligned}S_{11}^c &< \sigma_{11} < S_{11}^t \\ S_{22}^c &< \sigma_{22} < S_{22}^t \\ S_{12(-)}^s &< \sigma_{12} < S_{12(+)}^s\end{aligned}\quad \text{Eq. 5.4}$$

where S_{11}^c and S_{11}^t are the strength values for the compressive and tensile stress, respectively, for the along-fibre direction. Similarly, S_{22}^c and S_{22}^t are the in-plane compressive/tensile strength values for the direction perpendicular to the fibres; $S_{12(-)}^s$ and $S_{12(+)}^s$, finally, are the in-plane shear strength values. The reason for choosing the Chamis-Minnetyan criteria over other, often more elaborate, failure criteria lies with the fact that these criteria have been implemented in the GENOA package [11] designed for progressive failure in a shell-based environment, thereby providing a useful reference tool against which the reduced-order model presented here can be compared (see section 2.2 for a brief introduction into GENOA). For the current analysis modified distortion energy (MDE) failure criterion of GENOA was not enabled to facilitate comparison with the TWB-PFA model.

5.1.2. Implementation of the integrated TWB-PFA model

As stated above, for the purposes of the present work only static load vectors are considered.

Figure 5.1 shows the flowchart of this implementation, as described in the following.

The general procedure consists in an iterative process where the materials properties are progressively degraded as the load is gradually increased. The initial step of each loop of a static TWB-PFA simulation consists in the definition of a nodal load vector; $\{f\} = \{f_0\}$ at the first iteration. Then, the TWB finite element model is solved for nodal displacements, where the current materials properties of the blade are used; the nodal displacements are stored in the vector $\{u\}$. Subsequently, the strain and stress field tensors expressed in the (n, s, z) coordinate system used by the TWB formulation are obtained for all layers and all azimuthal and spanwise locations. The stress tensor is then transformed at each layer into the corresponding materials coordinate system by means of a passive rotation (see Eq. 5. 3); this coordinate system is understood as the one defined by the principal axes of the corresponding material at this layer. Once the stresses in a given layer are known, the failure criteria given by Eq. 5. 4 can be evaluated. If no increase in damage is found, the nodal load vector $\{f\}$ is increased by a small step Δf_i , and the analysis is repeated. If, on the other hand, the increase in damaged volume is higher than a

percentage pre-defined by the user, the load is reduced by Δf_2 ($|\Delta f_2| < |\Delta f_1|$), i.e. to an intermediate value between the last two. The objective of this procedure is to avoid too large increases in damage in one simulation step, which would lead to a loss of resolution. If a non-zero permissible damage level is observed in this step, then the load is maintained at a constant level for several simulation steps until the damage stabilizes. Only after stabilization the load is increased again. Progressive failure analysis (PFA) takes place whenever an acceptable (e.g. sufficiently small) increase in damage volume occurs. In such a case, materials properties are updated according to the type of damage yielded by the evaluation of the failure criteria, which in turns requires updating the TWB model, leading to updated nodal displacements, strain/stress fields and new damage assessment, all for the same amount of load $\{f\}$. This PFA cycle is iterated until damage stabilizes for a given load level $\{f\}$. Simulation ends when the percentage of damaged volume, as pre-defined by the user, is reached in one or more TWB elements.

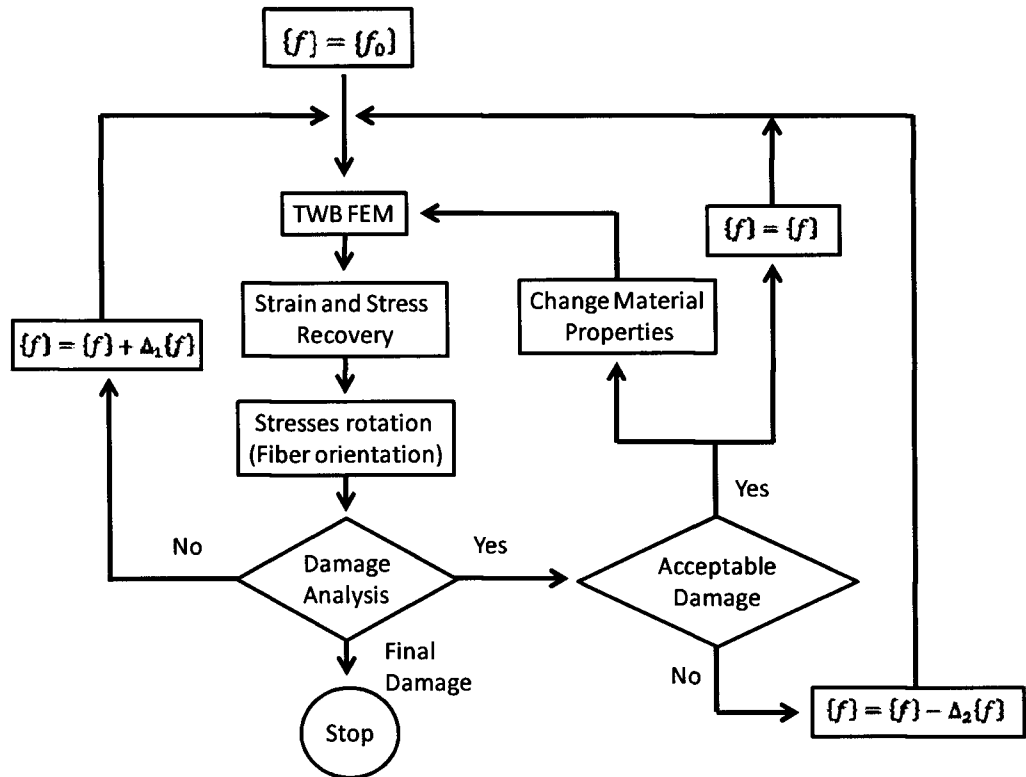


Figure 5.1 : PFA simulation cycle

5.1.3. Description of case study

Both the reduced-order TWB-PFA model presented in this work and the GENOA package were used to conduct a comparative study for the damage prediction in a structural model of a helicopter blade as described by Pawar and Ganguli [11,12]. The blade's external geometry is based on the NACA 0012 airfoil with a constant 305 mm chord and a two-cell cross sectional area, as shown in

Figure 5.2; the total blade length is 5080 mm. The D-spar and skin sections are divided at 35% of the chord. The blade reported in [11,12] does not specify the use of a web; however, in this work both webless and webbed cases were simulated in order to facilitate extending results to wind turbine blades. For the latter case, the web consisted of a 2mm width solid cross-section the centreline of which is located at 35% of the chord, running throughout the entire length of the blade. Table 5.1 lists the elastic and strength materials properties for Carbon Fibre Reinforced Polymer (CFRP, used for the D-spar and Skin sections) and Balsa (used for the web) used in the blade. Table 5.2 details the material layup for the D-spar and Skin sections, specifying the thickness of each layer from the outmost to the innermost.

Based on the databases corresponding to Table 5.1 and Table 5.2, two FE models were generated: Model 1 consists of 13,600 4-node shell elements, 13,467 nodes and 80,802 Degrees of Freedom (DOFs) and was subjected to Progressive Failure Analysis using GENOA. Model 2 consists of 100 TWB elements, 101 nodes and 707 DOFs. Both models were subject to equivalent boundary conditions (fixed at the root end) and loading (tip force applied in the out-of-plane direction). The loads in the shell model are distributed in all the nodes located at the blade tip, producing no torque around the blade axial axis. To assess the extent of cross-section deformation in the Shell model and therefore the range of applicability of the TWB-PFA model, two versions of model 1 (webless and webbed) were constructed.

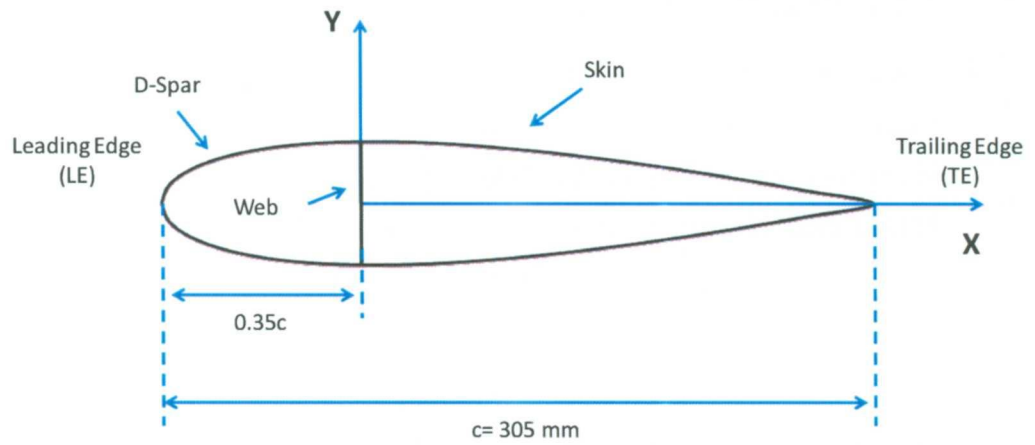


Figure 5.2: Cross sectional area of the blade

Table 5.1: Material elastic and strength properties

	CFRP (D-spar and Skin)	Balsa wood (web)
E11 (MPa)	206,000	2,070
E22 (MPa)	20,700	2,070
G12 (MPa)	8,300	848
V12	0.30	0.22
SL11 T (MPa)	1,979	13
SL11 C (MPa)	1,000	13
SL22 T (MPa)	59	13
SL22C (MPa)	223	13
SL12S (MPa)	103	3

Table 5.2: Material layup for the airfoil profile, listed from the outmost to the innermost layer.

# Layer	D-Spar		Skin	
	Thickness (mm)	Fiber Angle (deg)	Thickness (mm)	Fiber Angle (deg)
1	0.762	0	0.381	0
2	0.508	45	0.508	45
3	0.508	-45	0.508	-45
4	1.016	90	0.254	90
5	0.508	45	0.508	45
6	0.508	-45	0.508	-45
7	0.762	0	0.381	0

5.2. Results and discussion

Figure 5.3 illustrates the overall blade tip response during PFA. It can be observed that the three models (shell webless, webbed and TWB) have identical flexural stiffness for small loading, the region where no or only negligible damage would be expected. It should be noted that the reduced-order (TWB) model provides an excellent reproduction of the predictions of the far more detailed shell model. For higher loadings, the webless shell model exhibits a rapid decrease in flexural stiffness, explained by the collapse of the blade's cross section, with a deviation from the other models of about 10% at a tip load of 1000N and a rapidly growing discrepancy for higher loads. This reduction in flexural stiffness can be traced back to a collapse of the cross-sectional area of the webless blade, as illustrated in Figure 5.4. In this figure the cross section measured at 450mm from the root end has been plotted for different values of the tip load. Interestingly, a reduction in cross-sectional area can be observed for load values well before a difference in flexural response becomes conspicuous, with the onset of the cross-sectional collapse occurring for load values as low as 200N. The webbed shell model, on the other hand, maintains its cross-sectional area up to load values well into the region where structural damage occurs,

as shown below. For a load value of 1000N the reduction of the cross section is barely 5%, and still for 1500N the decrease is limited to about 10%. It is evident from these findings that the load carrying capabilities of the blade are widely extended by the use of the web, in accordance with good engineering practices in other fields, such as wind turbine blade engineering [14]. Apart from providing higher load carrying capacity, the use of the web ensures the approximate constancy of the cross-sectional area and justifies the use of the TWB model used in this work. After these introductory findings, the core of the result section will concentrate on the comparison of the TWB and the webbed shell model.

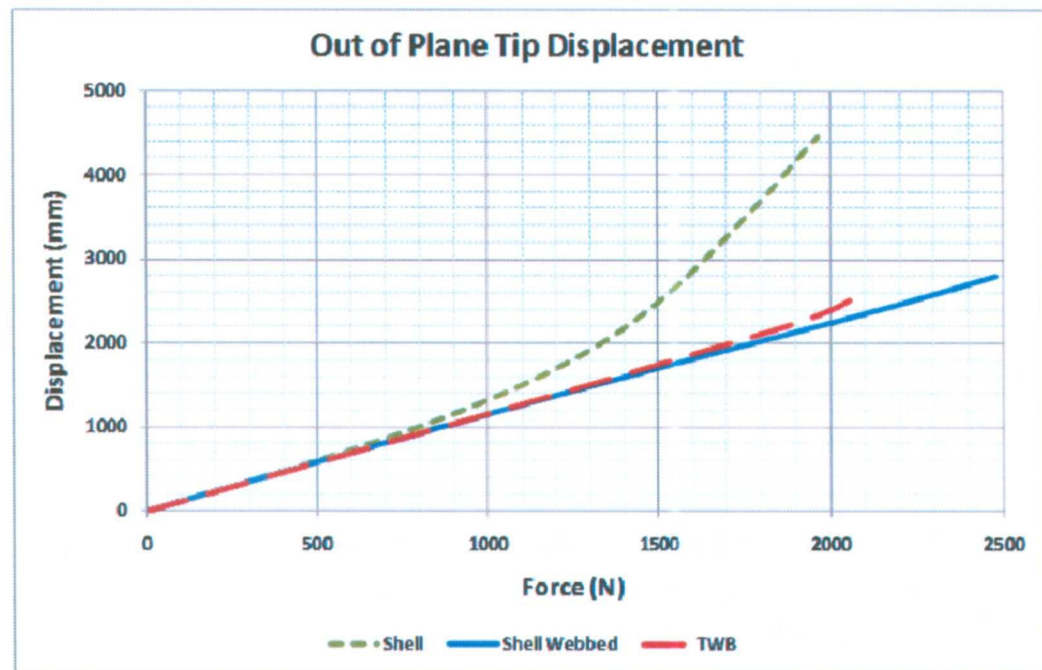


Figure 5.3: Out-of-plane blade tip displacement versus applied load

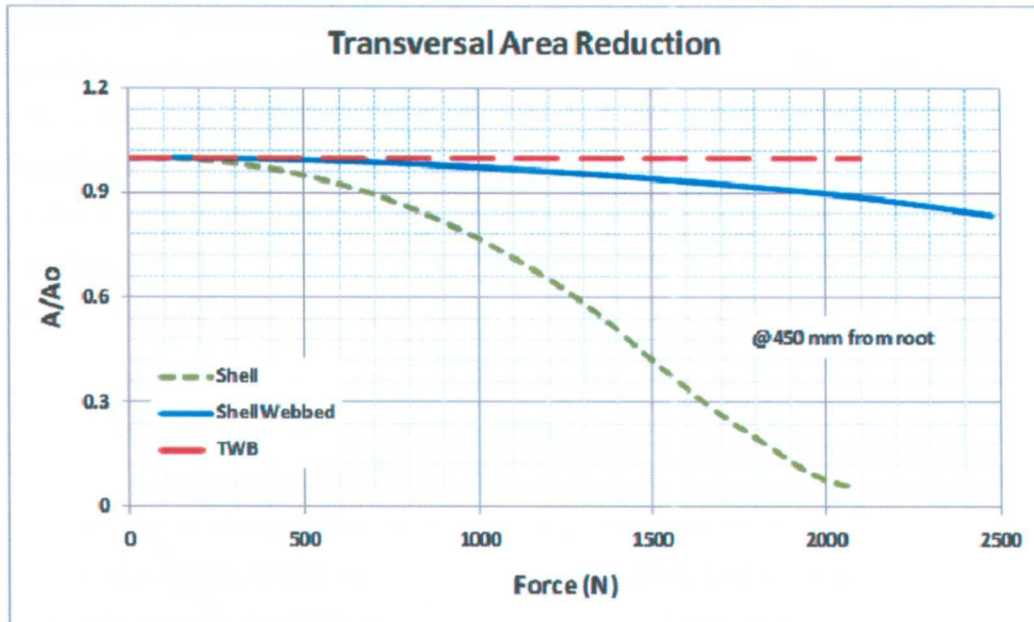


Figure 5.4: Evolution of the blade cross-section at 450 mm from the root end as a function of the applied load

In a first level of analysis the total damage volume of both the TWB and the shell models was calculated and plotted against the load value (Figure 5.5). Total damage volume is understood as the sum of damaged TWB or shell elements, respectively, resolved both by layer and span/contour-wise location. It is conspicuous that the prediction of the onset of damage is very similar in the TWB and webbed shell model, with an initial damage occurring at a load of about 1250N in the case of the TWB model and 1300N for the shell model. This corresponds to an error of about 3.8% in the prediction of the load where initial damage occurs, a fairly reasonable agreement. It should be noted that the TWB errs on the safe (conservative) side. Consistent with the slightly earlier onset of damage in the TWB model is the larger rate of increase with load which amounts to about 1.5% per 1000N of load for the TWB in the linear region of Figure 5.5 versus 1.2% per 1000N of load for the (webbed) shell model. While this difference in slope is far more substantial (25%) than the difference in the damage onset values, the subsequent layer-resolved damage analysis (below) will demonstrate that this discrepancy is actually much smaller if more appropriate error metrics are used. For the moment it can be stated that the general trend predicted by the TWB and the webbed shell

model beyond initial failure is very similar, including the change of slope occurring at about 2000N. Not unexpectedly, the webless model shows an onset of damage at about 1050N, well before the TWB and the webbed shell model. At this load value the cross-section at 450mm from the root end (Figure 5.4) can be seen to be partially collapsed (at about 75% of its original area), leading to significant loss of the section's structural properties. In the following, the comparative study will not further consider the webless model.

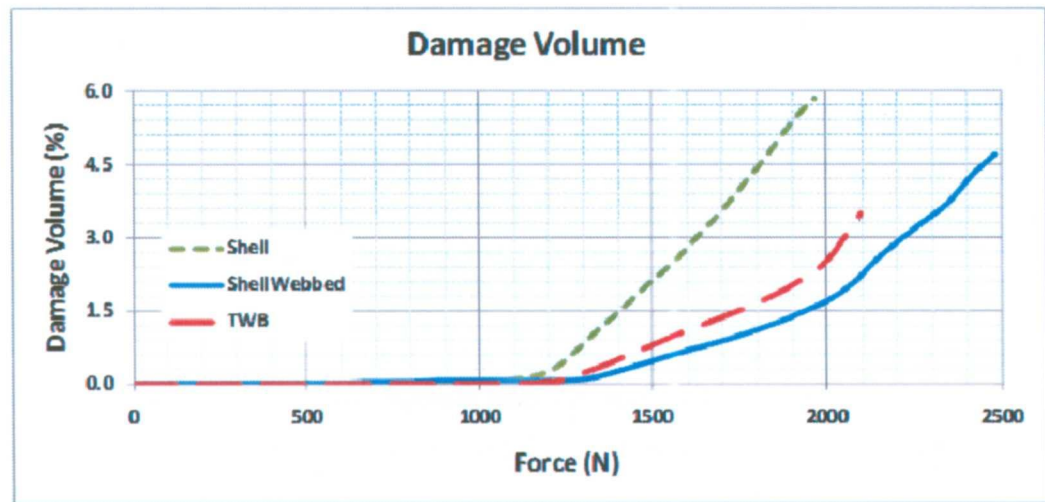


Figure 5.5: Percentage of damage volume vs. load for the three blade models

As stated earlier, the main motivation for using the TWB-PFA model described in this work is its capability of providing detailed damage maps for different load values, thereby allowing to use the model as a structural design tool, identifying and modifying critical areas in a sequence of rapid design cycles. In the following only the webbed shell and the TWB will be compared in detail. Only layers 4 and 7 of the thin-walled structure present damage at any of the load values studied. This finding is consistently predicted by both the TWB and the shell model. In order to compare the predictions of both models in a detailed manner, a damage map for layer 4 has been plotted for four different load values for both the TWB and the shell model; the results are shown in Figure 5.6. Damaged cells are shown in red (dark) on top of the backdrop of a three-dimensional visualization of the

blade, where undamaged cells are displayed in light blue. Please note that due to the different visualization tools used the scales of the blade displacements are different in the TWB and the shell part, respectively. Please refer to Figure 5.3 for a demonstration of the fact that the blade displacements of both models are essentially identical for identical loads. It should also be noted that due to the algorithmic nature of the load variation in both PFA tools the load value sequences corresponding the two models in Figure 5.6 are not identical, although reasonably similar.

It is conspicuous from Figure 5.6 that the damage maps for corresponding loads at layer 4 are strikingly similar between the two models. Most importantly, both models predict the occurrence of damage under tensile stress only. Secondly, in both cases the damage zone is a tongue-like structure which propagates from the root zone towards the spanwise direction. While the damage region at the lowest load value shown in Figure 5.6 is a little larger in the TWB model than the corresponding region in the shell model, the increase in size is practically identical in both cases. Taking the total length of the damage size as one possible metric, a linear increase as a function of load can be observed for load values higher than about 1600N (the three highest load cases for both models). This increase is 1.84 mm per N of load for both models. If the first load point is included (leading to a somewhat less linear relationship), then the incremental length of the damage zone is 2.2 mm / N for the shell model and 2.3 mm / N for the TWB model, still only a 5.5% difference. The striking similarity of the topology of the damage zones for the two models is further illustrated by a plane map for the four load cases studied (Figure 5.7). The similarities include the contour-wise location of the damage zone which is centered at about -60mm for both models. As expected from its more detailed structure, the shell model shows more irregular damage patterns, but the overall topology is very similar.

Damage in layer 4 is caused on the tension side of the blade and occurs because of the 90° orientation of the fibers with respect to the blade axis, leading to a situation where much of the load has to be carried by the matrix. Layer 7, on the other hand, fails on the compressed side of the blade, which can be explained by the fact that the stresses are highest in this layer because of the 0° fiber orientation and the strength for compression loads is relatively low compared to its tensile strength.

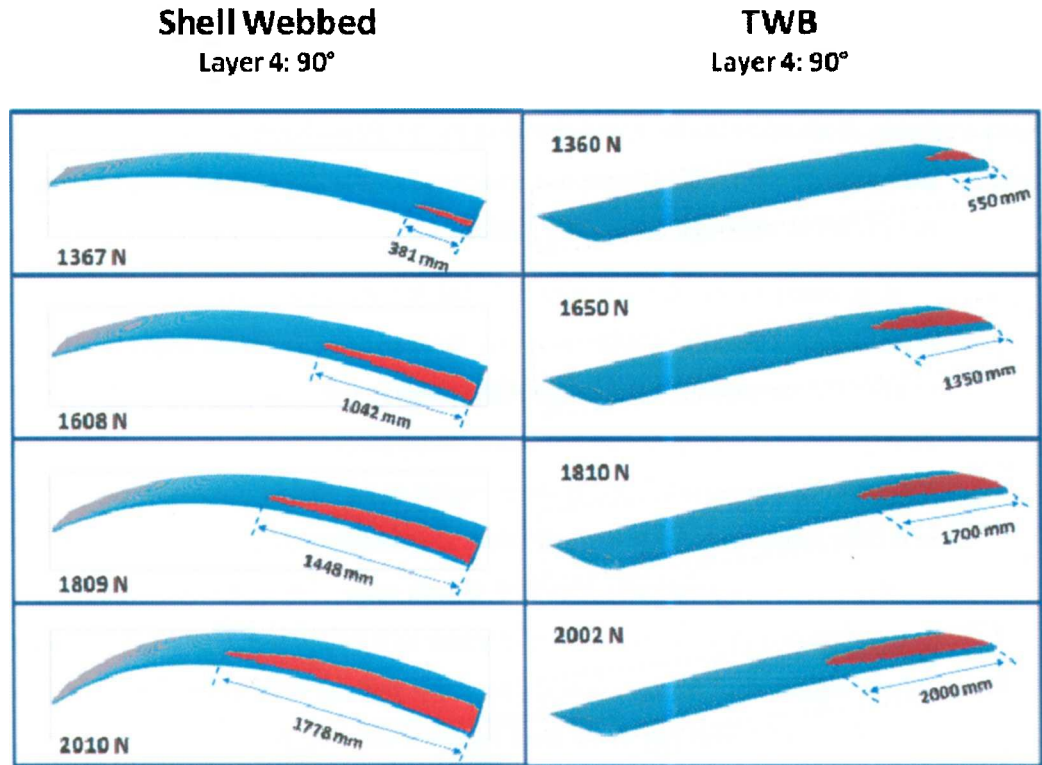


Figure 5.6: Damage Progression of Layer 4 (90°). (a) Plot showing location of damaged cells in layer 4 for different values of the external load as predicted by the GENOA model. (b) Corresponding plot built from the results obtained with the TWB-PFA model. Note that different scales have been used for visualization the deflection of the beam in the GENOA model (a) and the TWB-PFA model (b).

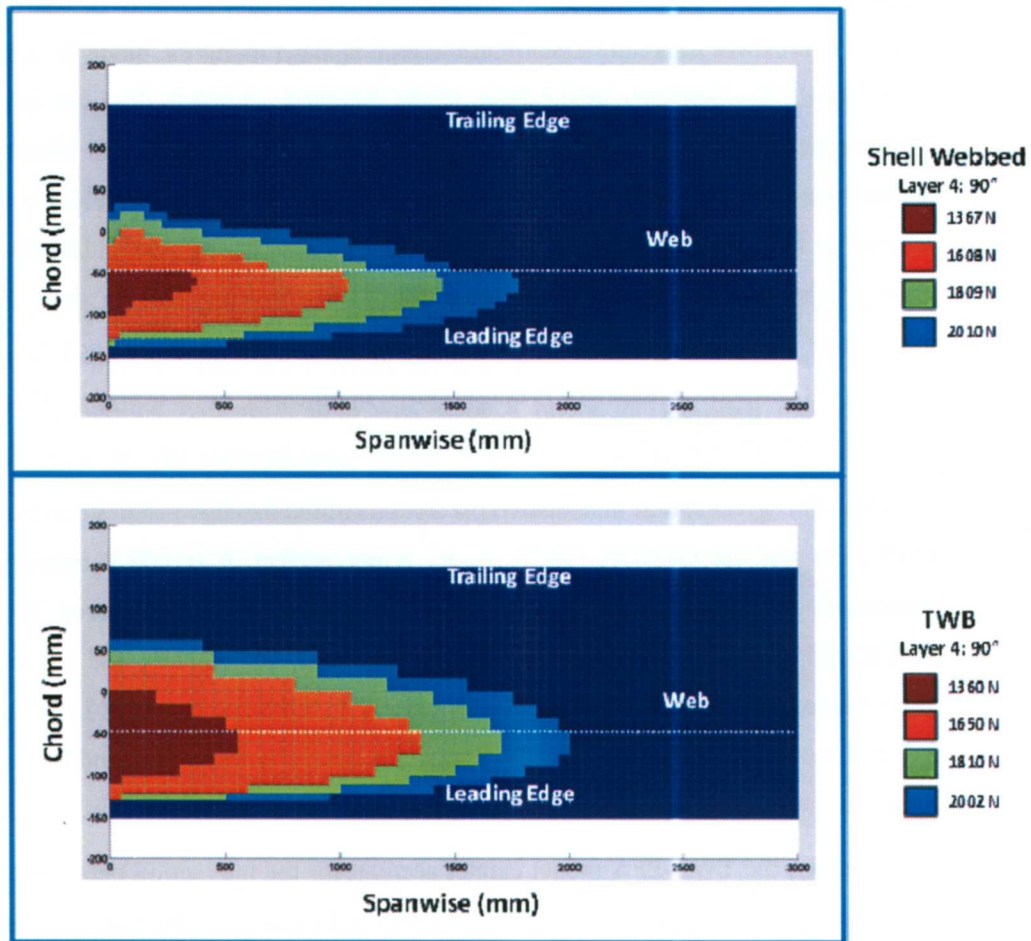


Figure 5.7: Top view of the Damage Progression of Layer 4 (90° fibre orientation). (a) Damage map calculated from GENOA for different values of the tip load. (b) Corresponding damage map obtained with the TWB-PFA model.

Additional insight into the progression of damage at layer 4 can be obtained by studying the cumulative damage along the blade, as shown in Figure 5.8. Three curves have been plotted in the sequence of four subplots, each corresponding to one load situation: The predictions directly obtained from both the TWB and the webbed shell model, respectively, and an additional TWB model output curve with adjusted failure strength values. The adjustment factor was equal for all strength values at a given load, but was allowed to vary among load values. In all load cases a relatively small adjustment

of the strength values used in conjunction with Eq. 5. 4 is sufficient to reproduce the predictions of the more detailed (shell) model. The criterion use to fit the cumulative damage curves was the requirement that the total damage along the blade for a given load value should be identical. In the case of the lowest load value this was achieved by increasing the strength values used in the TWB-PFA model by 6.5%, whereas in the higher load cases the increase was 9.5%, 12%, and 14.5% respectively. A still fairly acceptable fit is achieved if a uniform increase of 10% is used throughout. Even in the cases of the best fits for each load case the TWB-PFA can still be seen to slightly overpredict the damage at the root section, but the error is typically only of the order of a few percent. Moreover, the error is conservative in all cases, i.e. a designer relying on the TWB-PFA model will always err on the safe side.

While the agreement in the detailed predictions of the damage progression between the TWB-PFA and the GENOA (shell) model is not perfect, it is still surprisingly good, particularly if the huge reduction in degrees of freedom (DOF) is considered. Whereas the shell model needs 80,202 DOFs to accurately represent the geometry and materials layup of the blade, the reduced-order model uses only 707 DOFs, a mere 0.88% of the DOFs of the shell model. Consequently, the TWB model is generally more rigid and less capable of accommodating the externally imposed load by straining its internal DOFs.

Evidently, the TWB-PFA model cannot account for the interaction between a web and the blade shell such as in the case of the webbed shell model used here in conjunction with GENOA. As shown in Figure 5.9 and Figure 5.10 for the case of the 1800N load case a needle-like longitudinal damage feature can be seen to emerge in the shell model which is not predicted by the TWB model. This feature can be attributed to the presence of the web in the shell model, leading to a localized concentration of stress in the interface with the web. Apart from this feature, the agreement between the damage topologies predicted by both models is strikingly similar. Regarding the total damage volume at the two load values where damage arises (about 1800 and 2000N), the agreement between the predictions between the TWB and GENOA is remarkably good (about 0.025% at 1800N and 0.3% at 2000N for both models, Figure 5.11).

It should be emphasized that layer 7 represents only a small fraction of the total damage in the blade (0% at the lowest two load values, about 0.025% of the total volume

versus about 1% in layer 4 for the 1800N load case, and about 0.3% versus 1.2% in layer 4 for the 2000N load case), so discrepancies in this layer are of no practical concern at the design stage. Even so, the TWB correctly predicts the onset of damage, the total damage volume and (roughly) even the shape of the damage zone, with the exception of the needle-like feature caused by the presence of the web. This is quite an achievement for a reduced-order model. For forensic analyses, a more detailed model may be indispensable, but at the design stage the TWB-PFA model may be good enough.

A few remarks on computational economy: Setting up the shell model took about 3 person-hours, while the corresponding task for the TWB model was estimated at 0.5 person-hours. Execution time was some 4 hours for the shell model, compared to 5 minutes for the reduced-order model. This difference in set-up and computation time is likely to increase for more complex structures than the helicopter blade studied in the present work.

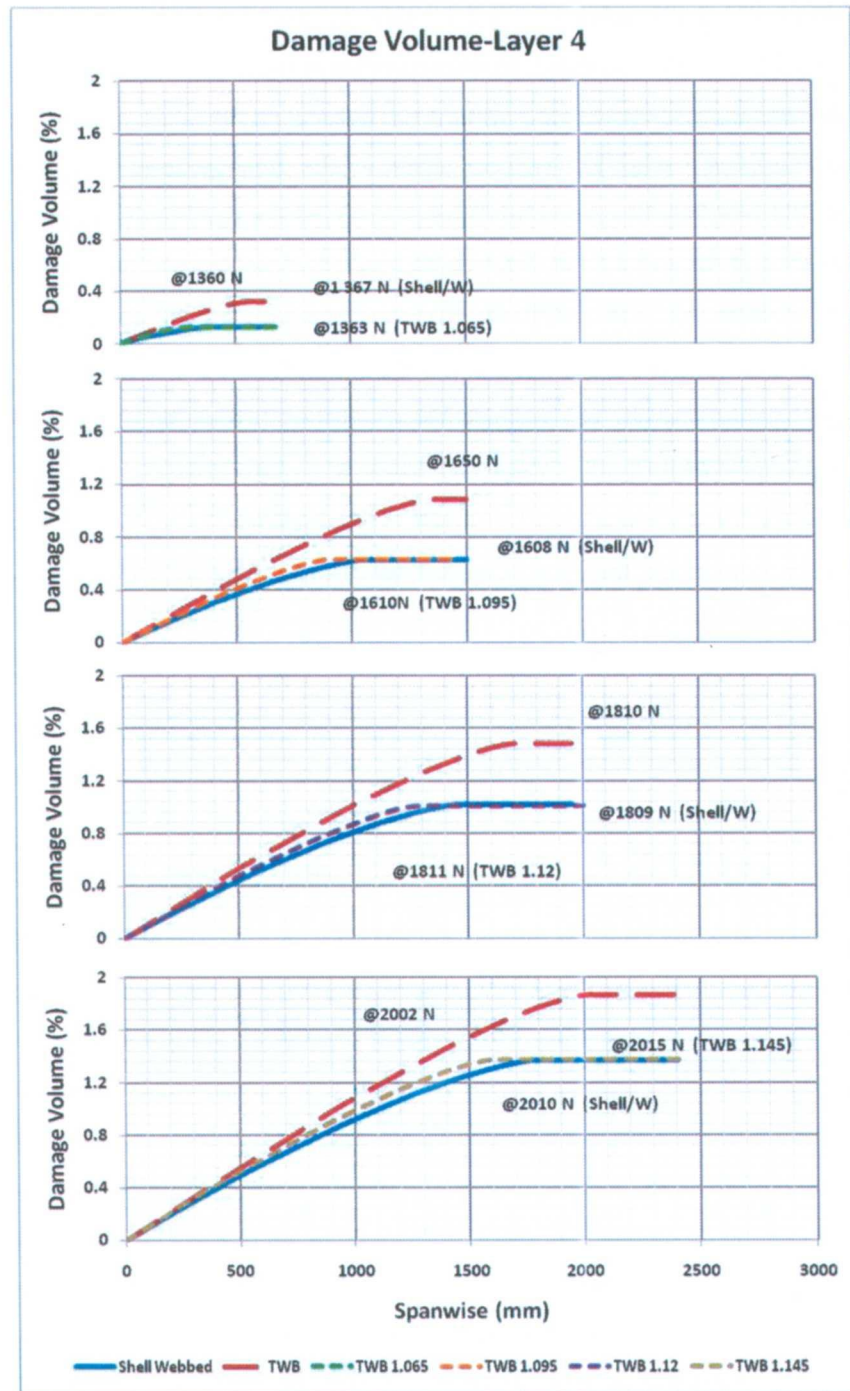


Figure 5.8: Cumulative damage volume as a function of the spanwise coordinate for Layer 4 (90° fibre orientation) and four load cases. Continuous curves: Predictions of the shell model. Dashed curves: Predictions of the unadjusted TWB-PFA model. Fine-dashed curve: Predictions of the TWB-PFA model with adjusted strength values

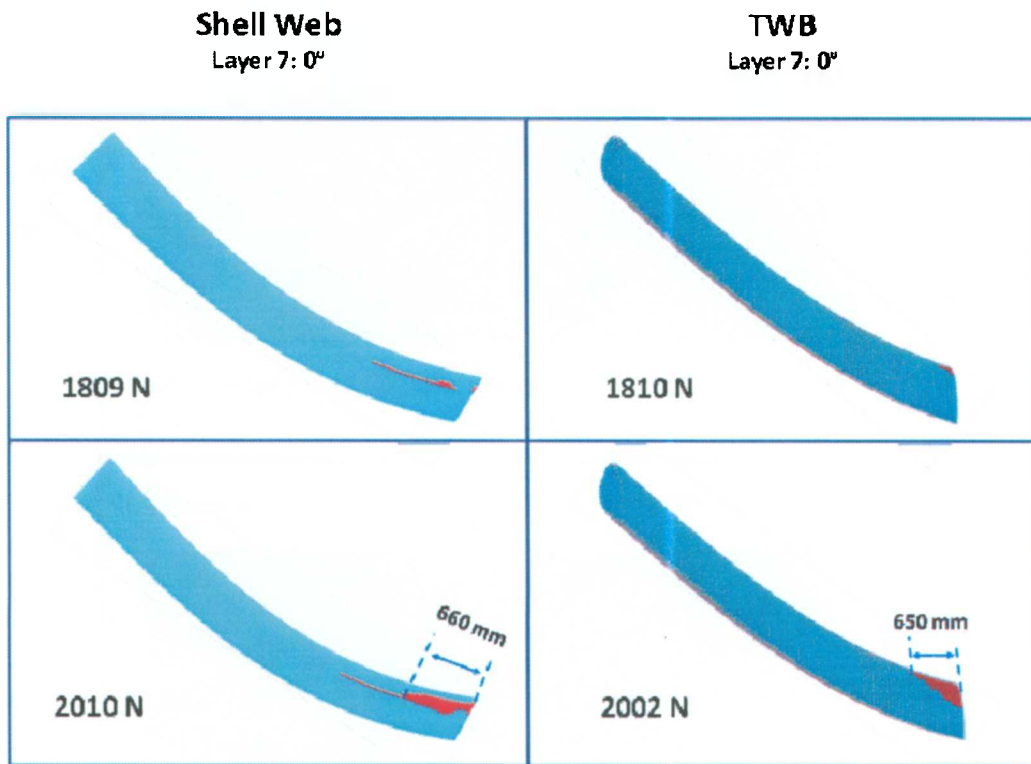


Figure 5.9: Damage Progression of Layer 7 (0°) as shown as damage maps for the two load cases where damage was observed. Left: Predictions of the shell model. Right: Predictions of the TWB-PFA model.

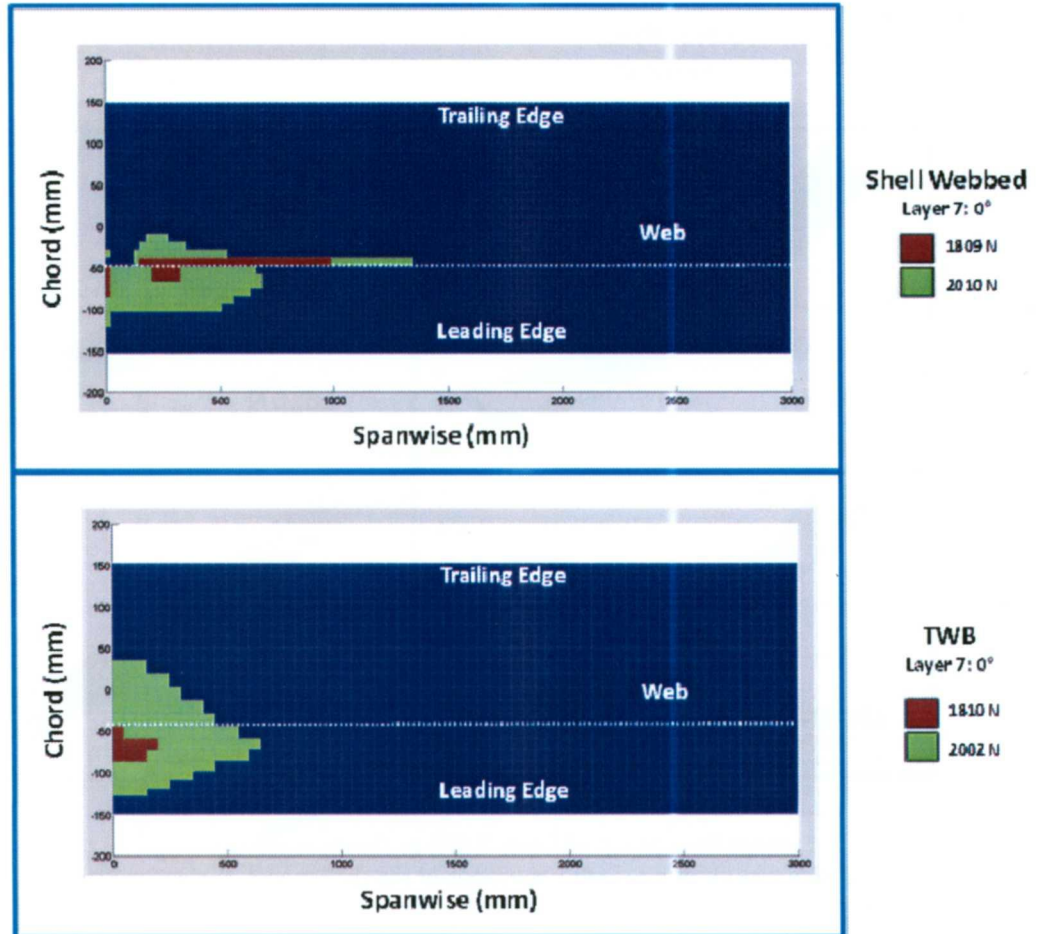


Figure 5.10: Top view of the Damage Progression of Layer 7 (0° fibre orientation). Upper graph: Predictions of the shell model. Lower graph: Predictions of the TWB-PFA model.

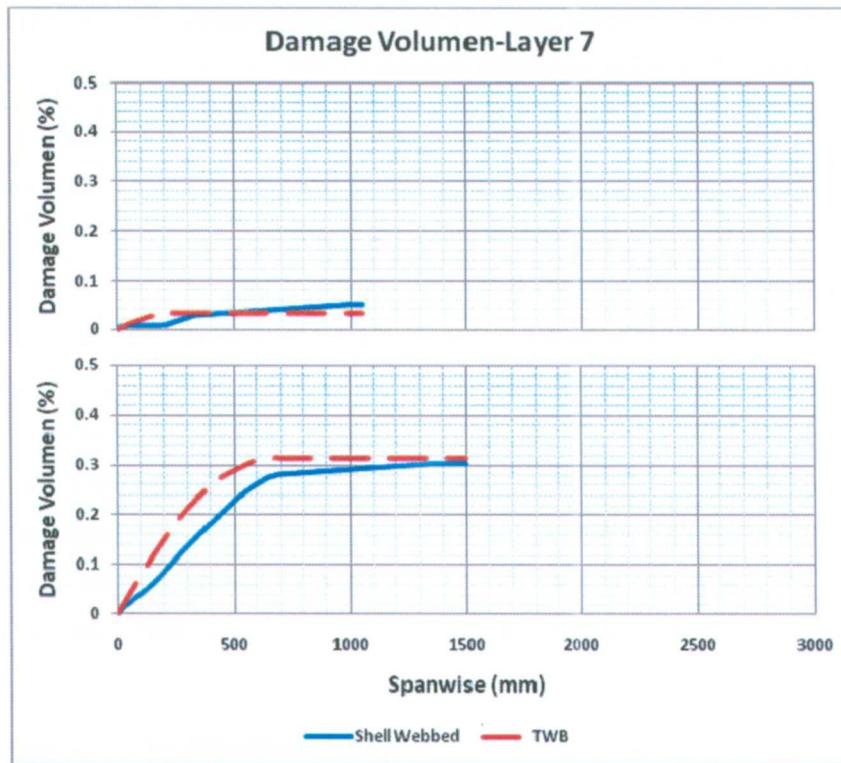


Figure 5.11: Cumulative damage volume as a function of the spanwise coordinate for Layer 7 (0°). Continuous curve: Predictions of the shell model. Dashed curve: Predictions of the TWB-PFA model.

5.3. Summary and conclusions

In the present chapter, a reduced-order thin-wall beam (TWB) progressive failure analysis (PFA) model has been presented and a detailed validation of its predictions for a helicopter blade subject to static tip loads against a more elaborate shell model, built in the commercial PFA software suite GENOA has been conducted. The TWB-PFA represents an equivalent one-dimensional model with a dramatically reduced number of degrees of freedom (DOF) compared to the detailed shell model. In spite of being a one-dimensional representation of the blade, the TWB-PFA model is capable of generating detailed maps of the progressively occurring damage in response to increasing external loads by taking advantage of the analytical relationships between the node displacements and the longitudinal and shear strains which, together with the constitutive laws for each lamina of

the composite material, allowing applying failure criteria to the blade resolved both by layer and by contour-/spanwise position.

Different levels of analysis were carried out in course of the study. At the first level the total damage volume as a function of the external load was calculated for both approaches; a similar value of the onset of damage was predicted by the shell (GENOA) and the TWB-PFA model if the shell model of the blade was equipped with an internal web, thereby avoiding a collapse of the cross sections near the root and ensuring the validity of one of the key assumptions of the TWB model used. The damage-onset value was predicted with an accuracy of about 5.5%, indicating a promising initial evidence for the suitability of the reduced-order model. While the damage after the onset progresses at a rate about 25% higher in the TWB-PFA model (1.5% of damage per 1000N of load vs. 1.2% / 1000N for the shell model), this difference can be substantially reduced by a small adjustment of the strength values used with the failure criteria for the TWB-PFA model, as discussed below.

In a second level of analysis the spatial distribution of the damage was studied for different load levels. Both in the TWB-PFA and the GENOA model damage is predicted in layers 4 and 7 only, and the topology of the damage maps is strikingly similar for both models. In the case of layer 4, where most of the damage occurs, the shape and the contour-wise location of the damage zone predicted by the reduced-order model is almost identical to the predictions of the more complex model, although the total length of the failure zone is somewhat larger for all load cases, which can be traced back to an almost constant offset between the two predictions, since the rate of growth of the length of the failure region is almost identical for both models. In the case of layer 7, where very little damage occurs and no damage is observed until fairly high load values (about 1800N of tip load for both models) the shape of the damage zone is well predicted by the TWB-PFA model except for a needle-like damage feature which can be traced back to the presence of the web in the shell model.

In a third level of analysis the layer-resolved cumulative damage volume as a function of the spanwise coordinate has been calculated for both models as a function of the applied tip load and the predictions have been compared. Consistently with the findings described above, the cumulative damage volume found from the TWB-PFA model is

somewhat higher than in the GENOA model. A possible explanation for this behaviour lies with the locally stiffer structure of the reduced-order model given its much smaller number of degrees of freedom (DOFs) and the correspondingly smaller ability of distributing the strain energy among the DOFs. Another issue refers to the appropriateness of the failure criteria, which may have to be modified for an effective reduced-order model. In order to explore this line of thought the strength values used in the TWB-PFA model were increased by a constant factor and the simulations were re-run for layer 4 and all load cases, matching the total cumulative damage volume. It was possible to quite accurately reproduce the cumulative damage curves of the GENOA model by a relatively small adjustment in materials strength, with the adjustment factor ranging from 1.065 (lowest load case) to 1.14 (highest load case); a constant adjustment factor of 1.1 still yielded acceptable results. The increase in the value of the adjustment factor from 1.065 to 1.14 can be explained by the fact that the damage progressively weakens the contour of the affected sections, thereby allowing for a progressive reduction of the section stiffness due to the decrease in cross-sectional area. As discussed above, this behaviour is correctly modelled by the shell but not the TWB model.

In conclusion, it can be said that the TWB-PFA model presented in this work has shown an encouraging capability of correctly predicting both the onset and the propagation of damage in the composite blade studied for the case of static loads, providing reliable information on the location of the damage zone (resolved both by layer and the contour- and spanwise location of the damage). A small overprediction of the damage compared to the more detailed shell model can be corrected by a small upward adjustment of the (equivalent) strength values to be used in the model. In all cases, the reduced-order model proved to be more conservative than the shell model, so it should be possible to safely use it for design purposes, especially if a series of iteration with quick turnaround times is desired. While the final design of a rotor blade will still remain confined to the domain of higher resolution models such as shell and volume element models, the TWB-PFA approach is a promising tool for pre-design and aeroelastic design simulation, where the use of high-resolution models would be prohibitive.

References

- 1 Song O, Librescu L, Jeong NH. Static response of thin-walled composite I-beams loaded at their free-end cross-section: analytical solution. *Composite Structures* 2001; 52(1): 55-65.
- 2 Librescu L, Na S. Active vibration control of doubly tapered thin-walled beams using piezoelectric actuation. *Thin-Walled Structures* 2001; 39(1): 65–82.
- 3 Qin Z, Librescu L. On a shear-deformable theory of anisotropic thin-walled beams: further contribution and validations. *Composite Structures* 2002; 56(1): 345–358.
- 4 Librescu L, Song O. *Thin-walled Composite Beams: Theory and Application*. Springer, 2006
- 5 Vo T, Lee J. Flexural torsional behavior of thin walled closed-section composite box beams. *Engineering Structures* 2007; 29(8): 1774-1782.
- 6 Lee J, Vo T., Flexural–torsional behavior of thin walled composite box beams using shear-deformable beam theory. *Engineering Structures* 2008; 30(7): 1958–1968.
- 7 Vo T, Lee J. Free vibration of thin-walled composite box beams. *Composite Structures* 2008; 90(2): 11-20.
- 8 Cardenas D, Elizalde H, Marzocca P, Probst O. Numerical validation of a finite element thin-walled beam model of a composite wind turbine blade. *Wind Energy* 2011. DOI: 10.1002/we.462.
- 9 Chamis CC, Minnetyan L. Defect/damage tolerance of pressurized fiber composite shells. *Composite Structures* 2001; 51(2): 159-168.
- 10 <http://www.ascgenoa.com/main/>
- 11 Pawar PM, Ganguli R. Modeling progressive damage accumulation in thin walled composite beams for rotor blade applications. *Composites Science and Technology* 2006; 66(13): 2337–2349.
- 12 Pawar PM, Ganguli R. On the effect of progressive damage on composite helicopter rotor system behavior. *Composite Structures* 2007; 78(3): 410–423.
- 13 Tuttle M. *Structural Analysis of Polymeric Composite Materials*. New York: Marcel Dekke, 2004.
- 14 Lindenburg C, Winkel GD. State of the art of rotor blade buckling tools. Technical report ECN-C–05-054. Energy Center of the Netherlands, 2005.

Chapter 6.

Dynamic Aeroelastic Progressive Failure Analysis of Thin-Walled Composite Structures

Chapter Summary

A thin-wall beam model capable of predicting failure progression under aeroelastic conditions with both stochastic and deterministic loads is presented in this chapter. Damage progression is an integral part of the formulation based on TWB. The model is coupled with a blade element momentum theory model used to determine the aerodynamic load distributions produced by the blades under operational conditions. Simulations include three particular cases corresponding to conditions more critical to those used to design wind turbine blades.

The ever increasing size of modern utility-scale wind turbines makes the assessment of structural properties at an early design stage an indispensable task [1]. Several authors have addressed structural design issues in large wind turbine blades, with a focus on damage propagation. Sutherland and Mandell [2] described their LIFE2 code designed to predict fatigue failure time based on wind speed distributions at a prospective site, material fatigue properties and a joint stress-strain distribution for different operational states of the wind turbine. Noda and Flay [3] use a time domain approach in their damage estimation code to assess the differences between low- and high-turbulence intensity sites and conclude that life time may be reduced by a factor of two. Their code is based on a sequential approach where a wind turbine load time series is first generated and damage is inferred in a subsequent step. Mouzakis et al. [4] use a multiple-regression approach to

relate the loading magnitudes with wind speed parameters, concluding that turbulence intensity is the most important parameter in predicting life time for all major wind turbine components. In her doctoral thesis [5], Li uses the VABS methodology [6] in combination with a damage model to optimize the structural properties of a helicopter rotor blade. She first calculates the strain/stress distributions in the blade for a typical helicopter manoeuvre and then performs an offline fatigue damage analysis for the complete aeroelastic time series generated from a multi-body dynamic software package. In case non-acceptable damage occurs, the design is revised and again subjected to a failure analysis, otherwise the design is deemed to be appropriate.

All works previously mentioned, although differing in scope and approach, are based on statistical relationships between load histories and blade damage. Nijssen [7] in his doctoral thesis raises the issue of strength-based life time prediction as opposed to counting methods such as Miner's rule which do not account for potential effects of load ordering. In a large set of experiments he demonstrated the existence of sequence effects on material life time but concluded that the increase in predictive accuracy does not justify the high computational effort required by the strength-based approach.

Since high computational requirement is the main impediment to modeling progressive damage in blades for dynamic and fatigue loads, the exploration of reduced-order approaches capable of modeling damage progression in highly-complex three-dimensional (3D) structures (i.e. wind turbine blades) is a logical step forward. As shown in the previous chapter for the case of damage progression under static loads, thin-walled beam models have great potential for accurately predicting propagation of damage, while requiring only a small fraction (~1%) of the Degrees of Freedom (DOF) required by 3D finite-element shell models to perform a similar task.

In this work a novel integrated platform for the modeling of dynamic damage propagation in complex composite structures (with application to wind turbine blades) based on the earlier work described in Chapter 5 is presented. The model integrates blade dynamics with aeroelasticity and Progressive Failure Analysis (PFA) and is therefore capable of tracking damage in blades under arbitrary wind conditions and operational states, requiring only modest computational resources and execution times. The usefulness

of this model is here demonstrated for a series of critical dynamic wind conditions and operational turbine states, and the spatial propagation of damage is discussed.

6.1. Description of the model

6.1.1. Thin-wall beam (TWB) model with Progressive Failure Analysis (PFA)

The wind turbine blade is modeled as Thin Walled Beam (TWB) Finite Element (FE) model. This allows inclusion of material anisotropy, arbitrary laminate layups and shear deformability, thus able to represent fundamental structural behaviour of more complex 3D shell or solid FE models with reasonably accuracy [8]. Stress/strain fields for individual layers can be recovered based solely on nodal FE displacement solutions, thus allowing PFA at any layer and position of the structure [9]. The TWB model requires the definition of Global and Local coordinate systems. The first is orthogonal Cartesian (x, y, z) with the x axis laying in the rotor plane, y is parallel to the wind direction and the z axis is parallel to the longitudinal axis of the blade. The second coordinate system is the local shell coordinate (n, s, z) as shown in Figure 6.1, wherein the n axis is normal to the middle surface of a plate element, the s axis is tangent to the middle and follow the contour of the section. The (n, s, z) and (x, y, z) coordinate systems are related through an angle of orientation θ (see Figure 6.1). Point p is called the pole axis, defined at the intersection of the beam's cross-section with an arbitrary line running along the radial direction of the beam (parallel to the z axis).

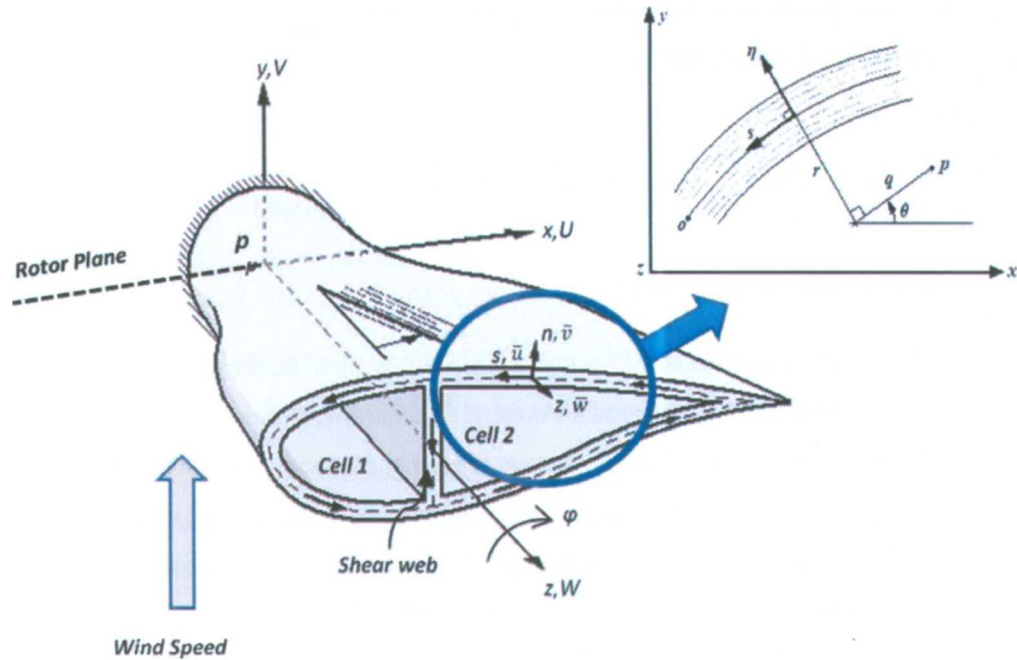


Figure 6.1: Global and mid-surface coordinate system [8]

Figure 6.2 illustrates the resultant single TWB FE element having seven DOFs at each node, defined next: $U_1(z)$, $V_1(z)$ and $W_1(z)$ refer to displacements of node 1 in the x , y and z (along the beam) directions, respectively, where node 1 is a fixed representative point of each cross-section (here called “pole”, see Figure 6.1). Further on, $\psi_y(z)$, $\psi_x(z)$ and $\psi_\omega(z)$ represent angular displacement of node 1 in the x , y and warping directions, respectively, and φ represents elastic angular displacement of the cross-section with respect to the pole (or z) axis. Each element cross-section can be reinforced by one or more shear webs, where the area enclosed by a given closed contour defines a *cell* (see Figure 6.1). The wall thickness t can have an arbitrary circumferential variation (along the contour) as long as it remains thin, but this variation is assumed uniform throughout the element’s length.

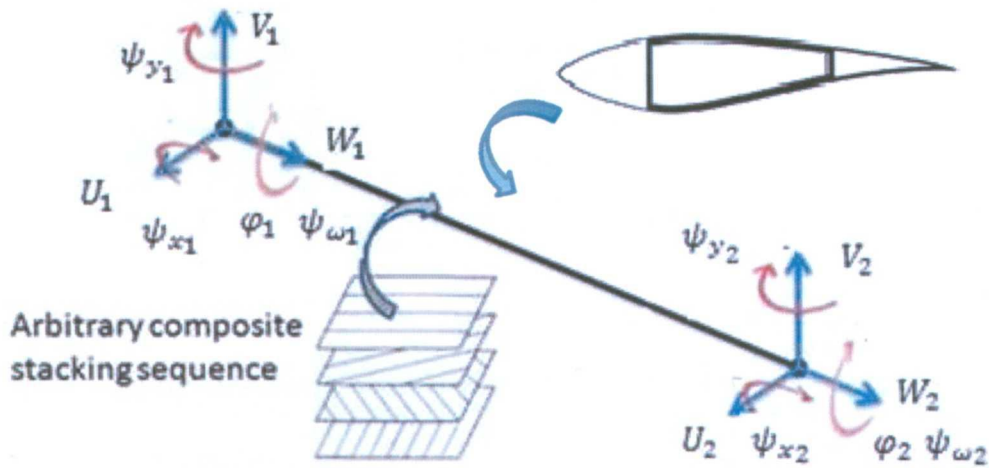


Figure 6.2: A generic 2-node TWB element with 7 DOFs per node.

The Finite Element discretization is obtained via standard displacement-based Lagrangian (shearable) or Hermitian (non-shearable) formulation, expressed as:

$$[M]_{14 \times 14} \{ \ddot{u} \}_{14 \times 1} + [C]_{14 \times 14} \{ \dot{u} \}_{14 \times 1} + [K]_{14 \times 14} \{ u \}_{14 \times 1} = \{ f \}_{14 \times 1} \quad \text{Eq. 6.1}$$

where $[M]$ and $[K]$ are the element's mass and linear stiffness matrices, respectively [9], $\{f\}$ is a vector of nodal external forces, and $\{u\}, \{\dot{u}\}, \{\ddot{u}\}$ represent nodal (linear and angular) accelerations, velocities and displacements. $[C]$ is an experimentally-obtained, proportional hysteretic damping matrix, calculated using a damping factor of 0.08 for a glass fibre/epoxy composite [10]. The vector $\{f\}$ is conformed of all external loads applied on the blade, where the load and displacement vectors have the following structure:

$$\{f\} = \begin{Bmatrix} f_{axial} \\ f_{edge-wise} \\ f_{flap-wise} \\ M_{torsional} \\ M_{edge-wise} \\ M_{flap-wise} \\ M_{bimoment} \end{Bmatrix}; \quad \{u\} = \begin{Bmatrix} W \\ U \\ V \\ \varphi \\ \psi_x \\ \psi_y \\ \psi_\omega \end{Bmatrix} \quad Eq. 6.2$$

Strain and Stress Recovery

From the displacement field the corresponding deformation field is recovered as follows:

$$\begin{aligned} \varepsilon_{zz} &= W'_0 + \psi_y'(x + n \sin \theta) + \psi_x'(y - n \cos \theta) + \psi_\omega'[F(n, s)] \\ \gamma_{sz} &= \gamma_{xz} \cos \theta + \gamma_{yz} \sin \theta + \gamma_\omega[r - n - F_t(s)] + \varphi'[F_t(s) + 2n] \end{aligned} \quad Eq. 6.3$$

As an important remark, only the strains mentioned in Eq. 6.3 are formulated in the TWB. The cross sectional area remains constant for any TWB element. Stress field can be defined based on arbitrary layup, each lamina k obeying a constitutive law as defined next:

$$\begin{Bmatrix} \sigma_{zz} \\ \sigma_{sz} \end{Bmatrix}_k = \begin{bmatrix} \bar{Q}_{11}^* & \bar{Q}_{16}^* \\ \bar{Q}_{16}^* & \bar{Q}_{66}^* \end{bmatrix}^k \begin{Bmatrix} \varepsilon_{zz} \\ \gamma_{sz} \end{Bmatrix}_k \quad Eq. 6.4$$

where coefficients \bar{Q}_{ij}^* are stiffness coefficients initially defined in a material frame, then reduced from a 3D orthotropic law to plane stress conditions, and finally transformed to global (i.e. analysis) coordinates. Once yielded, the FE stress field must be transformed back to material coordinates in order to evaluate failure criteria at each layer:

$$\begin{bmatrix} \sigma_{11} & \sigma_{12} \\ \sigma_{21} & \sigma_{22} \end{bmatrix}^K = [T] \begin{bmatrix} \sigma_z \\ \sigma_{sz} \end{bmatrix}^K [T]^T \quad Eq. 6.5$$

where the 1, 2 directions correspond to along and transversal to the fibre, respectively, and $[T]$ collects the director cosines between the spanwise axis and the fiber of the layer.

Damage Evaluation

Once the stresses are translated to material coordinates it is possible to evaluate layers and locations where damage occurs. For this particular case study, individual ply failure modes are assessed using failure criteria associated with negative and positive limits of the three ply-stress components in the material directions as follows:

$$\begin{aligned}
 S_{11}^c &< \sigma_{11} < S_{11}^t \\
 S_{22}^c &< \sigma_{22} < S_{22}^t \\
 S_{12(-)}^s &< \sigma_{12} < S_{12(+)}^s
 \end{aligned}
 \tag{Eq. 6.6}$$

where σ_L and S_L are the ply stress and ply strength defined by numerical subscripts 11 and 22, corresponding to along- and transverse to the fibre direction, respectively, while subscripts t (+) and c (-) refer to Tensile and Compressive values, respectively. In this way, S_{11}^t represents the ply longitudinal tensile strength, S_{22}^t the matrix-dominated ply transverse tensile strength, also known as matrix splitting, micro-cracking or interfacial bond failure, and S_{12}^s represents shear ply failure mechanisms dominated by matrix shear strength and interfacial conditions. The correspondent compressive values are denoted by the c subscript.

Material Degradation

Material degradation obeys to rules described in [11] as follows: for ply's tensile failure, the young modulus (E) in the failure direction is replaced by 1% of its original value, while for compressive failure the reduction factor is 20%. Same procedure applies for shear stresses, where shear modulus (G) is reduced to 10% of its original value. The degraded properties are then used to carry out the PFA and to update the stiffness matrix K_L of that specific layer.

6.1.2. Aerodynamic loads

Blade Element Momentum (BEM) [12] method is widely used in wind turbine design codes as it offers a fast, simple and accurate approach to calculate aerodynamic forces acting on blades. The basic assumption is that the blade can be divided in the spanwise

direction into a number of independent elements. Based on a momentum balance for an annular control volume of a blade element, the induced velocity is determined. The aerodynamic loads on each element are calculated using the lift, drag and moment coefficient (C_L , C_D and C_M) from experimental wind tunnel test data at defined angles of attack (α) for the profile. The solution provided by BEM is limited by the quality and range of these coefficients (Appendix D). The lift and drag force (L and D) on a blade element of length dz are normal and parallel to the direction of the relative speed V_{rel} respectively (see Figure 6.3), therefore:

$$L = \frac{1}{2} \rho V_{rel}^2 C_L c dz \quad Eq. 6.7$$

$$D = \frac{1}{2} \rho V_{rel}^2 C_D c dz \quad Eq. 6.8$$

where c is the chord of the blade element and ρ is the air density. Finally the momentum (M) around the blade axis is:

$$M = \frac{1}{2} \rho V_{rel}^2 C_M c^2 dz \quad Eq. 6.9$$

The relationship between velocities and forces are described in Figure 6.3, where a is the axial induction factor, β is the pitch angle between the rotor plane and the element chord, ϕ is the sum of β and α , Ω is the rotational rotor speed, z is the spanwise coordinate and U_∞ is the upcoming wind velocity.

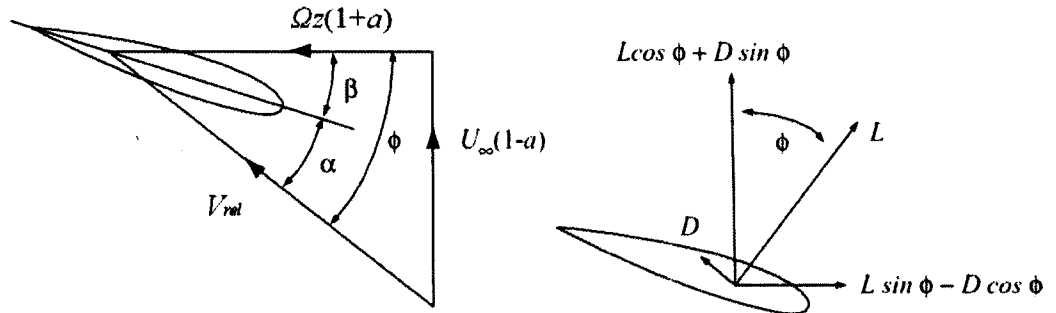


Figure 6.3: Blade element Forces and Velocities [10]

The Drag and Lift forces must be projected to the flap- and edge-wise directions to transform aerodynamic forces to blades's global coordinate system:

$$f_{flap-wise} = L \cos \phi + D \sin \phi \quad \text{Eq. 6.10}$$

$$f_{edge-wise} = -D \cos \phi + L \sin \phi \quad \text{Eq. 6.11}$$

A set of non-linear equations is solved numerically for each blade element, as detailed in [10]. The aerodynamic forces are calculated at 25% of the chord axis, where the load offset introduces a torque which must be accounted for. It is important to mention that the aerodynamic center of each BEM element, where the loads are acting, correspond to a node of the TWB FEM model.

6.1.3. Gravitational and centrifugal loads

Once the mass of each FE element is calculated, it is straightforward to calculate the gravitational and centrifugal loads. The direction of the gravitational load depends only on the azimuth angle (ϑ) of the blade.

$$f_{G-edge-wise} = mg \cos(\vartheta) \quad \text{Eq. 6.12}$$

$$f_{G-axial} = mg \sin(\vartheta) \quad \text{Eq. 6.13}$$

where m is the mass of each TWB FE element, g is the gravitational constant and ϑ defines the angular position of the blade in the rotor plane. The centrifugal force in the axial direction of the blade for a single blade element is expressed as:

$$F_{CF-axial}^e = \int_{z_1}^{z_2} m_A \Omega^2 (R_0 + z) dz \quad \text{Eq. 6.14}$$

where m_A correspond to the mass per unit of length, R_0 is the hub radius and z_1, z_2 are the initial and final position of the element in the spanwise direction. Due to the flexural deformation of the blade (edge and flap wise) the centrifugal force produces a restoring moments in flap and edge wise directions, with a corresponding stiffening effect, which is defined as:

$$M_{CF-edge-wise} = F_{CF-axial} \times U \quad \text{Eq. 6.15}$$

$$M_{CF-flap-wise} = F_{CF-axial} \times V \quad \text{Eq. 6.16}$$

6.1.4. Wind speed time series generation

Wind records are usually found in time periods of several minutes. Since minutes averages are inappropriate for probing the dynamic response of rotor blades, stochastic second-scale time series are here simulated based on a novel algorithm developed in our group [13]. This algorithm is based on a combination of stochastic Fourier series (allowing control of the frequency spectrum) and a gust-control strategy based on the concept of restrained simulation introduced by Bierbooms and Cheng [14]. This technique, which is based on the autocorrelation function of the original (Fourier) stochastic time series allows to generate a signal with the correct average wind speed and standard deviation (hence turbulence intensity) for a given averaging interval, and also reproduces the measured gusts and anti-gust values in the interval, while remaining stochastic in nature.

6.2. Program structure

Main assumptions of the code are listed below:

1. The blades are modeled as TWB FE linear elements and all the assumptions of TWB hold valid.
2. The aerodynamic forces are calculated based on Blade Element Momentum Theory assuming steady state conditions.
3. Only the rotor blades are simulated, thus any other component of the wind turbine is not considered.
4. The rotor plane is always oriented perpendicular to the wind.
5. The wind speed is uniform at any point in the rotor plane to comply with the BEM assumptions.

6. The blade's pitch angle remains constant throughout the analysis.

The main structure of the algorithm is described in Figure 6.4, basically consisting in three modules: static aeroelastic, dynamic aeroelastic and damage. Their interaction and description is provided below.

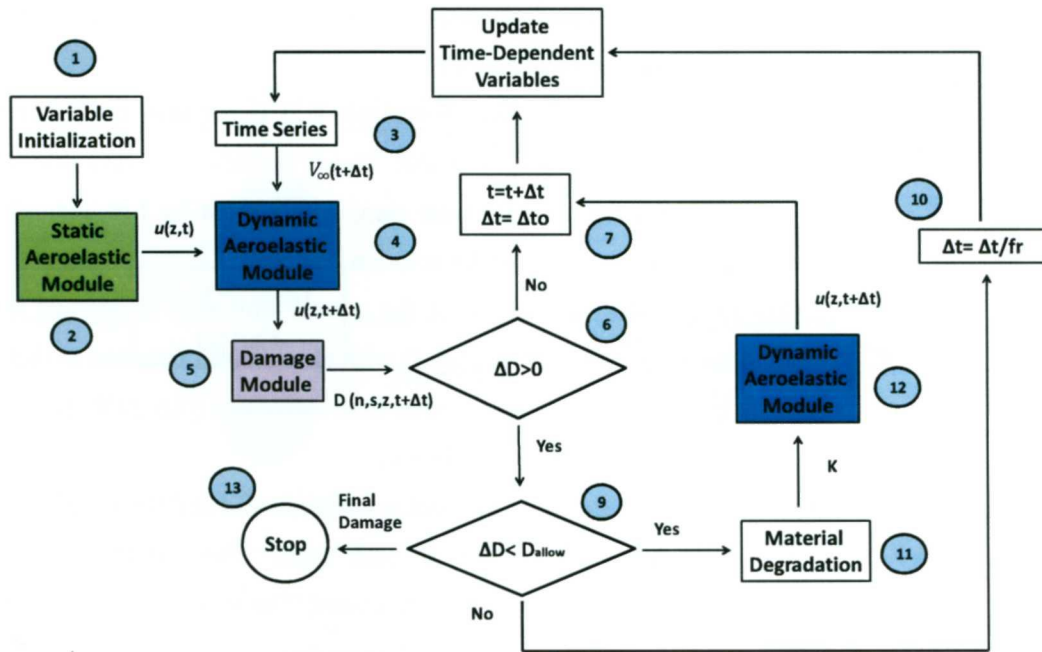


Figure 6.4: Aeroelastic code with damage progression capabilities (flowchart)

1. Main variables are initialized and the simulation time set to $t=0$.
2. The static aeroelastic module determines an initially deformed blade's position $u(z,0)$ for an initial wind velocity $V_\infty(0)$ at time $t=0$.
3. A predefined time-increment $\Delta t = \Delta t_0$ is applied so the Time series provides a new wind velocity value $V_\infty(t+\Delta t)$ to the Aeroelastic Module.
4. The dynamic aeroelastic module determines the updated blade's position $u(z,t+\Delta t)$.
5. The damage module evaluates whether a damage event did or did not occur at all layers. This information is stored in variable D (as for "damage") which records localization and time of any damage event.

6. At early stages of the simulation, stresses are usually low thus damage is unlikely to occur. In such case $\Delta D=0$ (that is, the increase in variable D is zero).
7. If $\Delta D=0$ then the time step is advanced $t=t+\Delta t$ and $\Delta t=\Delta t_0$.
8. All time variables are updated to reflect changes due to a new time-increment Δt . Specifically, the wind velocity series is scanned to provide a new value $V_\infty(t+\Delta t)$ and the simulation restarts at step 3). The sub-cycle 3)-8) is continued until a damage event is detected at step 6).
9. If $\Delta D>0$ (that is, if the increase in variable D is larger than zero) then a damage event has just taken place. Variable D_{allow} defines the allowable amount of damage occurring in a single time step, which must be low enough to avoid compromising the accuracy of the solution.
10. If $\Delta D> D_{allow}$ then the analysis at the current time-step is deemed invalid and calculations are restarted from step 3) with all variables returned to their previous values at time t and applying a smaller time-increment ((i.e. $\Delta t/fr$, $fr>1$). This sub-cycle 3)-9) is repeated until $\Delta D< D_{allow}$.
11. If $\Delta D< D_{allow}$ then the damage event is deemed valid and the simulation proceeds to degrade material properties at each layer where damage has occurred, according to failure criteria already described. The stiffness matrix K of the blade is updated based on degraded material properties.
12. The aeroelastic module is recalled to find the new converged position of the blade $u(z,t+\Delta t)$ and simulation proceeds from step 3).
13. Simulation stops whenever D reaches a maximum amount of damage predefined by the user.

Individual modules are described next.

6.2.1. Static aeroelastic module

The static aeroelastic module attempts to find the initial statically deformed position of the blade $u(z,0)$ due to wind load at time $t=0$, as described in Figure 6.5.

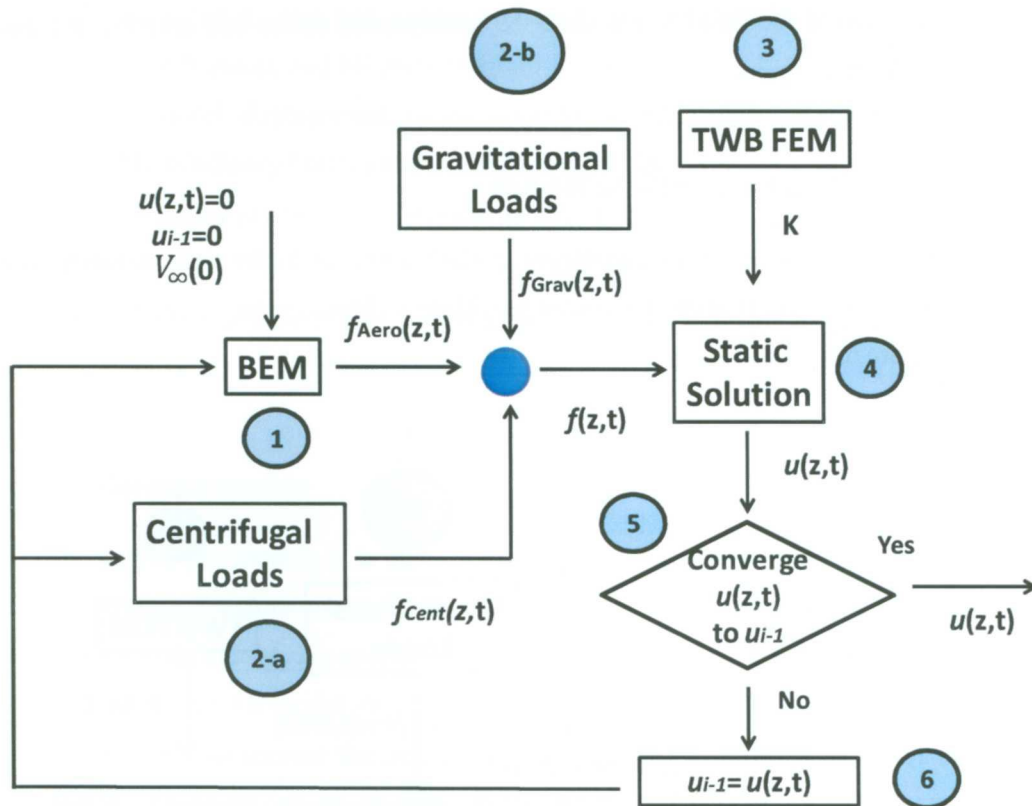


Figure 6.5: Static Aeroelastic Module diagram

1. The nodal displacement vector u and vector u_{i-1} are initialized at time $t=0$ before entering the BEM module. Nodal aerodynamic forces are calculated based on the wind speed $V_{\infty}(0)$ and the initial geometry of the blade $u(z,0)$.
2. The centrifugal and gravitational nodal loads are added to the aerodynamic nodal force vector f .
3. The stiffness matrix K is built based on TWB theory and FE discretization.
4. The nodal displacement vector $u(z,0)$ is calculated.
5. The vector u is compared to u_{i-1} (the nodal displacement of the geometry at a precedent state). If they converge to the same value the cycle ends. Otherwise the vector u_{i-1} is equal to u . The deformed geometry of the blade, which is defined in vector u is

provided to the BEM to calculate the aerodynamic forces and centrifugal loads and the cycle starts again.

6.2.2. Dynamic aeroelastic module

The task of the dynamic aeroelastic module is similar to the static counterpart explained above, that is, finding the converged blade's displacement at time $t+\Delta t$, as shown in Figure 6.6.

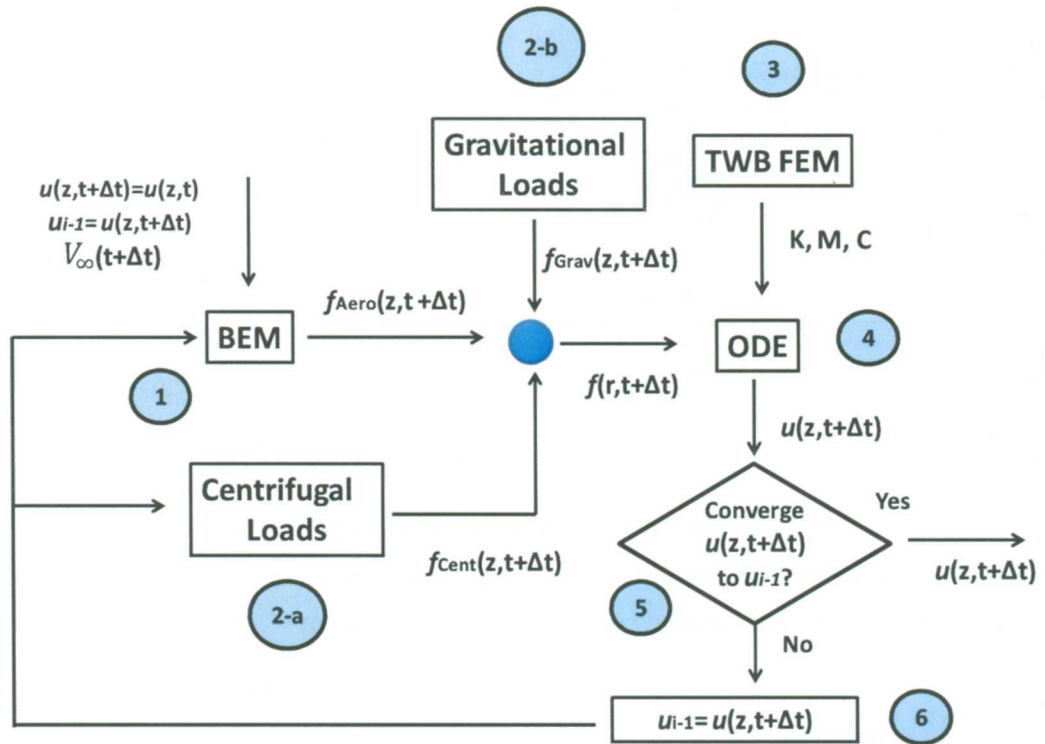


Figure 6.6: Aeroelastic Module flowchart

1. The nodal displacement vectors $u(z,t+\Delta t)$ and u_{i-1} are set equal to $u(z,t)$. The aerodynamic nodal forces at time $t+\Delta t$ are calculated via BEM based on $u(z,t+\Delta t)$ and $V_\infty(t+\Delta t)$.
2. The centrifugal and gravitational nodal loads are added to the aerodynamic nodal force vector at time $t+\Delta t$.

3. The stiffness, mass and damping matrix K , M and C of the blade are built based on TWB theory and FE discretization.
4. The nodal displacement vector $u(z,t+\Delta t)$ is calculated via standard MATLAB ODE (Ordinary Differential Equations) algorithms.
5. The vector $u(z,t+\Delta t)$ is compared to u_{i-1} . If they converge to the same value the cycle ends. Otherwise, u_{i-1} is equated to $u(z,t+\Delta t)$. The deformed blade's geometry is provided to the BEM and Centrifugal Loads module and the cycle restarts.

6.2.3. Damage module

The task of this module is to identify the presence of damage, localize and characterize those layers and regions where damage occurs due to load conditions at $u(z,t+\Delta t)$. The sub-steps of this module are exemplified in Figure 6.7.

1. Based on FE nodal displacement results, the TWB shell capabilities make it possible to recover the strain field at any layer and position of the blade, which can be translated to global longitudinal and shear stresses (σ_{zz} , σ_{sz}) via the constitutive law Eq. 6.4
2. This stress field must be transformed to material framework in order to assess damage in a given layer. Stresses σ_{11} , σ_{22} and σ_{12} represent the stress in the direction-of, perpendicular-to, and in-plane of the fibres respectively.
3. The material stresses are used to evaluate failure criteria to identify type, localization and amount of damage in affected areas. This information is stored in variable D .

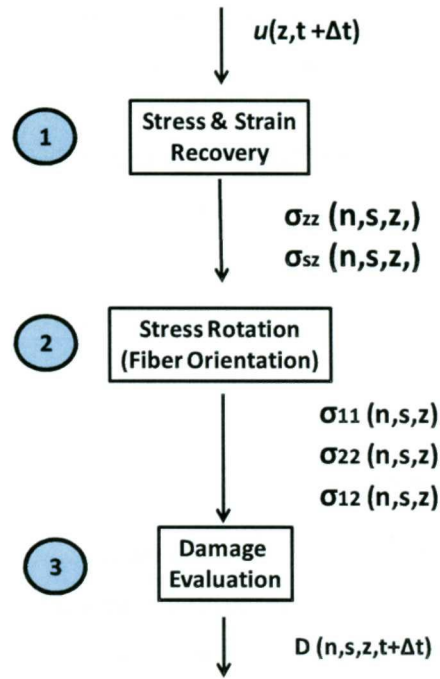


Figure 6.7: Damage Module Diagram

6.3. Description of the case study

Three different cases are simulated to demonstrate the damage detection and progression during the aeroelastic simulation. The cases selected in this study correspond to conditions more critical to those used to design wind turbine blades. The purpose of this work is just to describe how the damage is progressing during the time of the simulation.

6.3.1. Case 1: Parked rotor facing a class 5 hurricane

The first case to simulate assumes a wind turbine located in a coastal area. A hurricane category 5 strike the rotor, which is assumed to be parked and directly facing the wind. In order to assume a more severe condition the blade is exposing the major part of its area to the wind flow. The simulation only covers the 2 most critical minutes of the hurricane which has a gust speed of 97 m/s and an average of 74 m/s.

6.3.2. Case 2: Wind speed ramp at constant rotor shaft frequency

The nominal angular speed of the rotor is 55 RPM according with Sandia, the designers of the wind turbine [15]. This case supposes that the rotor keep constant its angular velocity while a wind gust hits it. As in the previous case, the plane of the rotor is facing the upcoming wind. The velocity of the wind is modelled as a ramp with a positive slope of 2 m/s².

6.3.3. Case 3: Constant wind speed and loss of load

The last case simulates a failure on the protection system of the turbine. The electric generator applies any torque and the brake system is not working. The rotor is free to accelerate in its angular speed. The angular acceleration of the rotor is proportional to the aerodynamic torque and inversely proportional to the inertia moment of the blades. The wind excites the wind turbine with a constant velocity, for this case 25 m/s.

6.3.4. Blade description

The wind turbine blade used in this work to exemplify the damage progression in a blade is based on the prototype NPS-100 from Sandia National Laboratories (SNL) described in Chapter 4. According to the Sandia report, the NPS-100 is a derivative of the ERS-100, a 9.2 meter blade originally developed by SNL and TPI Composites, intended for the 100 kW retrofit market. It was designed around a number of airfoils of variable chord, with a material layup conformed of glass fibre composites, balsa wood and gel coating. In Chapter 4, this blade was chosen as a case study to validate the static and dynamic behaviour predicted by a TWB model against an industry-standard 3D shell model built in a commercial software tool. Figure 6.8 illustrates the external geometry of the blade and the layup distribution. The color code represents the areas which share the same material layup. Detailed information of the geometry and material layup it is found in Chapter 4. Table 6.1 summarizes the material and their properties used to construct the blade. The aforementioned blade was used to construct a TWB FEM model using 120 shearable elements.

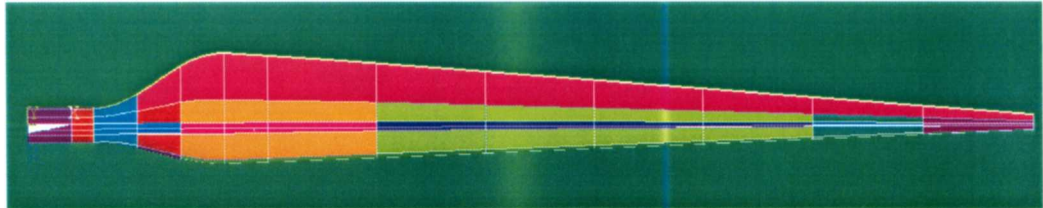


Figure 6.8: Blade geometry and materials layup

Table 6.1: Material elastic and strength properties

	Material Name				
	C520 (textile glass fibre)	C260 (textile glass fibre)	¾ mat (random glass fibre)	Gel coat	Balsa wood
E11 (MPa)	48,200	43,000	7,580	3,400	2,070
E22 (MPa)	11,700	8,900	7,580	3,400	2,070
G12 (MPa)	6,480	4,500	6,480	1,320	848
v12	0.30	0.27	0.30	0.30	0.22
Rho (g/cm3)	1.874	1.874	1.670	1.23	0.144
S₁₁^t (MPa)	1,000	892	132	71	7
S₁₁^c (MPa)	788	703	194	104	5.40
S₂₂^t (MPa)	51	39	132	71	7
S₂₂^c (MPa)	168	128	94	104	5.4
S₁₂^s (MPa)	112	78	112	50	1.6

It is important to remark that the load cases reproduced in this work are not those which Sandia used to design their 9 meter wind turbine blades [15]. The simulations presented here assume extremely critical and almost unrealistic conditions. The blade used here is already designed by Sandia to satisfy the design requirements described in [15]. For these reason extremely conditions are assumed in order to illustrate the damage progression in an aeroelastic simulation.

6.4. Results and discussion

The general system Eq. 6.1 can be solved via standard algorithms dealing with Ordinary Differential Equations (ODE). In this work, the Matlab ode15 function, recommended for stiff problems, yielded good results. Explicit methods for numerical integration are only conditionally stable and they have to use very small time step [16]. According with [16] if Δt exceeds a critical value, computed displacement and velocity errors grow without outbound. Based on the FRF of the blade illustrated in Chapter 4, the time step used for this work is 0.005 seconds was proven successful.

6.4.1. Case 1: Parked rotor facing class 5 hurricane

A hurricane category five with a maximum wind speed of 97 m/s and wind speed average of 74 m/s is acting against a wind turbine. The rotor is assumed to be in parked condition and the chord of the blade is perpendicular to the wind direction. The drag force is the main load acting over the blade. The solid line in Figure 6.9 represents the time series of the wind speed. The simulation only covers the most critical 2 minutes of the hurricane event. The circles present in the plot indicate the time step where a damage event occurs on the blade. The red line means the percentage of volume which is already damaged. After the two minutes of the hurricane 0.7 % of the blade volume has reached a failure criterion.

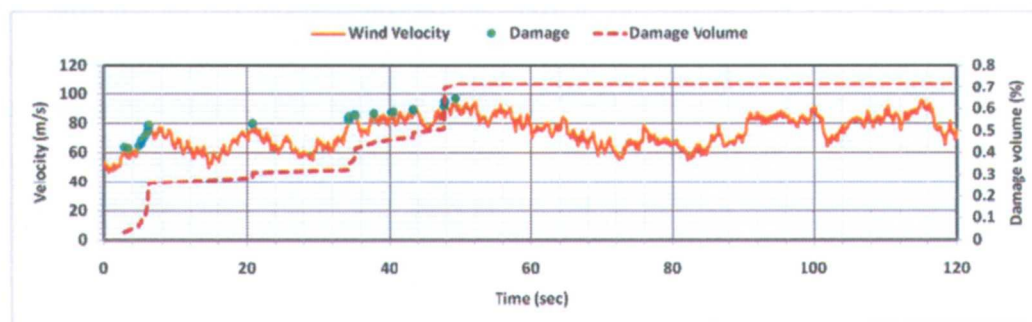


Figure 6.9: Wind speed time series and damage volume

The flapwise displacement of the tip blade during the hurricane it is shown in Figure 6.10. The circles over the graphic represent damages event. According with Figure 6.10 new damage occurs only when the displacement reach higher or very similar to the previous highest value. This damage progression behavior occurs because of the type of the damage model used in this work. Damage occurs once the stress reaches a threshold value. At that moment the material properties are degraded. The model doesn't accumulate the degradation produced by lower loads of the threshold value.

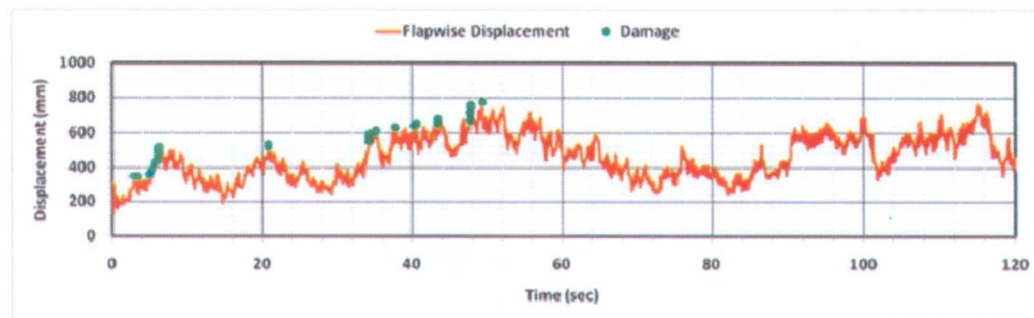


Figure 6.10: Flapwise displacement

The damage occurs only in layer number 6 which correspond to the Balsa material. Balsa is the main component in the material layup for the trailing edge of the balsa (See appendix C). Figure 6.11 shows the progressive failure analysis for the balsa. The cyan color represents the healthy areas of the blade. In the color scale the darker color corresponds the areas where the damage occurs first. The damage starts in the trailing edge of the blade and progress in the spanwise direction, typical of a structure in flexion. The failed area is located on the compressed side of the blade and the failure criteria reached is S11C.

PFA Layer 6 (Balsa)

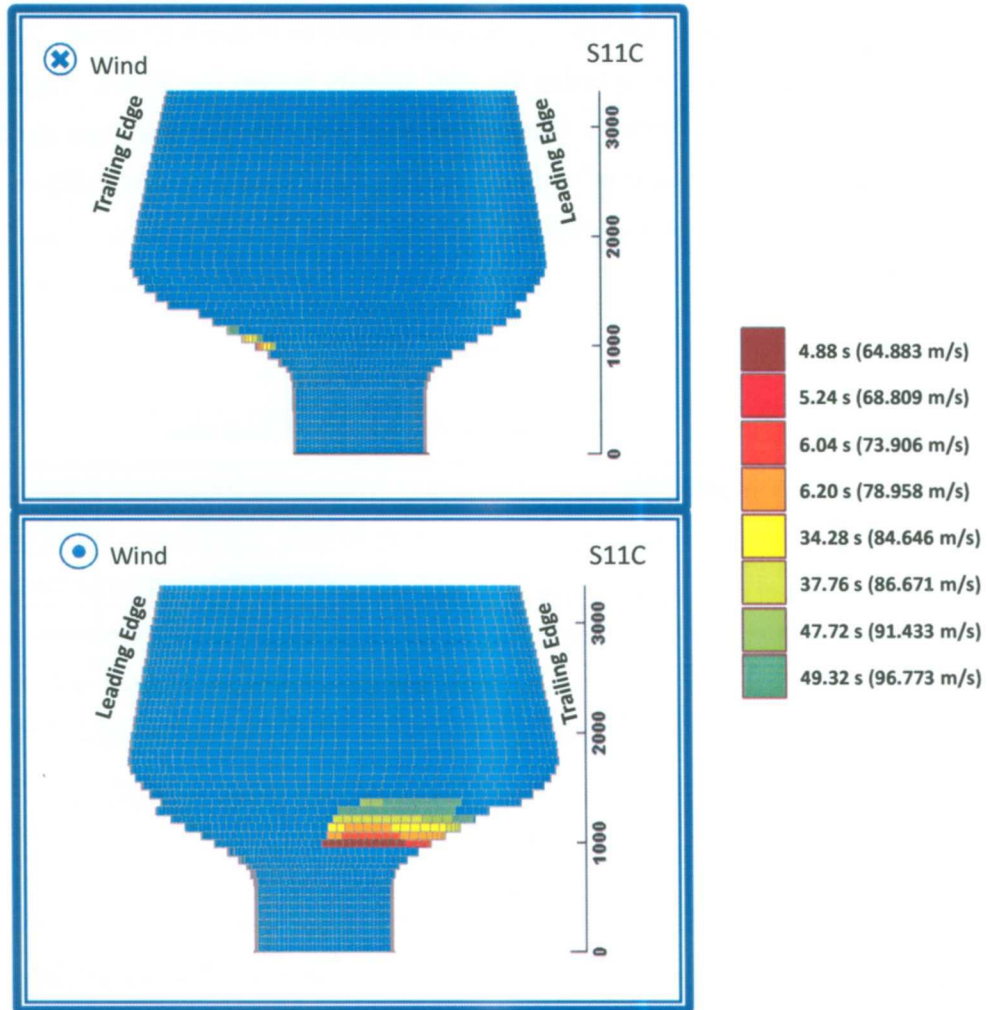


Figure 6.11: Progressive Failure Analysis of layer 6 (Balsa)

6.4.2. Case2: Wind speed ramp at constant rotor shaft frequency

In this case the angular speed of the rotor is assumed to remain constant at 55 RPM. The wind speed increase constantly 2 m/s each second as Figure 6.12 shows. The damage in the blade starts to appear before the wind velocity reaches the 60 m/s. The circles on the plot represent the instants when some new areas in the blade are damaged. The accumulated percentage of volume damage (dashed line in Figure 6.12) once the wind velocity reaches 100 m/s is 0.8%.

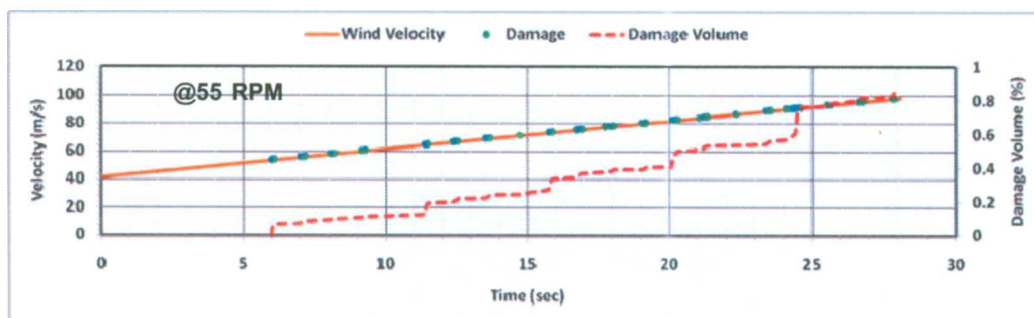


Figure 6.12: Wind speed time series and damage volume

The tip blade displacement doesn't follow linear increment as the velocity does. In Figure 6.13 the slope of the solid line increases over time. It is also possible to identify a cycling signal component corresponding to the gravitational loads on the flapwise direction. The dashed line represents the cosine of the azimuth angular position of the blade. This line helps to identify that the damage occurs when the blade is parallel to the ground with the trailing edge pointing down. In this position the gravitational load is flexing the blade in the edgewise direction. This effect is summed to the flexion in the flapwise direction causing most of the damage.

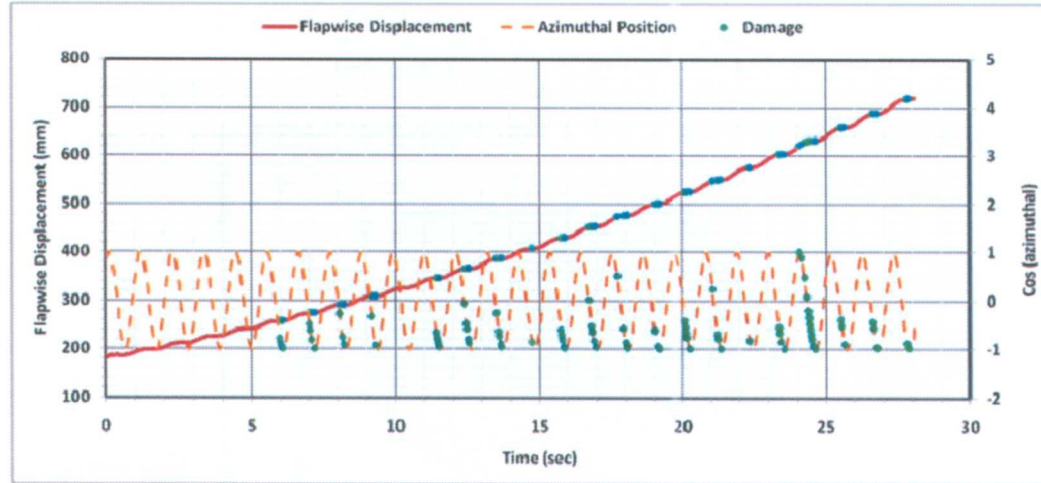


Figure 6.13: Flapwise displacement and azimuth position of the blade

The failure mechanism is similar to the previous example. The main load acting on the blade is the aerodynamic drag in the flapwise direction combined with the gravitational load acting in the edgewise direction. The layer where the damage is present is number 6 and corresponds to the Balsa. Figure 6.14 shows the progressive failure analysis for the balsa. The damage starts in the trailing edge zone which corresponds to the compressive side for flapwise and edgewise. The color scale has the same meaning as the previous figure. The progression of the damage moves in the spanwise direction and the failure criteria reached is S11C.

PFA Layer 6 (Balsa)

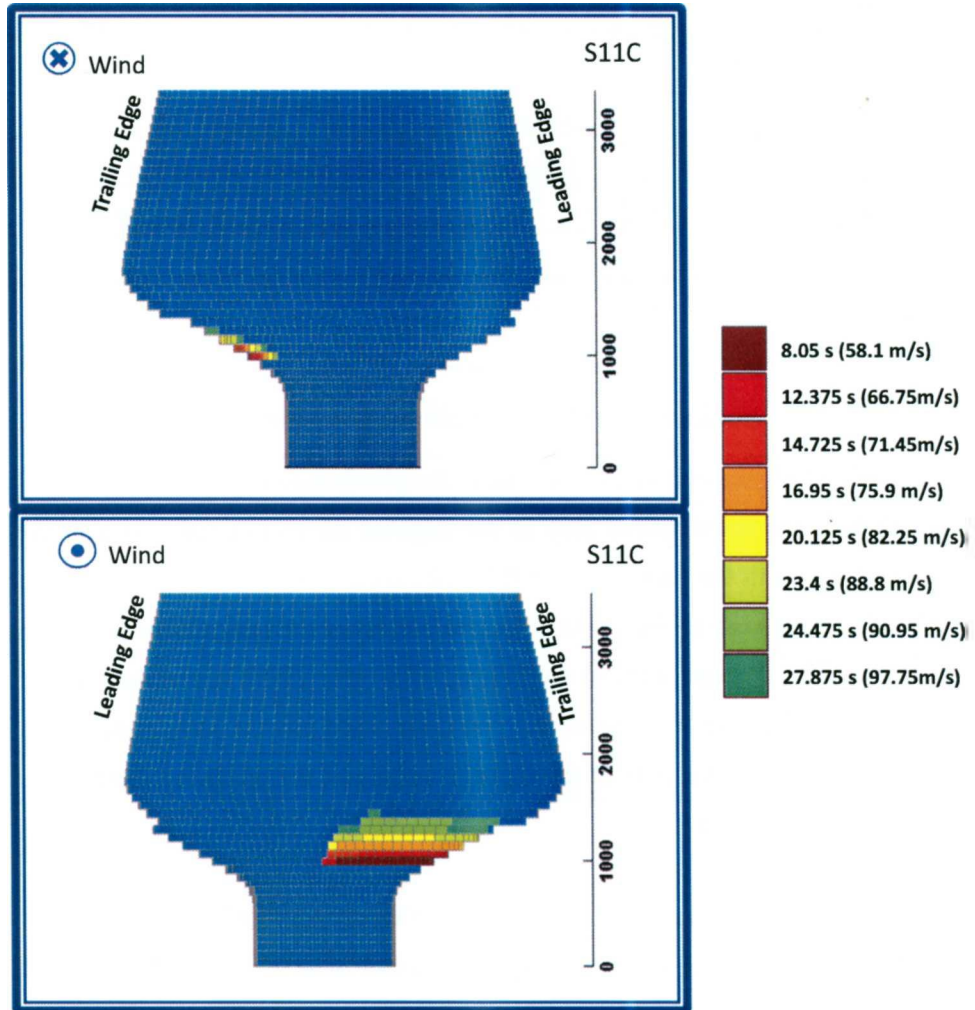


Figure 6.14: Progressive Failure Analysis of layer 6 (Balsa)

6.4.3. Case 3: Constant Wind Speed

In this last case the rotor is free to accelerate in its angular direction. The wind speed (25 m/s) facing the rotor is constant during all the simulation time. The angular acceleration it is produced by the torque generated by the wind. This is the case when the electric generator is shut down or has failed. Figure 6.15 shows that the angular speed increases linearly over the time. The damage appears suddenly and progress continuously in a catastrophic way. The amount of damage is again described by the dashed line. In less than a second 0.7 % of the blade is already damaged.

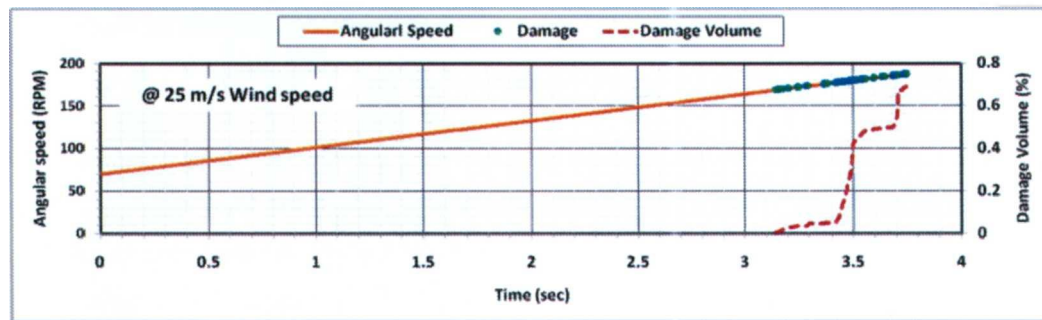


Figure 6.15: Wind speed time series and damage volume

The restoring moments stiffening the blade and due to the centrifugal loads considered in equations Eq. 6.15 and Eq. 6.16 are clearly observed in Figure 6.16. The Flapwise (solid line) displacement reaches a maximum value of 330 mm and then a gradual descent is observed while the angular rotation increases. In the other hand the spanwise displacement (dashed line) presents a parabolic behavior. The damage events are marked with circles and they appear grouped at the end of the simulation.

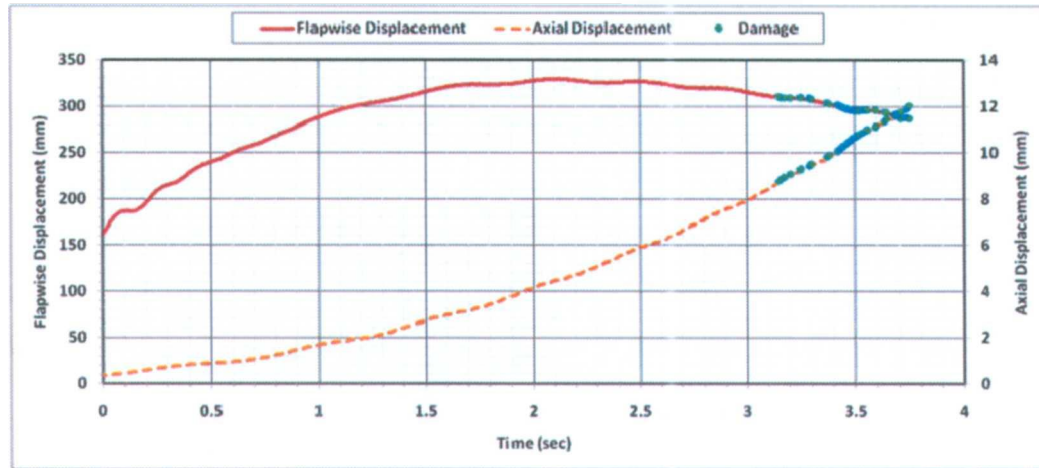


Figure 6.16: Flapwise and Spanwise displacement of the blade

The damage occurs again in layer 6 (Balsa) which represents the main volume of the trailing edge of the blade. Balsa fails mainly due to the tension (S11T) created by the spanwise displacement and the aerodynamical flexion. A small amount of shear damage (S12S) is present on leading edge side of tip blade. Due to the high speed rotation, the aerodynamical loads on the tip elements produces some damage which doesn't occurs in conditions described before. Damage produced by the shear loads is also evident in the proximity of the blade root. Figure 6.17 shows the location of the damage on the blade and the type of failure criteria which applies.

PFA Layer 6 (Balsa)

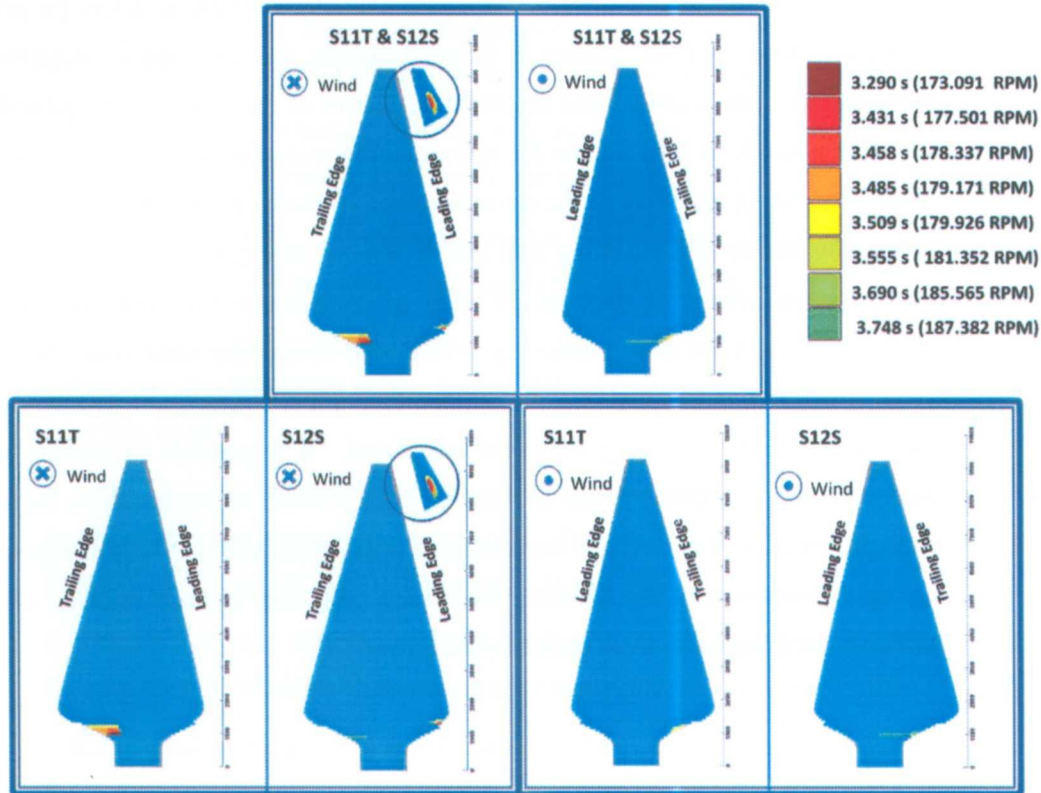


Figure 6.17: Progressive Failure Analysis of layer 6 (Balsa)

6.5. Conclusion

In the present chapter an implementation was described of a platform for modeling the progression of damage in complex structures made of composite materials during dynamic aeroelastic simulations. The structural behavior of the blade was modeled as a thin-walled beam (TWB), a 1D FE model capable of capturing the most essential characteristics of slender structures such as rotor blades. TWB has the potential of recovering the strains and stresses for all layers at any position of the blade. In this way it is possible to integrate failure models which allow analyzing the propagation of damage in the structure.

Due to its computational efficiency it is possible to integrate the TWB in a dynamic aeroelastic code describing the fluid-structure interaction. At any time step of the simulation, the integrity of the blade layers is evaluated in order to detect the presence of damage. Once a layer reaches a failure criterion, the mechanical properties of the damaged area are degraded and the stiffness matrix of the structure is updated. In this way it is possible to fully couple the interaction between the aerodynamics loads and the blade, integrating the effect of the damage caused by them on the structure. This coupling potentially allows implementing and testing control strategies during the simulation to avoid the occurrence of damage. In order to demonstrate the feasibility of the code presented here, three cases assuming severe load conditions were simulated using the blade described in Chapter 4. The simulation results illustrate the progression of the damage on the blade during the events simulated. It is possible to identify when and where the failure criteria are reached and the type of load which creates the damage. The code presented here will reduce the predesign times by integrating the blade geometry and lay up definition with the dynamic aeroelastic code and damage tracking capabilities, avoiding the designer to work each module separately.

References

- 1 PS Veers, TD Ashwill, HJ Sutherland, DL Laird, DW Lobitz, DA Griffin, JF Mandell, WD Musial, K Jackson, M Zuteck, A Miravete, SW Tsai, JL Richmond. Trends in the Design, Manufacture and Evaluation of Wind Turbine Blades. *Wind Energy*. 2003; 6:245–259
- 2 HJ Sutherland, JF Mandell. Application of the u.s. high cycle fatigue data base to wind turbine blade lifetime predictions. *Proceeding of Energy Week 1996, ASME*
- 3 M Noda, RGJ Flay. A simulation model for wind turbine blade fatigue loads. *Journal of Wind Engineering and Industrial Aerodynamics* 83 (1999) 527-540
- 4 F Mouzakis, E Morfiadakis, P Dellaportas. Fatigue loading parameter identification of a wind turbine operating in complex terrain. *Journal of Wind Engineering and Industrial Aerodynamics* 82 (1999) 69-88.
- 5 Li L. Structural design of composite rotor blades with consideration of manufacturability, durability and manufacturing uncertainties. Doctoral Thesis in School of Aerospace Engineering. Georgia Institute of Technology. August 2008
- 6 Volovoi V, Hodges D.H, Cesnik C.E.S, Popescu B. Assesment of beam modelling methods for rotor blade applications. *Mathematical and Computer Modelling* 2001; 33: 1099-1112
- 7 R.P.L. Nijssen. Fatigue Life Prediction and Strength Degradation of Wind Turbine Rotor Blade Composites. Doctoral Thesis in Design and Production of Composite Structures. Delft University of Technology 2006
- 8 Cardenas D, Elizalde H, Marzocca P, Probst O. Numerical validation of a finite element thin-walled beam model of a composite wind turbine blade. *Wind Energy* 2011. DOI: 10.1002/we.462.
- 9 Lee J, Vo T., Flexural–torsional behavior of thin walled composite box beams using shear-deformable beam theory. *Engineering Structures* 2008; 30(7): 1958–1968.
- 10 Burton T, Sharpe D, Jenkins N, Bossanvi E. *Wind Energy Handbook*. Wiley 2001
- 11 <http://www.ascgenoa.com/main/>
- 12 H. Madsen, R. Mikkelsen, S. Øye, C. Bak, J. Johansen. A Detailed investigation of the Blade Element Momentum (BEM) model based on analytical and numerical results and proposal for modifications of the BEM model. *Journal of Physics: Conference Series* 75 (2007) 012016

- 13 Amezcua, J.; Muñoz, R.; Probst, O. Reconstruction of gusty wind speed signals from data logger time series, submitted to *J. Wind Eng. Indust. Aerodyn* (October 2008).
- 14 W. Bierbooms, Po-Wen Cheng. Stochastic gust model for design calculations of wind turbines. *Journal of Wind Engineering and Industrial Aerodynamics* 90 (2002) 1237–1251.
- 15 D Berry, T Ashwill. Design of 9-Meter Carbon-Fiberglass Prototype Blades: CX-100 and TX-100. Sandia report: SAND2007-0201.
- 16 Ahlstrom A. Aeroelastic simulation of wind turbine dynamics. Doctoral thesis in Structural Mechanics, KTH, Sweden, 2005

Chapter 7.

Conclusions and further work

7.1. Conclusions and summary of contributions

An integrated computational platform was developed capable of modeling the progression of damage on long slender composite structures such as helicopter and wind turbine blades by dynamically integrating fluid-structure interaction and damage progression. The code has the capability of dynamically updating the structural properties of the blade in response to progressively occurring damage which in turn is a function of static and dynamic loads caused by fluid-structure interaction. This procedure avoids the limitations posed by the conventional approach where structural loads are first calculated based on time series or distributions and damage evaluation is conducted as an add-on step based on the load histories.

As shown in Chapter 3 and 4 wind turbine blades can be modeled as thin-walled beams (TWB), a class of 1D models capturing their main characteristics, albeit at the expense of some restricting assumptions and a possible loss of accuracy under certain conditions. For practical purposes, however, these restrictions are often not substantial as demonstrated in Chapter 4 where a validation of the capabilities of the TWB approach of reproducing the static and dynamic behavior of a complex blade against a 3D shell model created in a commercial software package was conducted. Besides this ability of TWB, the model offers the possibility of recovering the strains and stresses for all the layers at any position of the structure. In this way it is possible to implement failure criteria in order to model the progression of damage in the blade caused by the loads acting on it. For the purpose of validation of the combined Progressive Failure Analysis (PFA)-TWB model, its predictions were compared against those obtained with GENOA, a commercial finite element based tool designed for the composite failure analysis of complex structures. In

Chapter 5 the two models were compared demonstrating that a reduced order model such as the TWB can accurately predict the progression of the damage calculated by a higher-order model such as the shell model used in GENOA. The use of the PFA-TWB is limited to slender structures which do not violate the main assumptions of the model, such as the non-deformation of the cross-sectional area. Finally, Chapter 6 integrates the PFA-TWB model with dynamic aeroelastic simulation capabilities. Three different cases were simulated in order to demonstrate the capabilities of this approach.

The main contribution of the present work to the state-of-the-art of aeroelastic and damage progression modelling is the development of a computational platform which allows an integration of the different modules used independently in the current design practice of rotor blades. In this way, highly significant decreased execution times for the assessment of damage are possible, providing the designer with a useful tool at all design stages but certainly at pre-design, where a rapid turnover rather than the highest accuracy is required. Additionally, the restrictions as to accuracy imposed by the assumptions of the TWB model may be partly compensated by an increase in modelling accuracy, since the modification of the structural properties is provided as the damage occurs, as opposed to off-line assessments where the same structural properties are used for a whole load history.

7.2. Future Outlook

The proposed methodology open significant opportunities when it comes to perform fully coupled fluid-structure interaction simulations for advanced composite flexible blades considering the evolution of damage as it propagate throughout the structure. Of course, improvements to the methodology are possible in several venues, such as:

- The validation of the PFA-TWB against experimental results. Static and dynamic cases have to be considered. The use of guided waves can help to identify the layers and the area where damage occurs during experiments. Although this requires a dedicated and accurate experimental campaign, this effort can produce validation data that can be used to compare against the predictions of the PFA-TWB model.

- A relatively straightforward extension of the present work would be the consideration of failure criteria with combined multi-axial stresses and validate their damage progression against higher order models.
- The TWB-PFA has to be extended to considered (multi-axial) fatigue. The mechanical properties of the composites layers have to be updated due to the damage caused by cyclic loads.
- One further line of research would be to release one of the restraining assumptions of the TWB approach by allowing the cross-sectional area of the blade to deform in its plane in order to calculate the hoop strains and stress which can have some effect when combined failure criteria are implemented. Without this assumption it is possible to complete the stress tensor of the reduced order model allowing to apply the same failure models created for shell elements. The use of modal information could be an option to relate the TWB displacement with the deformation of the cross-sectional area.
- Non-linear geometrical effect and un-uniformity of the aerodynamic loads acting on the structure can also be taken into account as to improve accuracy of the model by taking into account large deformation and blade dynamic stall conditions. Within the current approach, which only considers small strains, is limited to initial damage stages where large deformations don't occurs.
- As the current work was limited to (rotating) blades alone, and did not consider structural coupling to other elements, such as a drive train and a wind turbine tower. These effects could also be included in further models.
- The current explicit numerical integration scheme used to solve the equation motion has many inconvenient. The method is conditionally stable and requires very small time steps to avoid errors. Future work will look into substituting it by an implicit method which can guarantee the equilibrium of the system after each iteration.
- The effects of material uncertainty can be included in the model. Composite materials present a scatter of the measured properties and it is important to consider it to predict the reliability of the structure.

Appendix A

$[E_{ij}] =$

$$\begin{aligned}
 E_{11} &= \int_s A_{11} ds & E_{15} &= \int_s \left(A_{16} \frac{F_t}{2} + B_{16} \right) ds \\
 E_{12} &= \int_s (A_{11}x + B_{11} \sin \theta) ds & E_{16} &= \int_s (A_{16} \cos \theta) ds \\
 E_{13} &= \int_s (A_{11}y - B_{11} \cos \theta) ds & E_{17} &= \int_s (A_{16} \sin \theta) ds \\
 E_{14} &= \int_s (A_{11}\omega_1 - B_{11}[q + F_2]) ds & E_{18} &= \int_s \left(A_{16} \left[r - \frac{F_t}{2} \right] \right) ds \\
 E_{22} &= \int_s (A_{11}x^2 + 2B_{11}x \sin \theta + D_{11} \sin^2 \theta) ds & E_{27} &= \int_s (A_{16}x + B_{16} \sin \theta) \sin \theta ds \\
 E_{26} &= \int_s (A_{16}x + B_{16} \sin \theta) \cos \theta ds & E_{28} &= \int_s (A_{16}x + B_{16} \sin \theta) \left(r - \frac{F_t}{2} \right) ds \\
 E_{36} &= \int_s (A_{16}y - B_{16} \cos \theta) \cos \theta ds & E_{37} &= \int_s (A_{16}y - B_{16} \cos \theta) \sin \theta ds \\
 E_{38} &= \int_s (A_{16}y - B_{16} \cos \theta) \left(r - \frac{F_t}{2} \right) ds & E_{46} &= \int_s (A_{16}\omega_1 - B_{16}[q + F_2]) \cos \theta ds \\
 E_{48} &= \int_s (A_{16}\omega_1 - B_{16}[q + F_2]) \left(r - \frac{F_t}{2} \right) ds & E_{47} &= \int_s (A_{16}\omega_1 - B_{16}[q + F_2]) \sin \theta ds \\
 E_{66} &= \int_s (A_{66} \cos^2 \theta + A_{55} \sin^2 \theta) ds & E_{67} &= \int_s (A_{66} - A_{55}) \sin \theta \cos \theta ds \\
 E_{88} &= \int_s \left[A_{66} \left(r - \frac{F_t}{2} \right)^2 + A_{55} \left(q + \frac{F_2}{2} \right)^2 \right] ds & E_{77} &= \int_s (A_{66} \sin^2 \theta + A_{55} \cos^2 \theta) ds
 \end{aligned}$$

$$E_{23} = \int_s (A_{11}xy + B_{11}(y \sin \theta - x \cos \theta) - D_{11} \sin \theta \cos \theta) ds$$

$$E_{24} = \int_s (A_{11}x\omega_1 + B_{11}(\omega_1 \sin \theta - x[q + F_2]) - D_{11} \sin \theta [q + F_2]) ds$$

$$E_{25} = \int_s \left(A_{16}x \frac{F_t}{2} + B_{16} \left(x + \frac{F_t \sin \theta}{2} \right) + D_{16} \sin \theta \right) ds$$

$$E_{33} = \int_s (A_{11}y^2 - 2B_{11}y \cos \theta + D_{11} \cos^2 \theta) ds$$

$$E_{34} = \int_s (A_{11}y\omega_1 - B_{11}[y(q + F_2) + \omega_1 \cos \theta] + D_{11} \cos \theta [q + F_2]) ds$$

$$E_{35} = \int_s \left(A_{16} \frac{F_t}{2} y + B_{16} \left(y - \frac{F_t \cos \theta}{2} \right) - D_{16} \cos \theta \right) ds$$

$$E_{44} = \int_s (A_{11}\omega_1^2 - 2B_{11}\omega_1(q + F_2) + D_{11}(q + F_2)^2) ds$$

$$E_{45} = \int_s \left(A_{16} \frac{\omega_1 F_t}{2} + B_{16} \left(\omega_1 - \left[\frac{q + F_2}{2} \right] F_t \right) - D_{16} [q + F_2] \right) ds$$

$$E_{55} = \int_s \left(A_{66} \frac{F_t^2}{4} + B_{66} F_t + D_{66} + A_{55} \frac{F_2^2}{4} \right) ds$$

$$E_{56} = \int_s \left(A_{66} \cos \theta \frac{F_t}{2} + B_{66} \cos \theta + A_{55} \sin \theta \frac{F_2}{2} \right) ds$$

$$E_{57} = \int_s \left(A_{66} \sin \theta \frac{F_t}{2} + B_{66} \sin \theta - A_{55} \cos \theta \frac{F_2}{2} \right) ds$$

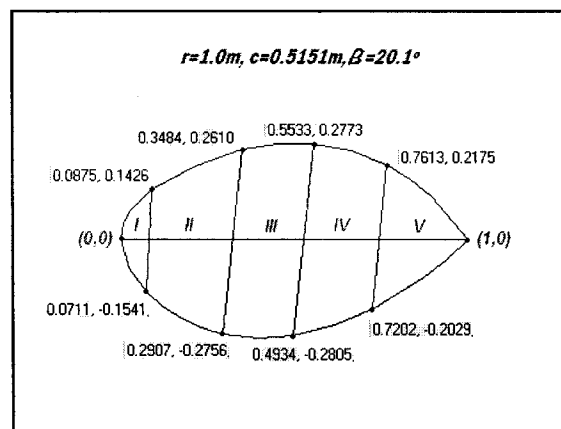
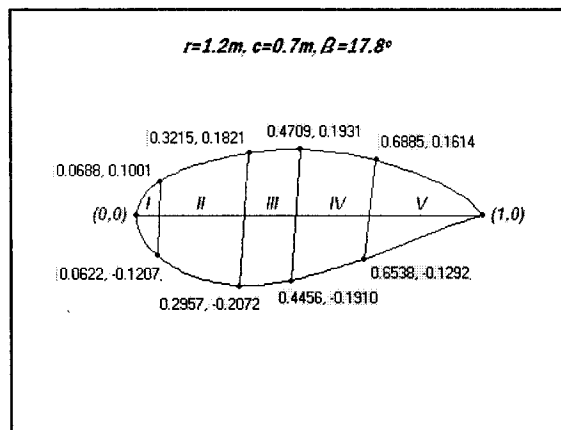
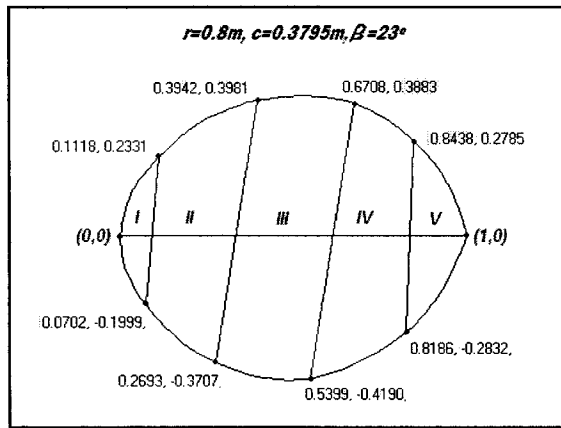
$$E_{58} = \int_s \left[\left(A_{66} \frac{F_t}{2} + B_{66} \right) \left(r - \frac{F_t}{2} \right) - A_{55} \frac{F_2}{2} \left(q + \frac{F_2}{2} \right) \right] ds$$

$$E_{68} = \int_s \left[A_{66} \cos \theta \left(r - \frac{F_t}{2} \right) - A_{55} \sin \theta \left(q + \frac{F_2}{2} \right) \right] ds$$

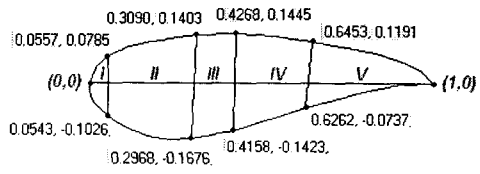
$$E_{78} = \int_s \left[A_{66} \sin \theta \left(r - \frac{F_t}{2} \right) + A_{55} \cos \theta \left(q + \frac{F_2}{2} \right) \right] ds$$

Appendix B

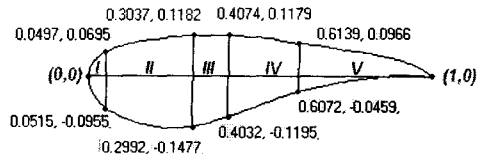
External dimensions of transitional airfoils (relative to Figure 4.1 and Figure 4.4)



$r=1.4m, c=0.8816m, \beta=16.2^\circ$



$r=1.6m, c=1.0m, \beta=15^\circ$



Appendix C

Layup Code (Relative to Figure 4.1 and Figure 4.6)

LAYUP CODES 1,2,3,5,8,9,11,13,15			
Layer	Material	Angle (°)	Thickness (mm)
1	D	0	0.130
2	C	0	0.372
3	B	45	0.296
4	C	0	0.296
5	B	-45	0.296
6	B	45	0.186
7	C	0	0.186
8	B	-45	0.186
9	A	0	t15
10	B	45	0.186
11	C	0	0.186
12	B	-45	0.186
13	B	45	0.296
14	C	0	0.296
15	B	-45	0.296

LAYUP CODES 6,10,12,14			
Layer	Material	Angle (°)	Thickness (mm)
1	D	0	0.13
2	C	0	0.372
3	B	45	0.296
4	C	0	0.296
5	B	-45	0.296
6	B	45	0.186
7	C	0	0.186
8	B	-45	0.186
9	A	0	t27
10	B	45	0.186
11	C	0	0.186
12	B	-45	0.186
13	B	45	0.296
14	C	0	0.296
15	B	-45	0.296
16	B	45	0.296
17	C	0	0.296
18	B	-45	0.296
19	B	45	0.296
20	C	0	0.296
21	B	-45	0.296
22	B	45	0.296
23	C	0	0.296
24	B	-45	0.296
25	B	45	0.296
26	C	0	0.296
27	B	-45	0.296

LAYUP CODE 7			
Layer	Material	Angle (°)	Thickness (mm)
1	D	0	0.130
2	C	0	0.372
3	B	45	0.296
4	C	0	0.296
5	B	-45	0.296
6	E	0	6.350
7	B	45	0.186
8	C	0	0.186
9	B	-45	0.186

LAYUP CODE	t15 (mm)
1	26.40
2	19.80
3	13.20
5	9.240
8	6.350
9	7.920
11	6.600
13	5.280
15	3.960

LAYUP CODE	t27 (mm)
6	9.240
10	7.920
12	6.600
14	5.280

LAYUP CODE 4			
Layer	Material	Angle (°)	Thickness (mm)
1	D	0	0.13
2	C	0	0.372
3	B	45	0.296
4	C	0	0.296
5	B	-45	0.296
6	B	45	0.186
7	C	0	0.186
8	B	-45	0.186
9	B	45	0.186
10	C	0	0.186
11	B	-45	0.186
12	B	45	0.296
13	C	0	0.296
14	B	-45	0.296

LAYUP CODE 16 (Shear Web's width)			
Layer	Material	Angle (°)	Thickness (mm)
1	B	45	0.186
2	C	0	0.186
3	B	-45	0.186
4	E	0	9.525
5	B	45	0.186
6	C	0	0.186
7	B	-45	0.186

Appendix D

Aerodynamic Coefficients

Reynolds		500,000	
alpha	CL	CD	CM
-4	-0.1722	0.01425	-0.1333
-3	-0.0571	0.01334	-0.1346
-2	0.0521	0.01296	-0.1343
-1	0.1629	0.01267	-0.1339
0	0.2746	0.01232	-0.1336
1	0.3875	0.0123	-0.1332
2	0.5012	0.01222	-0.1328
3	0.6126	0.0123	-0.1318
4	0.7212	0.01256	-0.1301
5	0.8278	0.01286	-0.1279
6	0.9255	0.01336	-0.124
7	1.0191	0.01404	-0.1195
8	1.0991	0.01542	-0.1131
9	1.1567	0.01803	-0.1042
10	1.2123	0.02092	-0.0959
11	1.2621	0.02437	-0.088
12	1.3054	0.02873	-0.0811
13	1.3404	0.0345	-0.0755
14	1.3671	0.042	-0.0718
15	1.3831	0.05174	-0.0701
16	1.393	0.06346	-0.0706
17	1.3917	0.07788	-0.0735
18	1.3862	0.09411	-0.0784
19	1.38	0.112	-0.0852
20	1.3727	0.1291	-0.0935
21	1.3675	0.145	-0.10041
22	1.3634	0.16076	-0.1098
23	1.3684	0.17583	-0.1197
24	1.3798	0.1889	-0.1288
25	1.3821	0.20395	-0.1402
26	1.3862	0.21824	-0.1517
27	1.3946	0.23116	-0.1625

Reynolds		1,000,000	
alpha	CL	CD	CM
-4	-0.1689	0.01068	-0.1362
-3	-0.059	0.01047	-0.1359
-2	0.0548	0.01	-0.1365
-1	0.17	0.0098	-0.1368
0	0.287	0.00972	-0.1371
1	0.4035	0.00972	-0.1372
2	0.5189	0.0098	-0.137
3	0.634	0.00995	-0.1364
4	0.7458	0.01026	-0.1352
5	0.8542	0.0106	-0.1332
6	0.957	0.0111	-0.1302
7	1.0485	0.01221	-0.1254
8	1.122	0.01421	-0.1181
9	1.1953	0.01611	-0.1109
10	1.2639	0.01823	-0.1036
11	1.326	0.02073	-0.096
12	1.3821	0.02382	-0.0888
13	1.4284	0.02799	-0.082
14	1.4646	0.03363	-0.0763
15	1.4933	0.0409	-0.0724
16	1.5103	0.05039	-0.0703
17	1.5197	0.06198	-0.0704
18	1.5218	0.07568	-0.0727
19	1.5135	0.09198	-0.0773
20	1.5048	0.10934	-0.0839
21	1.4846	0.12924	-0.0936
22	1.4671	0.14658	-0.1018
23	1.4497	0.16547	-0.1136
24	1.4212	0.18631	-0.1285
25	1.4123	0.20329	-0.1412
26	1.4075	0.21928	-0.1539
27	1.407	0.23416	-0.1662

Reynolds		1,500,000	
alpha	CL	CD	CM
-4	-0.1691	0.00942	-0.1375
-3	-0.0539	0.00907	-0.1383
-2	0.0629	0.00893	-0.1389
-1	0.1809	0.00882	-0.1395
0	0.2993	0.00875	-0.1401
1	0.4182	0.00876	-0.1405
2	0.5352	0.00888	-0.1405
3	0.651	0.00908	-0.1401
4	0.7662	0.00931	-0.1394
5	0.8775	0.00971	-0.1379
6	0.9784	0.01039	-0.1345
7	1.0575	0.01201	-0.1276
8	1.1391	0.01356	-0.1213
9	1.2159	0.01524	-0.1144
10	1.2907	0.01697	-0.1076
11	1.3598	0.01902	-0.1005
12	1.4203	0.02166	-0.0931
13	1.4711	0.02521	-0.0858
14	1.5117	0.03003	-0.0792
15	1.5449	0.03631	-0.0742
16	1.5698	0.04434	-0.0709
17	1.5849	0.05448	-0.0696
18	1.5913	0.06681	-0.0704
19	1.5929	0.08087	-0.0732
20	1.5842	0.09738	-0.0783
21	1.5697	0.11563	-0.0858
22	1.55335	0.133595	-0.09485
23	1.537	0.15156	-0.1039
24	1.5043	0.17265	-0.1179
25	1.4788	0.1924	-0.1324
26	1.4571	0.21133	-0.1473
27	1.4411	0.22906	-0.162

Reynolds		2,500,000	
alpha	CL	CD	CM
-4	-0.1637	0.00814	-0.14
-3	-0.0449	0.00803	-0.141
-2	0.075	0.00794	-0.1421
-1	0.1955	0.00782	-0.1432
0	0.3162	0.00782	-0.1439
1	0.4357	0.00787	-0.1445
2	0.5534	0.00807	-0.1444
3	0.6717	0.00822	-0.1444
4	0.7876	0.0085	-0.1438
5	0.8992	0.00896	-0.1424
6	0.993	0.01026	-0.1379
7	1.07595	0.0115725	-0.131625
8	1.1589	0.012885	-0.12535
9	1.24185	0.0141975	-0.119075
10	1.3248	0.01551	-0.1128
11	1.398	0.01725	-0.1058
12	1.4622	0.0195	-0.0981
13	1.5183	0.02242	-0.0905
14	1.5645	0.02639	-0.0832
15	1.6035	0.03155	-0.0771
16	1.6344	0.03828	-0.0724
17	1.6595	0.04653	-0.0696
18	1.6723	0.05713	-0.0687
19	1.6819	0.06914	-0.0695
20	1.6744	0.08446	-0.0729
21	1.6702	0.1002	-0.0779
22	1.6626	0.11716	-0.0849
23	1.6424	0.13517	-0.0933
24	1.6176	0.15432	-0.1043
25	1.5966	0.17263	-0.1164
26	1.5694	0.19187	-0.1306
27	1.5408	0.21119	-0.1462

Reynolds		5,000,000	
alpha	CL	CD	CM
-4	-0.1535	0.00707	-0.1432
-3	-0.032	0.00703	-0.1446
-2	0.0907	0.0069	-0.1461
-1	0.2128	0.00687	-0.1473
0	0.3335	0.00698	-0.1479
1	0.4546	0.00704	-0.1487
2	0.5739	0.00724	-0.1488
3	0.6924	0.00745	-0.1488
4	0.8083	0.0078	-0.1482
5	0.9112	0.00882	-0.1452
6	1.0094	0.00998	-0.1414
7	1.1068	0.01091	-0.1373
8	1.1942	0.01176	-0.1313
9	1.283	0.01275	-0.1256
10	1.366	0.01395	-0.1193
11	1.4432	0.01539	-0.1123
12	1.5123	0.01721	-0.1047
13	1.5756	0.01946	-0.0969
14	1.6308	0.0224	-0.0892
15	1.678	0.02628	-0.082
16	1.7175	0.03138	-0.0759
17	1.7505	0.03784	-0.0712
18	1.7744	0.04606	-0.0681
19	1.7859	0.05659	-0.0669
20	1.7928	0.0687	-0.0676
21	1.7936	0.08248	-0.0702
22	1.7789	0.09929	-0.0753
23	1.7633	0.11688	-0.0824
24	1.7464	0.13445	-0.091
25	1.7314	0.15133	-0.1003
26	1.7133	0.16837	-0.1111
27	1.6901	0.18597	-0.1239

Tecnológico de Monterrey, Campus Monterrey



30002007497605

<http://biblioteca.mty.itesm.mx>